# *Sensitivity of Spent Fuel Temperatures to Variable Canister Backfills*

## Spent Fuel and Waste Disposition

***Prepared for***
***US Department of Energy***
***Spent Fuel and Waste Science and Technology***

**Pacific Northwest National Laboratory**
***CL Grant***
***CF Campbell***
***DJ Richmond***

***August 30, 2021***
**M3SF-21PN010203021**
**PNNL-31875**

# SUMMARY

This report describes thermal modeling done to understand the effects of a hypothetical loss of backfill to a spent fuel storage canister. A NAC MAGNASTOR system was analyzed using STAR-CCM+ and COBRA-SFS at various heat loads, helium pressures, and air environments over a simulated 300 year storage period. When helium was lost later in life the results showed no safety impact to the thermal performance of the cask system and fuel cladding. However, there were other results of interest from this study. The potential to detect helium leaks using external temperature measurement was considered and found to be a potential area for future technology development. The other major result of interest was the significant change in flow velocities with an air environment. This data will be useful in understanding the potential impacts of a breached canister.

This page is intentionally left blank.

# ACKNOWLEDGEMENTS

The authors wish to thank Ned Larson and the Department of Energy Spent Fuel Waste Science and Technology for funding this work. We thank Jim Fort for supporting STAR-CCM+ model review and Brian Hom and Colleen Winters for their careful review and support.

This page is intentionally left blank.

# CONTENTS

# LIST OF FIGURES

# LIST OF TABLES

# ACRONYMS

| | |
|---|---|
| BWR | boiling water reactor |
| CFD | computational fluid dynamics |
| CISCC | chloride-induced stress corrosion cracking |
| DOE | U.S. Department of Energy |
| EPRI | Electric Power Research Institute |
| FSAR | Final Safety Analysis Report |
| ISFSI | independent spent fuel storage installation |
| MAGNASTOR | Modular, Advanced Generation, Nuclear All-purpose STORage |
| NAC | NAC International |
| NIST | National Institute of Standards and Technology |
| NRC | U.S. Nuclear Regulatory Commission |
| ORNL | Oak Ridge National Laboratory |
| PCT | peak cladding temperature |
| PNNL | Pacific Northwest National Laboratory |
| PWR | pressurized water reactor |
| SST | shear stress transport |
| TSC | Transportable Storage Container |
| UFSAR | Updated Final Safety Analysis Report |

This page is intentionally left blank.

# SENSITIVITY OF SPENT FUEL TEMPERATURES TO VARIABLE CANISTER BACKFILLS

## 1. INTRODUCTION

The long-term extension of dry storage in the U.S. brings unique design, licensing and operations considerations. The potential for chloride-induced stress corrosion cracking (CISCC) of canister-based systems in extended dry storage is being investigated by numerous research organizations including the U.S. Department of Energy's (DOE's) national labs. The development of a through wall crack has the potential to breach a canister's confinement boundary and release any gases present. These include the fill gas or fission gases in the event of a fuel failure. In extreme cases, fuel particles from damaged assemblies have potential to be released from the canister. For canister systems the loss of fill gas may have consequences for their thermal performance as well. Helium is chosen as a fill gas for spent fuel for its inert nature and also its favorable heat transfer properties. In all systems the high thermal conductivity helps move heat out of the cask through fluid conduction. In a vertical ventilated canister system, the canister is filled with helium at pressure to promote a thermosiphon where internal circulation increases heat transfer from the fuel assemblies. The effect of low helium pressure and a change in fill gas to atmospheric air will be evaluated. The work described in this report is focused on evaluating that effect on thermal performance at different points in the canister's life cycle. In this report that life cycle is defined out to 300 years post initial loading to fully encompass currently licensed extended storage and have relevance for potential direct disposal activities.

A primary question to be answered by thermal analysis is whether the elevated temperatures will challenge any design temperature limits. Additionally, the analysis presented in this report will be a useful reference for concurrent related research. External flow and canister temperature results are useful for studying potential particle deposition and crack growth. The internal flows can be used for understanding the behavior of any fuel particles and gases internal to the canister. Another topic that researchers are looking at currently is the possibility of developing a detection mechanism for alerting the occurrence of containment breaches through the change in canister thermal profile. The results presented here will be useful to the development of that technology as well. To summarize the questions:

1. What are the thermal impacts in areas of interest?
2. Can we determine fill pressure loss through external (relative to canister) temperature behavior?
3. What are the impacts on flow velocities (inside and outside the canister)?

The storage module selected for this study is the NAC International, Inc. (NAC) Modular, Advanced Generation, Nuclear All-purpose STORage (MAGNASTOR). This is a modern vertical ventilated system that is operated with internally pressurized helium. The system chosen represents the typical capacity and design of vertical ventilated systems in use in the U.S. It holds 37 pressurized water reactor (PWR) assemblies with various heat zone loading maps that have been licensed by the U.S. Nuclear Regulatory Commission (NRC).

Detailed models of the NAC MAGNASTOR had been previously developed using COBRA-SFS (Michener et al. 2017) and STAR-CCM+ (Siemens, PLM 2019), and were modified as needed for the current study. The immediate purpose of this modeling effort was to investigate the effects of a changing internal gas environment on the thermal behavior of the MAGNASTOR system. Estimates of fuel cladding temperatures were of primary interest, but temperatures of the cask components were captured as well. The models developed for both codes represent the entire cask, but the capabilities of each code are exploited to capture detailed evaluations of different portions of the system.

COBRA-SFS is used to model the fuel and basket region in detail and provide an accurate representation of heat transfer by radiation, convection, and conduction in the radial direction from the fuel to external ambient. Heat transfer paths through the base and top of the cask, which are by design of much lesser significance compared to radial heat removal, are treated in a more simplistic manner.

STAR-CCM+ is used to model the solid structures of the basket and concrete cask in detail, including the base and lid regions, but approximates the fuel assemblies within the basket as a porous media, and utilizes an effective thermal conductivity model to capture fuel cladding temperatures. With consistent material specifications and the same boundary conditions, these two models are complementary and provide an effective consistency check to verify the models are appropriately capturing the physical behavior of the system. This provides confidence that the results of the thermal evaluations accurately represent the temperatures that will be achieved in the storage system, within the uncertainty in the various input parameters provided.

A general background for the NAC MAGNASTOR system is provided in Section 2.0. The general modeling approach is summarized in Section 3.0. The model constructed for COBRA-SFS is described in detail in Section 4.0. The results of the COBRA-SFS models are summarized in Section 5.0. The STAR-CCM+ model is described in Section 6.0. Results obtained with the STAR-CCM+ models are presented in Section 7.0. Section 8.0 provides the comparison and discussion of the results, while Section 9.0 lists the conclusions from this work, and Section 10.0 recommends avenues for future work. Section 11.0 contains the list of references cited.

# 2. MAGNASTOR DESCRIPTION

The MAGNASTOR module is a spent nuclear fuel dry storage system manufactured by NAC International, Inc. The MAGNASTOR has a fuel storage canister inside a ventilated concrete cask. NAC refers to their canister as the Transportable Storage Canister (TSC).

An external view of the MAGNASTOR is shown in Figure 2-1. The concrete cask inner cavity and air flow passages are lined with carbon steel plate. The TSC sits on an elevated pedestal above the four air inlets. At the ground level, each of the inlet passages are partially filled with several rows of vertical, cylindrical pins that provide shielding. Radial positioning of the TSC within the concrete cask cavity is maintained by carbon steel standoff supports that extend outward from the concrete cask inner shell. Outlet air passages and vents are included near the top of the concrete cask. Access to the inner cavity for insertion of the TSC is provided by a removable lid.

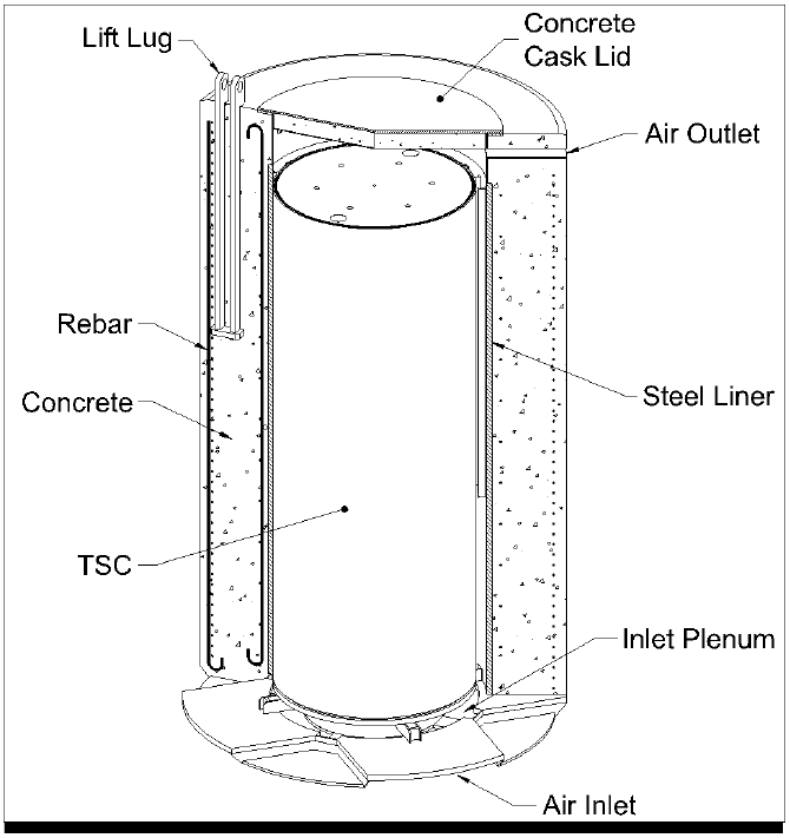


**Figure 2-1. MAGNASTOR Storage System**

The TSC shell and PWR fuel basket is shown in Figure 2-2. The basket has 37 assembly positions for PWR fuel. An alternate design has 87 assembly positions for boiling water reactor (BWR) fuel, but only the PWR design was modeled for this project. The fuel tubes are made from carbon steel plate and are connected to adjacent tubes at the corners by machined rods. Neutron absorbers are attached to the fuel tube walls with a thin stainless-steel retainer on the outer face. Carbon steel side and corner support assemblies are bolted to the basket assembly and position the assembly within the TSC. The TSC shell and bottom are manufactured using stainless steel, as is the TSC lid. The TSC lid shield material is carbon steel.

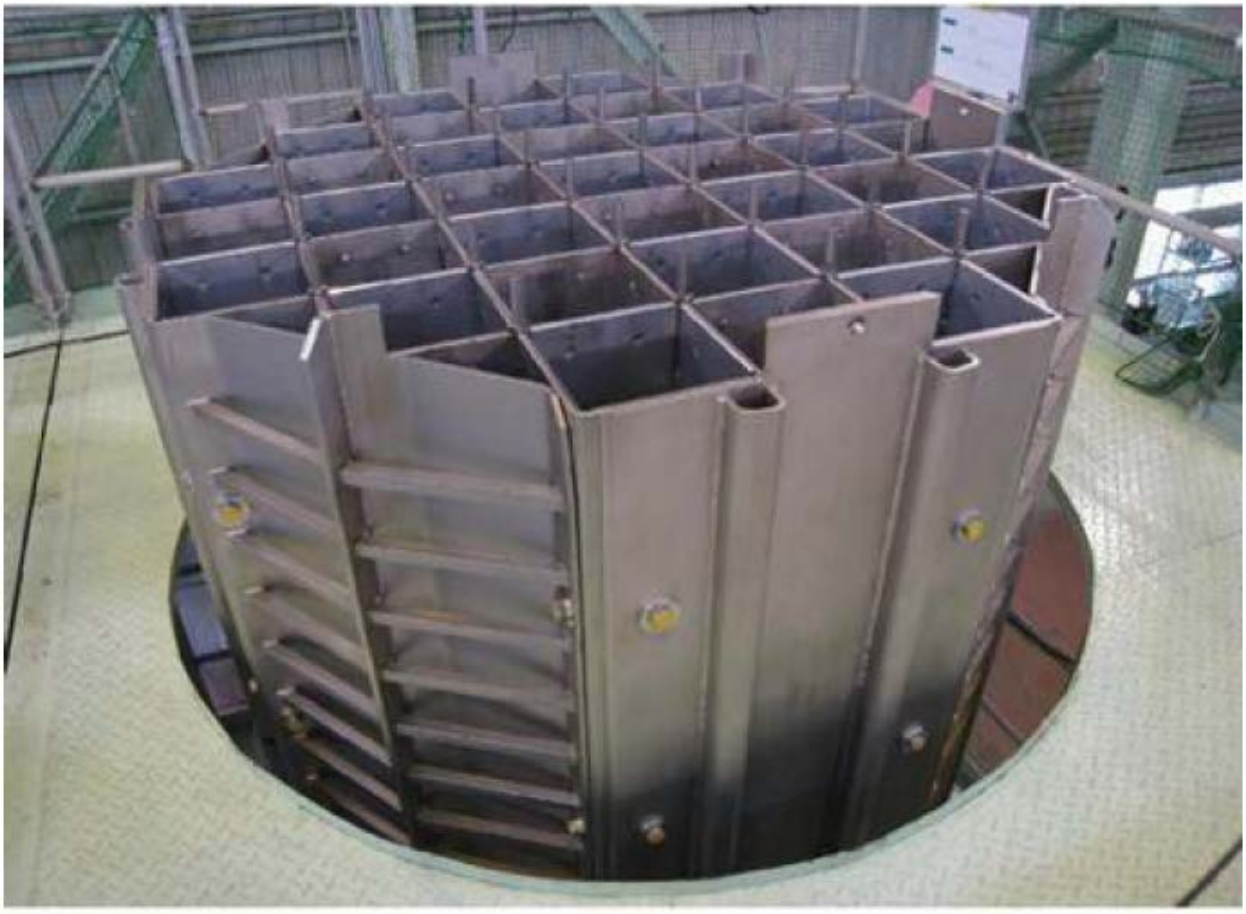

**Figure 2-2. MAGNASTOR PWR Basket**

In normal operations, the loaded TSC is moved from the transfer cask into the concrete cask following vacuum drying and backfill with helium. The assembled storage system is then transported by crawler transport to the Independent Spent Fuel Storage Installation (ISFSI).

# 3. MODELING APPROACH

This section describes the overall modeling approach and aspects that apply to the COBRA-SFS models and the STAR-CCM+ models. The intent is to model a representative case for spent fuel in dry storage. The approach laid out here, while applied to a specific cask and heat load, will be broadly applicable to similar heat loads and designs in the fleet. Sections 3.5 and 3.7 describe the estimated heat loads applied to the models.

## 3.1 Scenario Description

The modeling scenario of interest for this study is one where a canister-based system becomes depressurized during its life cycle. For this report the life cycle is extended beyond the 100 year extended storage period currently in use to both bound the problem and allow for results applicable to operations in direct disposal scenarios currently being researched. Throughout discussion in this report the terms early and late in life are used. There is not a good definitive number for this because it depends on which design and licensing and operational factors are being considered. For this report and general thermal analysis under 50% design basis heat load can be considered late in life. In actual time this may be well under halfway through a canister's operational life. However, the thermal behavior changes slower and less dramatically as heat loads decrease further below 50%. For this study the exact mechanism of depressurization is not particularly relevant as long as it does not change the configuration of the cask in a way where it cannot be modeled with its standard licensing design drawings. The current motivation is primarily potential CISCC; however, a damaged weld or vent/drain port closure that causes depressurization would also be applicable. The thermal effects of replacement with atmospheric air will also be studied.

## 3.2 Steady State vs. Transient Analysis

This work uses steady-state analysis in all models and does not try to model the depressurization process directly. Overall, this could be termed a quasi-steady state approach because results can be plotted through a canister lifecycle. The choice of steady state modeling is useful for several reasons.

The first reason for choosing steady state analysis is to keep the results generally applicable. In simple terms, the speed at which cask depressurization occurs is dependent on the internal-external pressure differential and the flow resistance of the opening. However, these are not constant parameters for any breach at any time. To fully know the depressurization rate, one would need to consider internal and external temperatures, initial fill gas pressure, along with the opening's size, shape, and roughness. Because this report is meant to be general, those values are not calculated here.

Another justification for choosing steady state analysis is that this work is focused on the thermal response to a loss of pressure scenario, not the depressurization event itself. Whatever thermal response occurs, it will be relatively slow due to the speed of depressurization, environmental variation, and the time constant of a spent fuel storage cask. Even with a catastrophic breach and near instantaneous loss of pressure, a typical large PWR cask such as the MAGNASTOR will take 2-3 days for fuel temperatures to react to any changes. Evidence of this can be seen in vacuum operations and the data collected in the High Burnup Demonstration Cask Research Project (Fort et al. 2019). In any case, the CISCC crack of most interest to the study will likely take from weeks to months to fully depressurize the cask. Because the driving force expelling the helium will diminish as the internal pressure drops, this depressurization phase will proceed more slowly the longer it goes on. Once the helium pressure is lost, it will take another long period of time for that internal fill gas to exchange with air. This exchange period would not begin in any significance until there was zero pressure differential between the cask fill gas and the external atmosphere.

## 3.3 Relevant Performance Metrics

The performance metrics relevant to this report are determined for safety limits and research. The primary safety limits considered are the normal cladding limit of 400 °C (752 °F) and the accident limit of 570 °C (1058 °F). These are generally in use in the U.S. in response to NRC ISG 11 rev. 3 (NRC 2003). The other metrics that will be considered are the flow velocities and rates inside and outside the canister. These are relevant to particle deposition and potential release. Finally, the canister wall, lid, and base temperatures will be examined to understand the ability to predict depressurization based off these metrics.

## 3.4 Assembly Configuration

The MAGNASTOR basket has 37 assembly positions for PWR fuel. In both the COBRA-SFS and STAR-CCM+ models, the assemblies were numbered as shown in Figure 3-1.

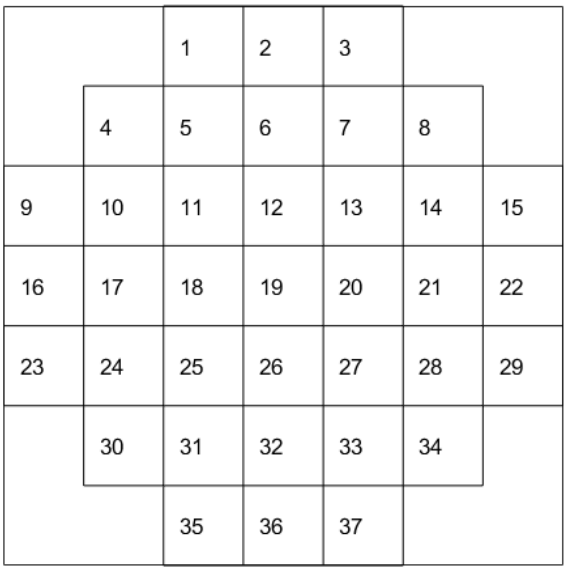


**Figure 3-1. Assembly Numbers Used in Modeling**

## 3.5 Loading Configurations

Three different loading conditions were used in the modeling process. Two were provided by NAC in their Final Safety Analysis Report (FSAR [NAC 2011]). These are the three-zone and four-zone loading configurations. For brevity, these configurations are called “3Z” and “4Z” respectively for the remainder of this report. Diagrams showing the 3Z and 4Z loading configurations can be seen in Figure 3-2 and Figure 3-3. The final loading configuration used was a flat distribution in which all assemblies have the same heat load. In this report, this is referred to as the one-zone, or “1Z,” configuration.

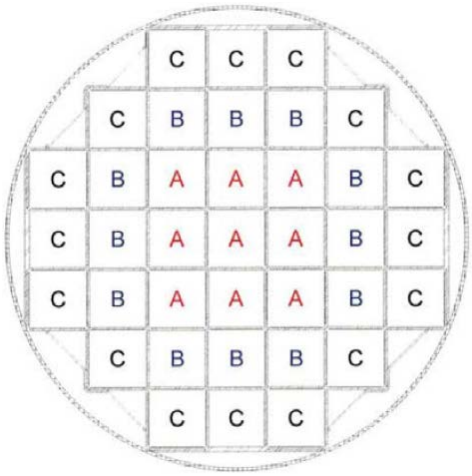


**Figure 3-2. 3Z (Three-Zone) Loading Configuration**

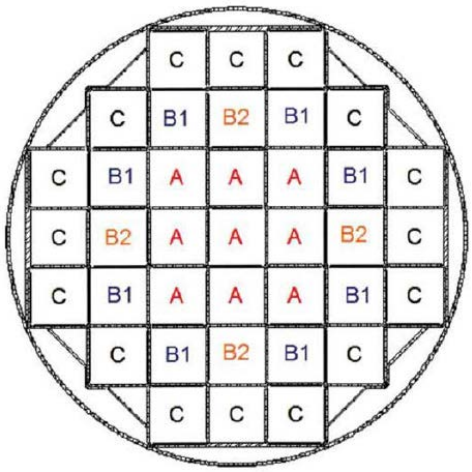


**Figure 3-3. 4Z (Four-Zone) Loading Configuration**

## 3.6 Axial Decay Heat Profiles

The axial decay heat profiles for each assembly, for input to the thermal models, were constructed by Pacific Northwest National Laboratory (PNNL). The resulting axial decay heat profiles are shown in Figure 3-4. The profiles are the same for all assemblies. Figure 3-4 also shows the standard axial profile for low burnup fuels from DOE-RW-0472 (DOE 1997).

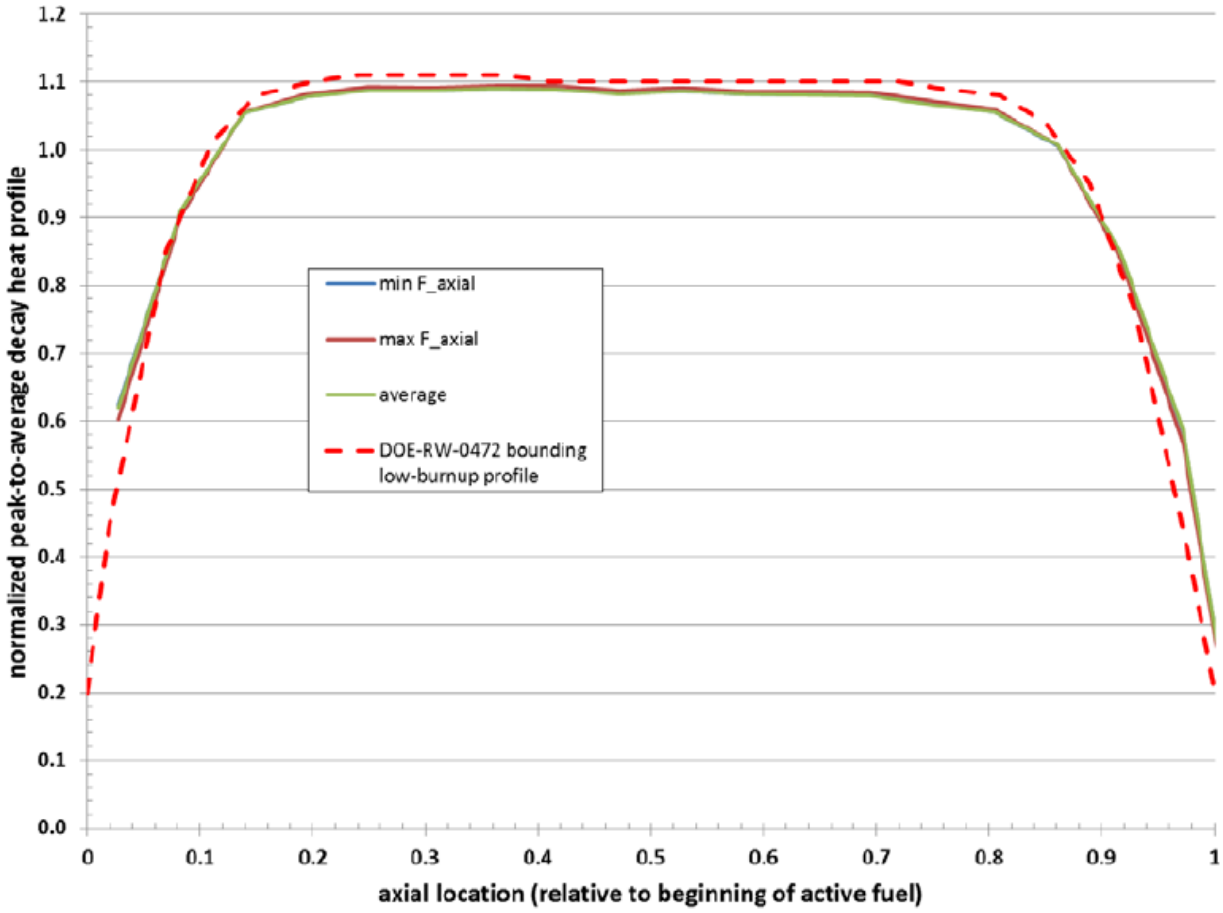


**Figure 3-4. Maximum, Minimum, and Average Axial Profiles Compared with the Standard Axial Profile for Low Burnup Fuels (DOE 1998)**

The axial profiles used in the models for this project were originally developed for another project involving the MAGNASTOR module (Fort et al. 2016). As a part of that project, Oak Ridge National Laboratory (ORNL) used a database containing approximately 3000 burnup profiles from different reactors to estimate the actual characteristics of spent fuel stored in a MAGNASTOR storage system. From that database, a subset using similar reactors, initial enrichment and burnup resulted in an average profile that was used for the assemblies. PNNL then used that data to generate the axial decay heat profile shown in Figure 3-4. The impact of different burnup profiles on the assembly average decay heat is less than half a percent. It does, however, have a significant impact on the axial distribution of decay heat.

## 3.7 Assembly Heat Load Values

A major focus of this research was on the effects of changing canister internal environment over a long span of time. To facilitate this, an estimated heat load was calculated to simulate 50, 100, 200, and 300 years after a MAGNASTOR module is installed at an ISFSI. The heat load values used were originally developed for another study of the MAGNASTOR storage system (Fort et al. 2016). The calculations of decay heat were performed by ORNL using the ORIGAMI tool from SCALE 6.2. The decay heat was calculated on a pin-by-pin basis using real world estimated burnup data. The original project produced "best estimate" decay heats for a specific fuel loading that had a similar distribution to the design basis loading in the FSAR (NAC 2011), albeit at a lower heat load of 26.4kW. For this study, the design basis

heat load of 35.5 kW was used for year 0. The subsequent years were scaled using the factor developed during the original study. Table 3-1 shows the total canister heat loads calculated for each time period. The heat loads used in the models are shown in Figures 3-5 to 3-20. Each value shown is the total heat load in Watts for the assembly pictured.

**Table 3-1. Heat Loads Over Time**

| Years After Installation | Heat Load [kW] | Percent Design Basis |
|---|---|---|
| 0 (Design Basis) | 35.5 | 100% |
| 50 | 14.8 | 41.7% |
| 100 | 8.7 | 24.5% |
| 200 | 5.4 | 15.2% |
| 300 | 4.2 | 11.8% |

In the results sections of this report, heat loads are characterized as different points in time. However, these can also be thought of in terms of "percent design basis" for general applicability. This choice was made to account for the non-linear decay of spent fuel heat generation and allow for better qualitative applications to other work. Crack growth studies and depressurization are generally reported in terms of time, which will compare well to the results of this paper. If sensitivity to canister pressure at a specific heat load is needed, then the results will be relevant for a specific point in time, but care should be taken when trying to draw conclusions in a temperature behavior vs. time graph. The heat load vs. time graph in Figure 3-5 shows the non-linear behavior and why this distinction is important.

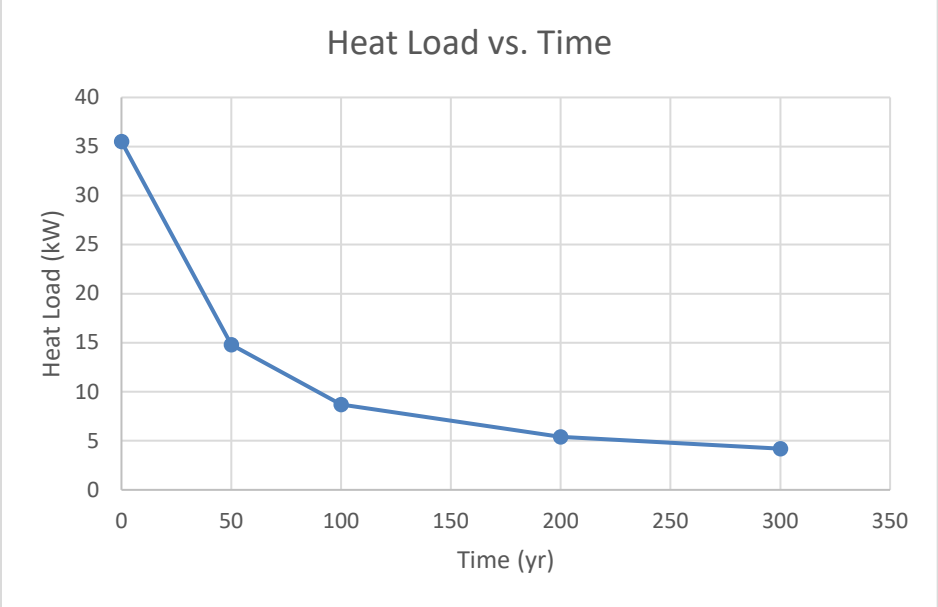


**Figure 3-5. Heat Load versus Time**

Figure 3-6 through Figure 3-20 show the individual assembly decay heat in Watts (W) for the various loading patterns at different times.

| | | | | | | |
|---|---|---|---|---|---|---|
| | | 800 | 800 | 800 | | |
| | 800 | 1200 | 1200 | 1200 | 800 | |
| 800 | 1200 | 922 | 922 | 922 | 1200 | 800 |
| 800 | 1200 | 922 | 922 | 922 | 1200 | 800 |
| 800 | 1200 | 922 | 922 | 922 | 1200 | 800 |
| | 800 | 1200 | 1200 | 1200 | 800 | |
| | | 800 | 800 | 800 | | |

**Figure 3-6. Heat Load Values (W), 3Z, Year 0 (Design Basis)**

| | | | | | | |
|---|---|---|---|---|---|---|
| | | 334 | 334 | 334 | | |
| | 334 | 501 | 501 | 501 | 334 | |
| 334 | 501 | 385 | 385 | 385 | 501 | 334 |
| 334 | 501 | 385 | 385 | 385 | 501 | 334 |
| 334 | 501 | 385 | 385 | 385 | 501 | 334 |
| | 334 | 501 | 501 | 501 | 334 | |
| | | 334 | 334 | 334 | | |

**Figure 3-7. Heat Load Values (W), 3Z, Year 50**

| | | | | | | |
|---|---|---|---|---|---|---|
| | | 196 | 196 | 196 | | |
| | 196 | 294 | 294 | 294 | 196 | |
| 196 | 294 | 226 | 226 | 226 | 294 | 196 |
| 196 | 294 | 226 | 226 | 226 | 294 | 196 |
| 196 | 294 | 226 | 226 | 226 | 294 | 196 |
| | 196 | 294 | 294 | 294 | 196 | |
| | | 196 | 196 | 196 | | |

**Figure 3-8. Heat Load Values (W), 3Z, Year 100**

| | | | | | | |
|---|---|---|---|---|---|---|
| | | 121 | 121 | 121 | | |
| | 121 | 182 | 182 | 182 | 121 | |
| 121 | 182 | 140 | 140 | 140 | 182 | 121 |
| 121 | 182 | 140 | 140 | 140 | 182 | 121 |
| 121 | 182 | 140 | 140 | 140 | 182 | 121 |
| | 121 | 182 | 182 | 182 | 121 | |
| | | 121 | 121 | 121 | | |

**Figure 3-9. Heat Load Values (W), 3Z, Year 200**

| | | | | | | |
|---|---|---|---|---|---|---|
| | | 95 | 95 | 95 | | |
| | 95 | 143 | 143 | 143 | 95 | |
| 95 | 143 | 110 | 110 | 110 | 143 | 95 |
| 95 | 143 | 110 | 110 | 110 | 143 | 95 |
| 95 | 143 | 110 | 110 | 110 | 143 | 95 |
| | 95 | 143 | 143 | 143 | 95 | |
| | | 95 | 95 | 95 | | |

**Figure 3-10. Heat Load Values (W), 3Z, Year 300**

| | | | | | | |
|---|---|---|---|---|---|---|
| | | 830 | 830 | 830 | | |
| | 830 | 1300 | 1800 | 1300 | 830 | |
| 830 | 1300 | 513 | 513 | 513 | 1300 | 830 |
| 830 | 1800 | 513 | 513 | 513 | 1800 | 830 |
| 830 | 1300 | 513 | 513 | 513 | 1300 | 830 |
| | 830 | 1300 | 1800 | 1300 | 830 | |
| | | 830 | 830 | 830 | | |

**Figure 3-11. Heat Load Values (W), 4Z, Year 0 (Design Basis)**

| | | | | | | |
|---|---|---|---|---|---|---|
| | | 346 | 346 | 346 | | |
| | 346 | 542 | 751 | 542 | 346 | |
| 346 | 542 | 214 | 214 | 214 | 542 | 346 |
| 346 | 751 | 214 | 214 | 214 | 751 | 346 |
| 346 | 542 | 214 | 214 | 214 | 542 | 346 |
| | 346 | 542 | 751 | 542 | 346 | |
| | | 346 | 346 | 346 | | |

**Figure 3-12. Heat Load Values (W), 4Z, Year 50**

| | | | | | | |
|---|---|---|---|---|---|---|
| | | 204 | 204 | 204 | | |
| | 204 | 319 | 442 | 319 | 204 | |
| 204 | 319 | 126 | 126 | 126 | 319 | 204 |
| 204 | 442 | 126 | 126 | 126 | 442 | 204 |
| 204 | 319 | 126 | 126 | 126 | 319 | 204 |
| | 204 | 319 | 442 | 319 | 204 | |
| | | 204 | 204 | 204 | | |

**Figure 3-13. Heat Load Values (W), 4Z, Year 100**

| | | | | | | |
|---|---|---|---|---|---|---|
| | | 126 | 126 | 126 | | |
| | 126 | 197 | 272 | 197 | 126 | |
| 126 | 197 | 78 | 78 | 78 | 197 | 126 |
| 126 | 272 | 78 | 78 | 78 | 272 | 126 |
| 126 | 197 | 78 | 78 | 78 | 197 | 126 |
| | 126 | 197 | 272 | 197 | 126 | |
| | | 126 | 126 | 126 | | |

**Figure 3-14. Heat Load Values (W), 4Z, Year 200**

| | | | | | | |
|---|---|---|---|---|---|---|
| | | 99 | 99 | 99 | | |
| | 99 | 155 | 215 | 155 | 99 | |
| 99 | 155 | 61 | 61 | 61 | 155 | 99 |
| 99 | 215 | 61 | 61 | 61 | 215 | 99 |
| 99 | 155 | 61 | 61 | 61 | 155 | 99 |
| | 99 | 155 | 215 | 155 | 99 | |
| | | 99 | 99 | 99 | | |

**Figure 3-15. Heat Load Values (W), 4Z, Year 300**

| | | | | | | |
|---|---|---|---|---|---|---|
| | | 959 | 959 | 959 | | |
| | 959 | 959 | 959 | 959 | 959 | |
| 959 | 959 | 959 | 959 | 959 | 959 | 959 |
| 959 | 959 | 959 | 959 | 959 | 959 | 959 |
| 959 | 959 | 959 | 959 | 959 | 959 | 959 |
| | 959 | 959 | 959 | 959 | 959 | |
| | | 959 | 959 | 959 | | |

**Figure 3-16. Heat Load Values (W), 1Z, Year 0 (Design Basis)**

| | | | | | | |
|---|---|---|---|---|---|---|
| | | 400 | 400 | 400 | | |
| | 400 | 400 | 400 | 400 | 400 | |
| 400 | 400 | 400 | 400 | 400 | 400 | 400 |
| 400 | 400 | 400 | 400 | 400 | 400 | 400 |
| 400 | 400 | 400 | 400 | 400 | 400 | 400 |
| | 400 | 400 | 400 | 400 | 400 | |
| | | 400 | 400 | 400 | | |

**Figure 3-17. Heat Load Values (W), 1Z, Year 50**

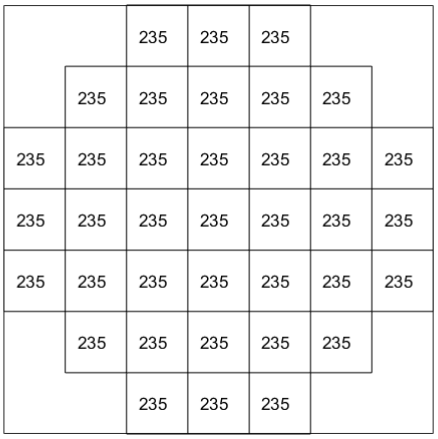


**Figure 3-18. Heat Load Values (W), 1Z, Year 100**

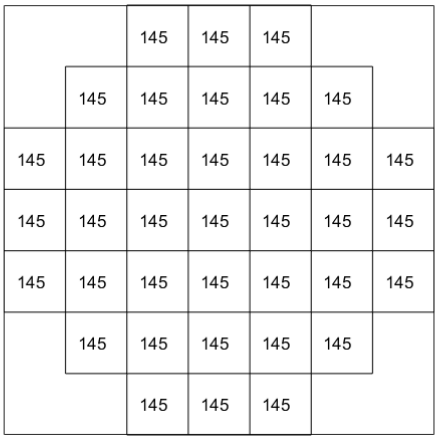


**Figure 3-19. Heat Load Values (W), 1Z, Year 200**

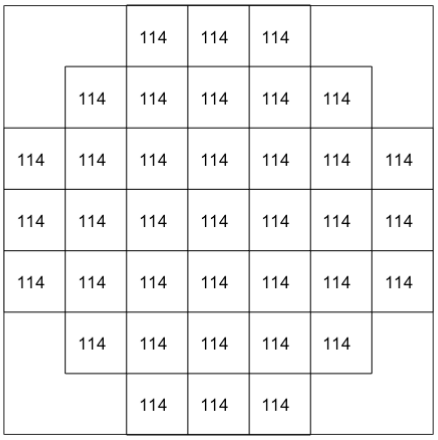


**Figure 3-20. Heat Load Values (W), 1Z, Year 300**

# 4. COBRA-SFS MODEL DESCRIPTION

Section 4.1 describes the representation of the solid material components of the storage system, and Section 4.2 presents a detailed discussion of the rod-and-subchannel representation of the fuel assemblies within the basket. Sections 4.3 and 4.4 describe the material properties and assumptions used in the models, particularly those related to the boundary conditions. The model descriptions in this section are repeated here from the original study (Fort et al. 2016), except for changes related to the fill gas.

## 4.1 Representation of the Storage System

A schematic diagram of the MAGNASTOR is shown in Figure 4-1, which also identifies the basic elements of the COBRA-SFS model of this system. The major path of heat removal from the fuel assemblies in the TSC (and all canister types in vertical storage systems in general) is in the radial direction by conduction, convection, and thermal radiation. Heat is removed from the canister's exterior surface by convection to the buoyancy-driven airflow in the annulus between the concrete cask and TSC shell. Thermal radiation is also significant in carrying heat from the canister to the concrete cask liner and lid, where it is either removed by convection to the cooling airflow or transferred to the outer surfaces of the concrete cask by conduction. From there it is dissipated to the environment by convection or thermal radiation to the essentially infinite heat sink of the ambient air. Heat can also leave the system through the lid structures and base of the cask, but this is generally an insignificant path compared to the radial pathway. For an air-cooled system such as the MAGNASTOR, most of the heat is carried out by the air flow in the annulus.

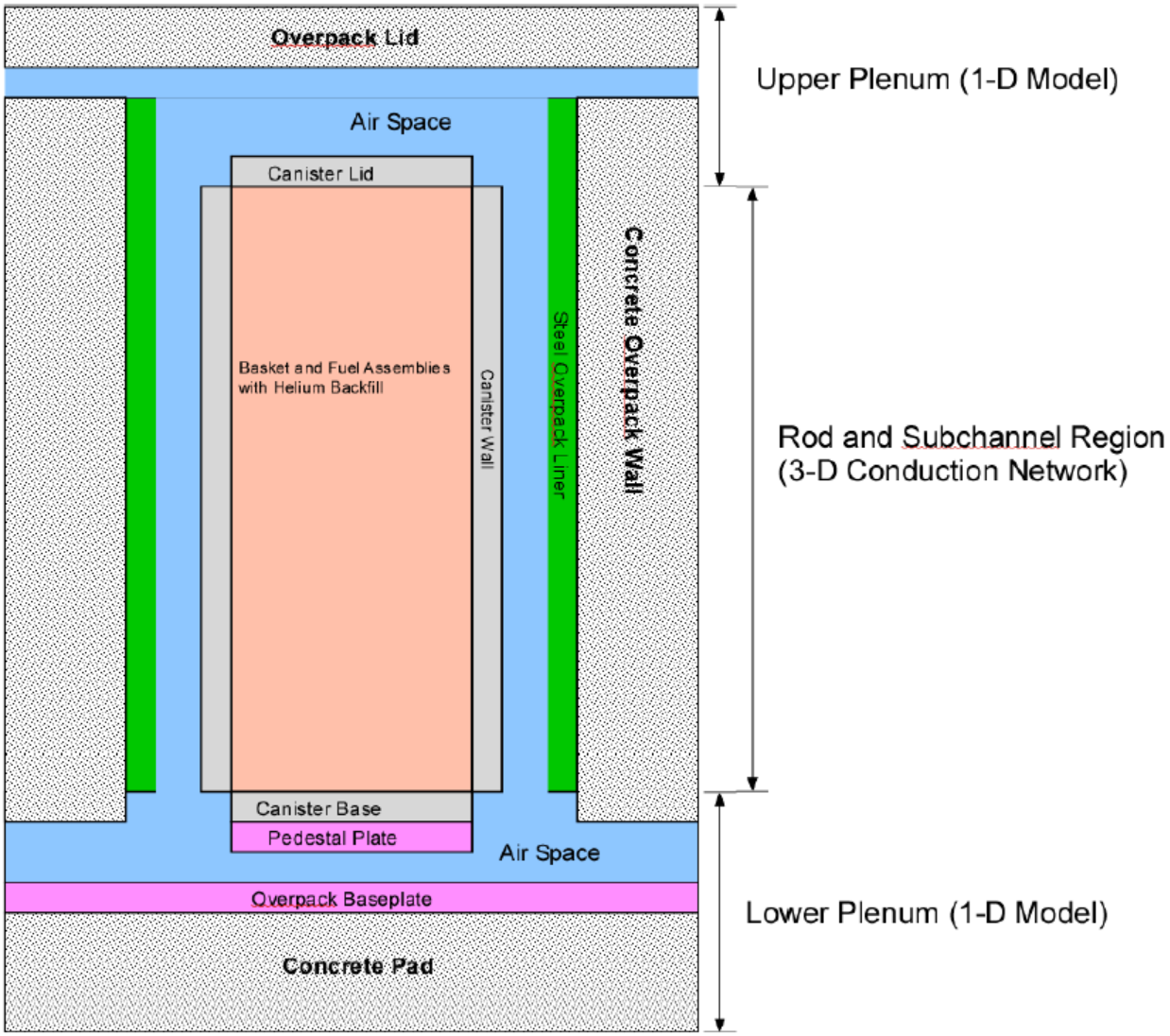


**Figure 4-1. Diagram of MAGNASTOR Showing Major COBRA-SFS Model Regions (NOTE: model image not to scale)**

Consistent with the significant heat transfer paths in the system, the COBRA-SFS modeling approach provides a detailed, highly resolved representation of the fuel assemblies, basket plates, support assemblies, and canister shell over the axial length of the basket. This allows the model to appropriately represent heat transfer by conduction, convection, and thermal radiation in the region of most significant heat removal, to obtain accurate and physically meaningful predictions of local component temperatures, including detailed temperatures and temperature distributions for the fuel rods within the assemblies. Axial heat transfer paths from the system, which in most configurations consists of conduction through layered solid structures, are represented with a network of locally one-dimensional heat transfer paths, using appropriate material properties and contact resistances for the layered components.

Diagrams illustrating the detailed 3-D solid conduction network for the COBRA-SFS model representation of the basket, supports, TSC shell, and concrete cask are shown in Figure 4-2 and Figure 4-3. These diagrams are not to scale, with nodal thicknesses greatly exaggerated for clarity. Figure 4-2 focuses on the representation of the radial heat transfer paths through the basket, basket supports, and canister shell, to the cooling air flow in the annulus between the TSC and concrete cask inner wall. The

basket cells are formed by carbon steel plates, while the neutron absorber is assumed to be composed of equal thickness layers of aluminum and neutron absorber composite with a thin stainless-steel retainer on the outer face. These layered components are attached to the basket structure with steel weld posts. However, these fine details were not represented in the model.

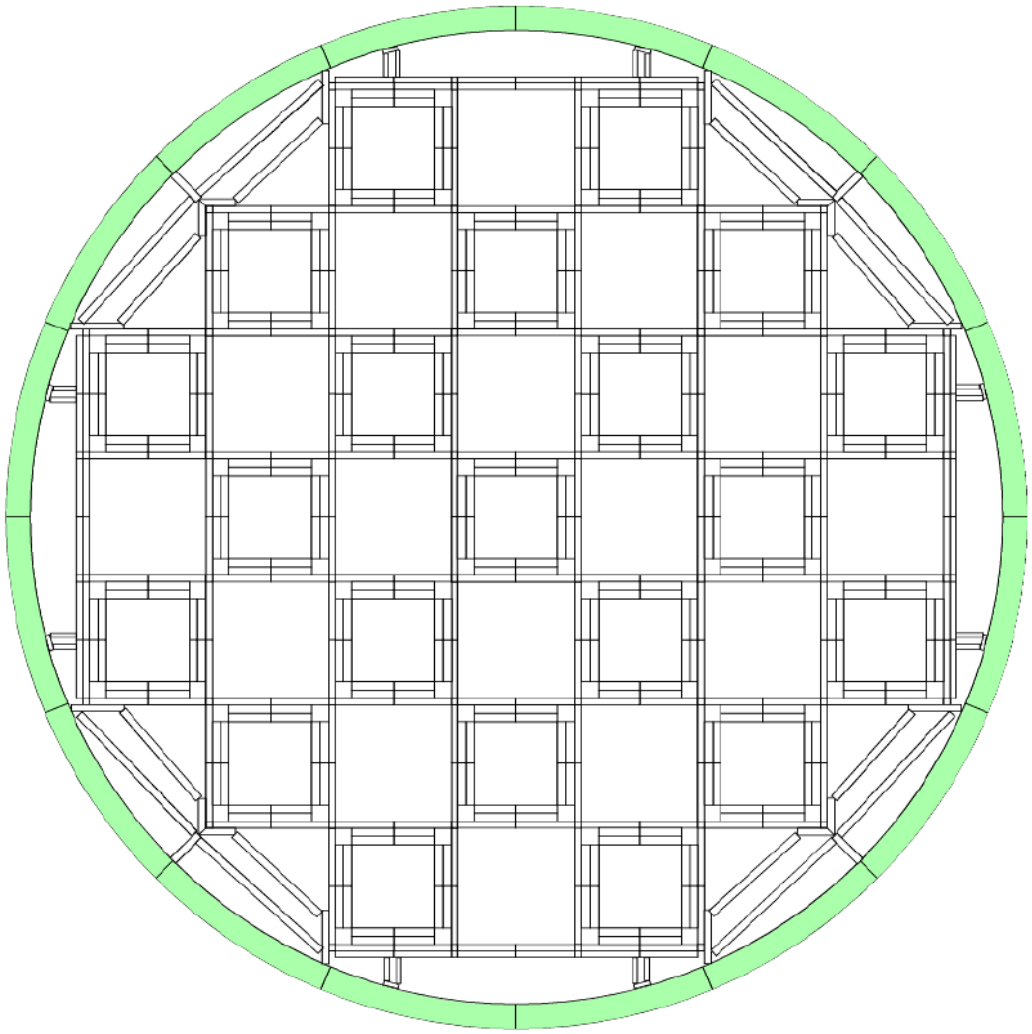

**Figure 4-2. Diagram of COBRA-SFS Model of MAGNASTOR TSC Cross-Section Illustrating TSC Shell, Basket and Support Rail Nodalization (NOTE: diagram not to scale; node thicknesses greatly exaggerated for clarity)**

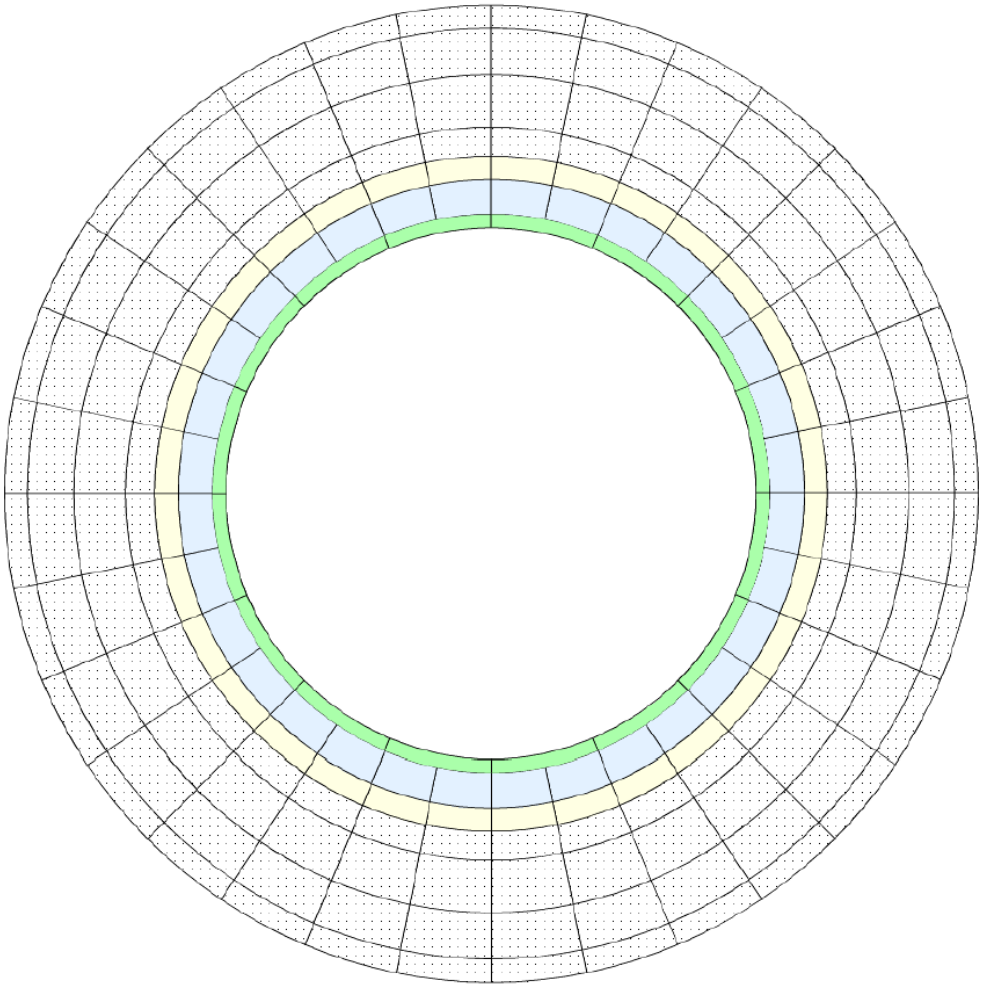

**Figure 4-3. Diagram of COBRA-SFS Model of MAGNASTOR Concrete Cask Cross-Section Illustrating Nodalization of Overpack Body and Exterior Surface (NOTE: diagram not to scale; node thicknesses greatly exaggerated for clarity)**

Thermal gap resistances are included with the neutron absorber because of the imperfect contact between adjacent layers and the consequent effect on contact conductance, since the plates are fastened together only at intermittent points, and because the two materials have different coefficients of thermal expansion. The COBRA-SFS model assumes a resistance equivalent to a 0.01-inch gap between the fuel tube and neutron absorber and between the neutron absorber and the retainer. Heat transfer across each gap is assumed to consist of conduction through helium gas filling the gap and thermal radiation between the adjacent flat plates.

The carbon steel support assemblies between the sides and corners of the basket and the inner surface of the TSC shell are modeled as shown in Figure 4-2. In the MAGNASTOR, these supports are fastened to the basket with bolts (used as screws) at intermittent locations along the axial length of the basket. Since the basket and supports are made of the same material, a gap resistance is not imposed at this interface. However, a gap resistance is imposed between each of the corner supports and the TSC shell equivalent to 0.3 inches of helium.

As shown by the diagram in Figure 4-3, the noding for the COBRA-SFS model becomes much simpler for the concrete cask body, in keeping with the much simpler geometry and direct radial heat transfer paths through the layered steel shells of the cask. The noding mesh for the cask shell is divided into

segments encompassing 22.5° of arc, which is more than adequate to provide a reasonable interface with the detailed modeling of the cask internal structure, as illustrated in Figure 4-2. The thin carbon steel inner liner is represented with a thickness of one node. The thick concrete layer comprising the body of the concrete cask is represented with four layers of variable thickness nodes.

## 4.2 Fuel Assemblies and Internal Convection in the COBRA-SFS Model

The fuel assemblies within each of the 37 cells in the MAGNASTOR basket are represented in the COBRA-SFS model using rod-and-subchannel modeling of the actual assembly geometry. This approach uses a representation of the fluid flow and heat transfer paths within the rod array originally developed for analysis of core hydrodynamics in operating reactors and is still in use today in reactor core and primary system modeling software. The original reactor core code was later expanded and extended to be applicable to computational fluid and thermal analysis of spent fuel assemblies in dry storage packages, primarily by adding a detailed rod-to-rod and rod-to-wall thermal radiation modeling capability (see the COBRA-SFS documentation, Michener et al. 2017, for full details).

A diagram of the basic rod-and-subchannel array for a 17x17 assembly is shown in Figure 4-4. (This diagram is not to scale; the gaps between the rods are greatly exaggerated for clarity.) This diagram is a generic illustration of the rod-and-subchannel modeling for a fuel assembly of this type and does not show local variations due to control rod guide sleeves, instrument tube(s), or burnable poison rods. However, the COBRA-SFS model is capable of considering these individual variations in specific fuel assembly designs, and these variations in the specific assemblies were included in the modeled detail for both the Westinghouse Electric Company W-RFA and the AREVA MkBW fuel assemblies. Each assembly has 24 control rod guide tubes.

A unique feature of the COBRA-SFS code is the detailed modeling of the flow field within the fuel assemblies within the individual basket cells, accounting for local heat transfer by conduction and convection. Thermal radiation is also calculated directly, using grey-body view factors (rod-to-rod and rod-to-wall) for all rods in the array. This representation of the fuel assembly allows for a much more accurate resolution of the local gas temperatures and velocities, fuel cladding surface temperatures, and rod internal temperatures, compared to the typical approach used in computational fluid dynamics (CFD) and finite element analysis codes. In CFD codes, the assembly is typically modeled as a porous medium, and in CFD and finite element analysis codes, thermal radiation and conduction heat transfer within the fuel assembly is typically represented as a homogeneous block, using an effective conductivity model. Such an approach is described for the STAR-CCM+ model in Section 6.3.

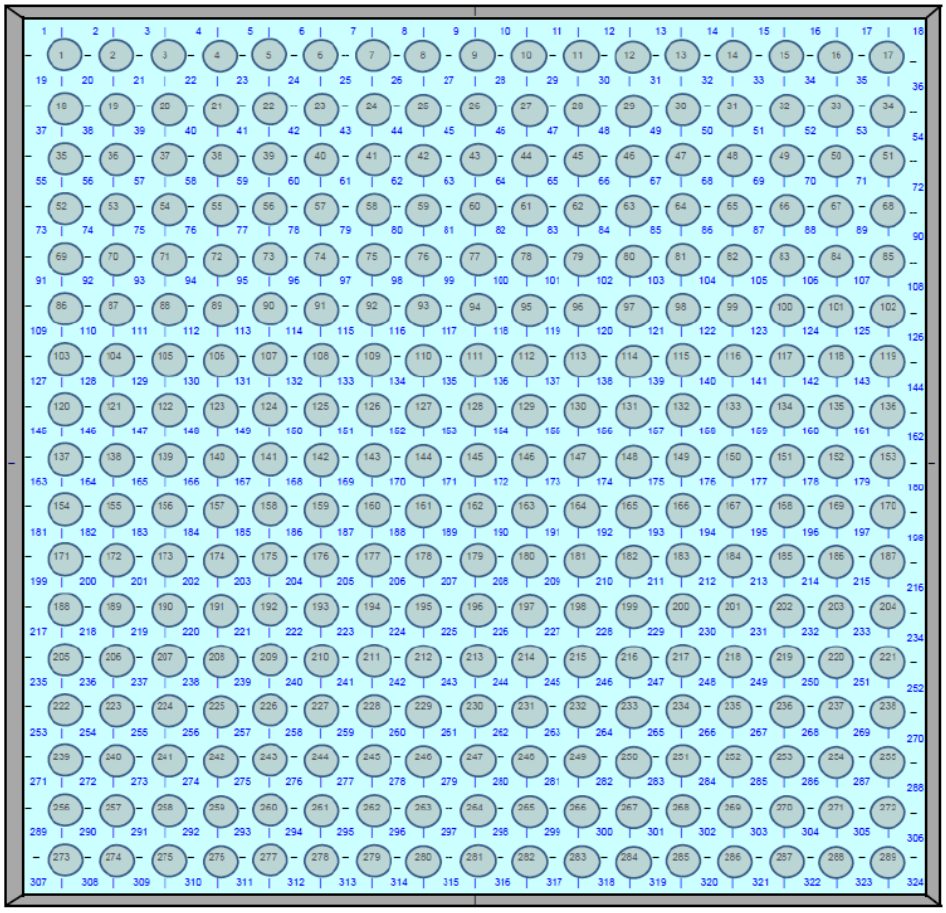

**Figure 4-4. Rod-and-Subchannel Array Diagram for COBRA-SFS Model of 17x17 Fuel Assemblies within Basket Cells (NOTE: diagram is not to scale)**

For fluid convection within the system, heat transfer is represented with a user-specified heat transfer correlation. Based on validation of the COBRA-SFS code with experimental data from horizontal and vertical test systems and canisters loaded with actual spent fuel, convection is represented with the venerable Dittus-Boelter heat transfer correlation for turbulent flow,

$$Nu = 0.023\ (Re^{0.8})(Pr^{0.4})$$

where

Nu = Nusselt number

Re = Reynolds number, based on subchannel hydraulic diameter

Pr = Prandtl number for the backfill gas

For laminar flow conditions, a Nusselt number of 3.66 has been verified as applicable to spent fuel rod arrays (Lombardo et al. 1986; Michener et al. 1995; Rector and Michener 1989). In the COBRA-SFS code, the local heat transfer coefficient is defined as the maximum of the values calculated from the laminar and turbulent correlations specified by user input. Figure 4-5 illustrates the convenient mathematical behavior of these correlations as a function of Nusselt number.

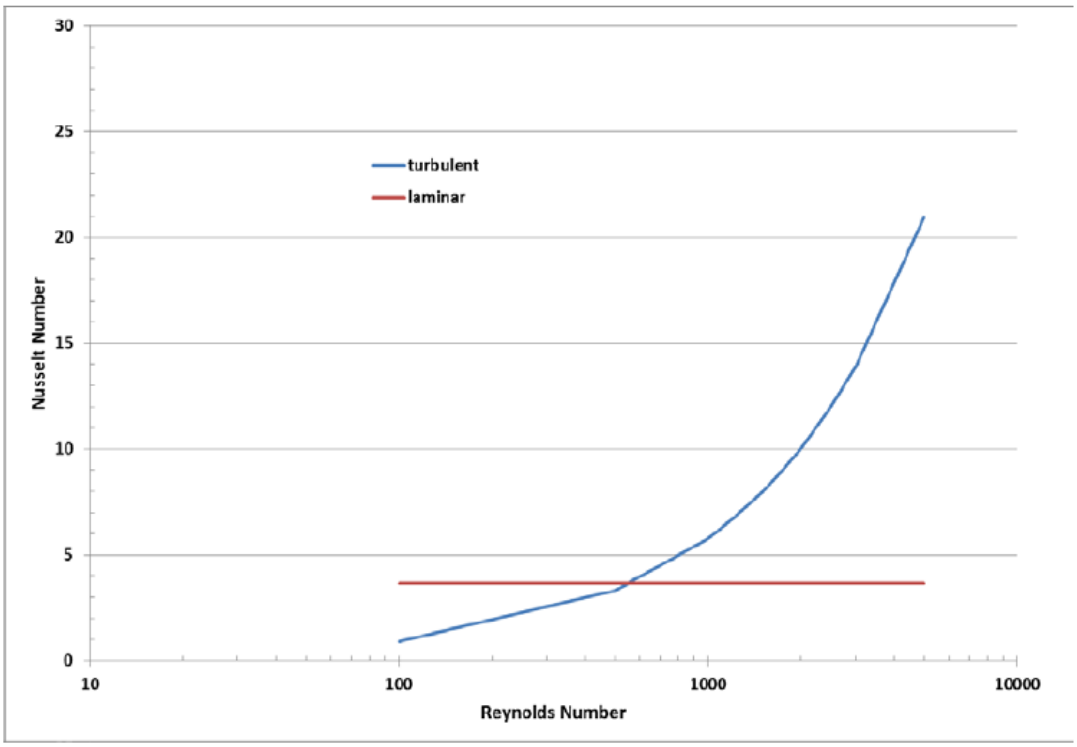


**Figure 4-5. Laminar and Turbulent Formulations for Nusselt Number**

The open regions of the support rails, as illustrated in the diagram in Figure 4-2, are represented as gas flow channels that allow a thermosiphon natural convection recirculation within the cavity, with helium gas rising through the fuel assemblies within the basket, absorbing heat from the fuel rods, then mixing in the narrow head space above the basket and sinking down the open channels in the support rails, as heat is transferred from the gas to the cooler steel wall of the canister.

## 4.3 Material Properties

Well-tested values were used for properties of solids and gases. Specific treatment of the various fill gases used in the modeling is described below.

### 4.3.1 Fill Gases

A major focus of this modeling effort was determining the effect of changing fill gases on the thermal and fluid characteristics of the MAGNASTOR system over time. Because of this, care was taken to utilize fill gas properties traceable through the National Institute of Standards and Technology (NIST). Helium properties at every pressure modeled were obtained from the NIST fluid property database (Lemmon et al. 2013).

To create models that include an air or air-helium mixture as a fill gas, an assumption of the composition of air was made. The air properties used in the modeling were developed from the NIST database properties of the individual components of air. The assumed composition of air used in the modeling is given in Table 4-1. The air-helium mixture gas properties were determined similarly using the derived air properties and the database helium properties.

**Table 4-1. Assumed Proportions of Air Components**

| Component | Proportion |
|---|---|
| Nitrogen | 0.78 |
| Oxygen | 0.21 |
| Argon | 0.01 |

### 4.3.2 Surface Properties

For thermal radiation heat transfer, surface emissivity values of the basket, tubes, and canister wall were estimated from standard material properties. Carbon steel components were specified with an emissivity of 0.8. Stainless-steel components were specified with an emissivity of 0.36. The external surface of the concrete cask was specified with an emissivity of 0.8 for thermal radiation to the environment, as it was assumed to be painted with a high emissivity paint. The fuel rod cladding surface emissivity was assumed to be 0.8, which is a typical realistic estimate for spent fuel rods. These surface emissivities are listed in Table 4-2.

**Table 4-2. Surface Emissivities**

| Material | Emissivity |
|---|---|
| Carbon Steel | 0.8 |
| Concrete Cask | 0.8 |
| Fuel Cladding | 0.8 |
| 304 Stainless Steel | 0.36 |

## 4.4 Boundary Conditions

In many storage systems, design basis analysis assumes 100°F (37.8°C) as a bounding value for daily average temperature for normal conditions of storage. NAC uses 76°F (24.4°C) in the FSAR and this same value is used in the models here. Regulatory solar loading was included as shown in the 24-hour average values listed in Table 4-3.

**Table 4-3. Solar Loading (NAC 3003)**

| Surface | Insolation over 24 hours (Btu/ft$^2$) | Insolation Rate (Btu/hr-ft$^2$) |
|---|---|---|
| Side | 1475 | 61.46 |
| Top | 2950 | 122.92 |

# 5. COBRA-SFS MODEL RESULTS

This section describes the COBRA-SFS modeling results. Section 5.1 details the models included in the analysis. Sections 5.2 to 5.11 show the findings from the models. These consist of comparisons of temperature at different locations as well as an examination of internal fluid conditions.

## 5.1 Simulation Matrix

A unique property of the COBRA-SFS code is the ability to run models in considerably less time than other CFD or thermal analysis codes and software packages. This property was leveraged during this project in order to amass a large dataset of model data. Table 5-1 shows the models created for this analysis. Each "X" signifies that a model was run at those conditions. Models were not run for conditions in which an air or partially air internal gas environment is present at year 0 heat load. Attempts at modeling these conditions led to projected temperatures outside the normal scope of spent fuel modeling efforts, producing questionable results. Additionally, the situation being simulated, that of a large leak very soon after initial loading, is highly unlikely and outside the scope of analysis for this project.

**Table 5-1. COBRA-SFS Simulation Matrix**

| Loading Configuration: | | | 3Z | | | | |
|---|---|---|---|---|---|---|---|
| Pressure | He | Air | 0 yrs | 50 yrs | 100 yrs | 200 yrs | 300 yrs |
| 7 atm | 100% | 0% | X | X | X | X | X |
| 6 atm | 100% | 0% | X | X | X | X | X |
| 5 atm | 100% | 0% | X | X | X | X | X |
| 4 atm | 100% | 0% | X | X | X | X | X |
| 3 atm | 100% | 0% | X | X | X | X | X |
| 2 atm | 100% | 0% | X | X | X | X | X |
| 1 atm | 100% | 0% | X | X | X | X | X |
| 1 atm | 50% | 50% | | X | X | X | X |
| 1 atm | 0% | 100% | | X | X | X | X |
| Loading Configuration: | | | 4Z | | | | |
| Pressure | He | Air | 0 yrs | 50 yrs | 100 yrs | 200 yrs | 300 yrs |
| 7 atm | 100% | 0% | X | X | X | X | X |
| 6 atm | 100% | 0% | X | X | X | X | X |
| 5 atm | 100% | 0% | X | X | X | X | X |
| 4 atm | 100% | 0% | X | X | X | X | X |
| 3 atm | 100% | 0% | X | X | X | X | X |
| 2 atm | 100% | 0% | X | X | X | X | X |
| 1 atm | 100% | 0% | X | X | X | X | X |
| 1 atm | 50% | 50% | | X | X | X | X |
| 1 atm | 0% | 100% | | X | X | X | X |
| Loading Configuration: | | | 1Z | | | | |
| Pressure | He | Air | 0 yrs | 50 yrs | 100 yrs | 200 yrs | 300 yrs |
| 7 atm | 100% | 0% | X | X | X | X | X |
| 6 atm | 100% | 0% | X | X | X | X | X |
| 5 atm | 100% | 0% | X | X | X | X | X |
| 4 atm | 100% | 0% | X | X | X | X | X |

| | | | | | | | |
|---|---|---|---|---|---|---|---|
| 3 atm | 100% | 0% | X | X | X | X | X |
| 2 atm | 100% | 0% | X | X | X | X | X |
| 1 atm | 100% | 0% | X | X | X | X | X |
| 1 atm | 50% | 50% | | X | X | X | X |
| 1 atm | 0% | 100% | | X | X | X | X |

## 5.2 Peak Cladding Temperature Comparisons

This section shows the peak cladding temperature (PCT) results from the COBRA-SFS models. The PCT is plotted against the overall heat load (given as an estimated time in years after installation) and separately against internal gas pressure and composition. The same PCT data are plotted for all three types of graphs; the data are only visualized differently.

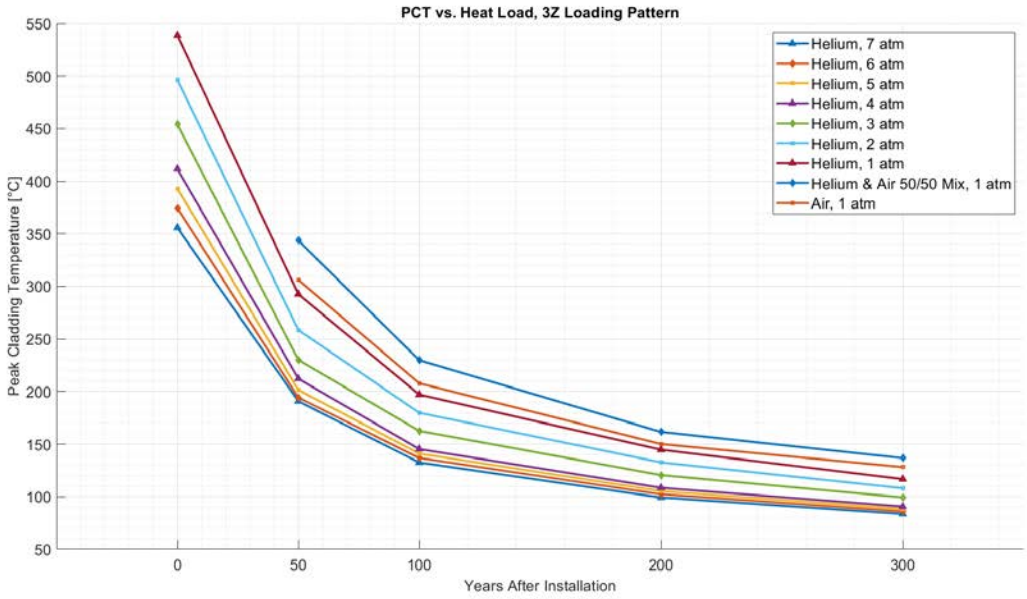


**Figure 5-1. PCT vs. Heat Load, 3Z Loading Pattern**

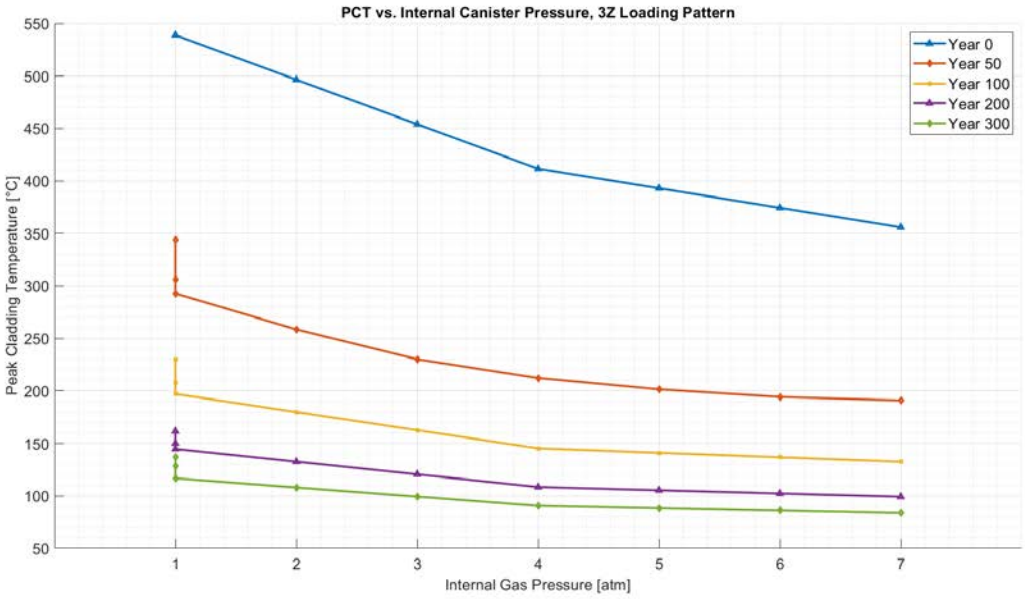


**Figure 5-2. PCT vs. Internal Canister Pressure, 3Z Loading Pattern**

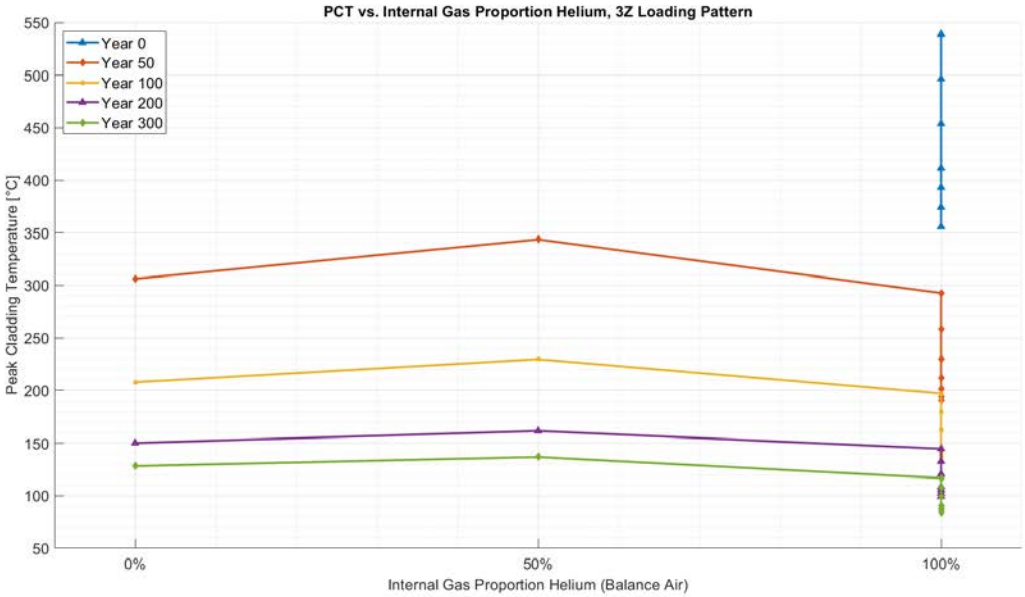


**Figure 5-3. PCT vs. Internal Gas Proportion Helium, 3Z Loading Pattern**

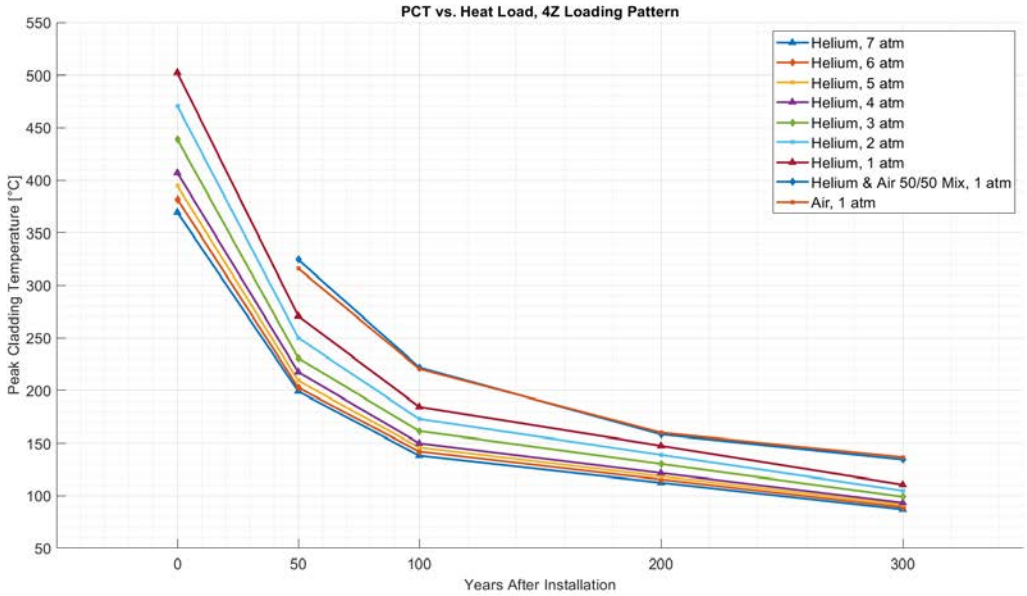


**Figure 5-4. PCT vs. Heat Load, 4Z Loading Pattern**

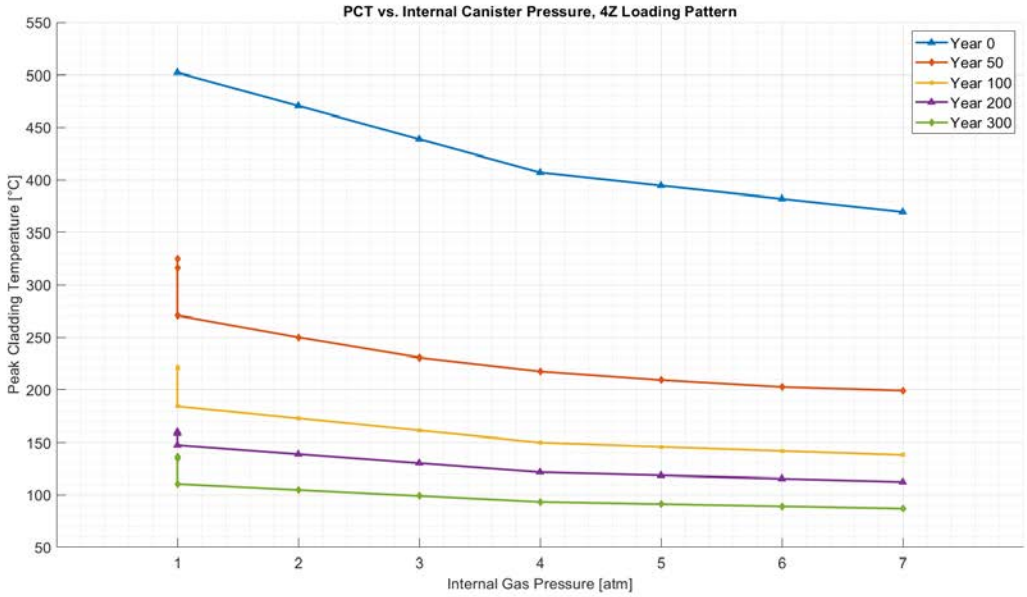


**Figure 5-5. PCT vs. Internal Canister Pressure, 4Z Loading Pattern**

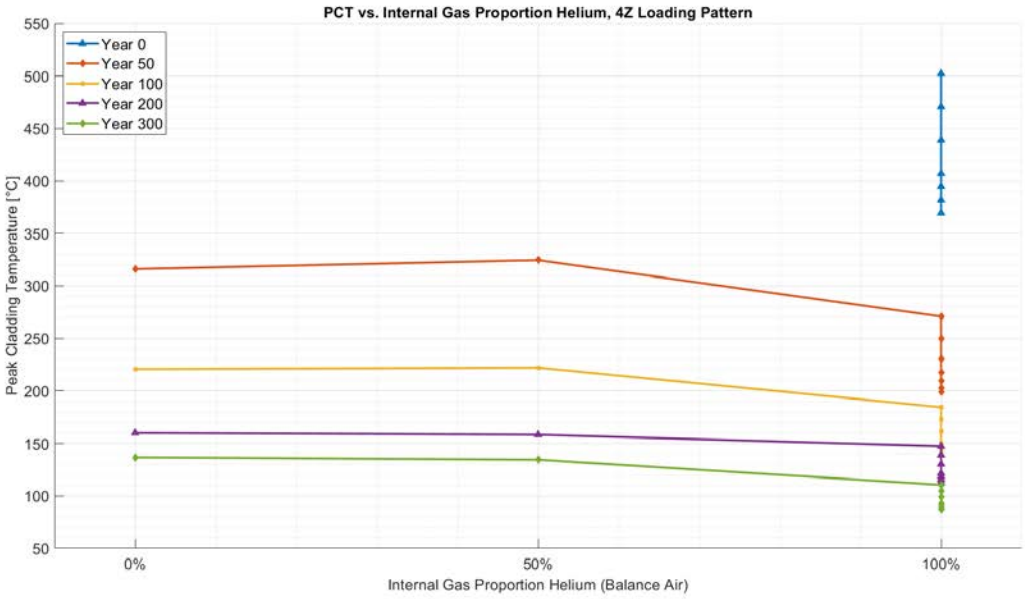


**Figure 5-6. PCT vs. Internal Gas Proportion Helium, 4Z Loading Pattern**

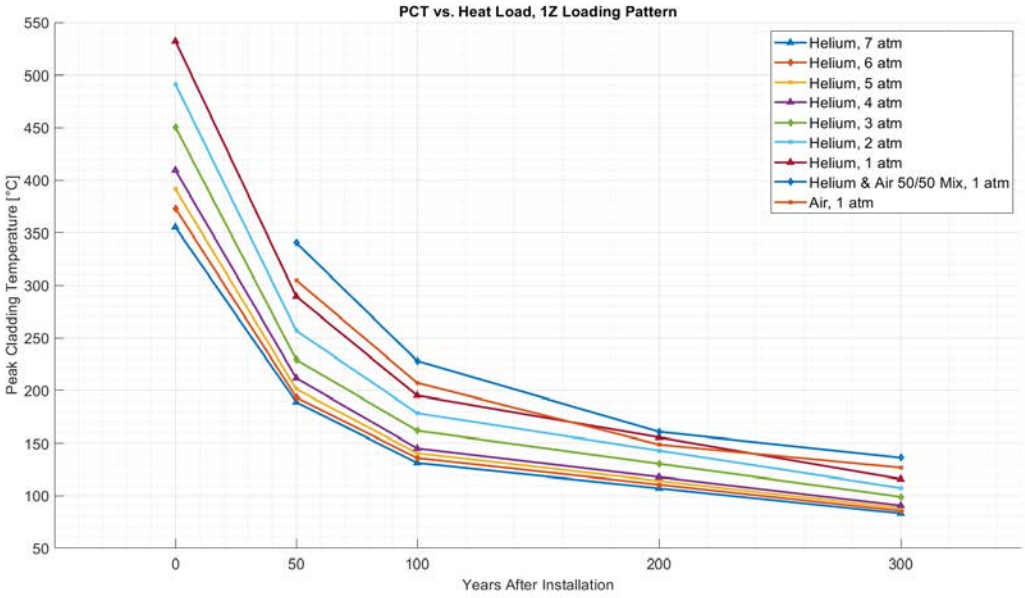


**Figure 5-7. PCT vs. Heat Load, 1Z Loading Pattern**

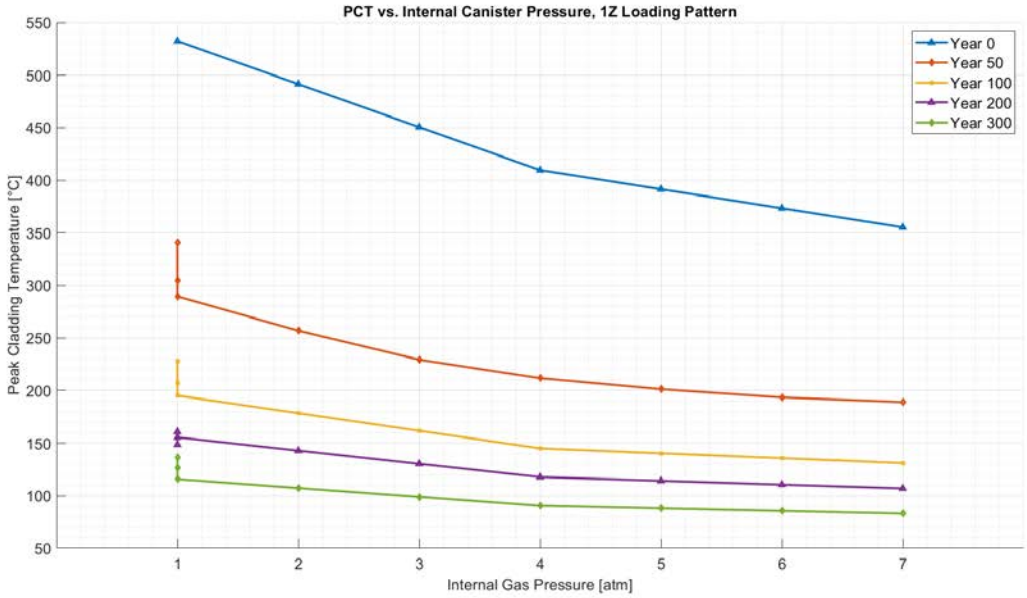


**Figure 5-8. PCT vs Internal Canister Pressure, 1Z Loading Pattern**

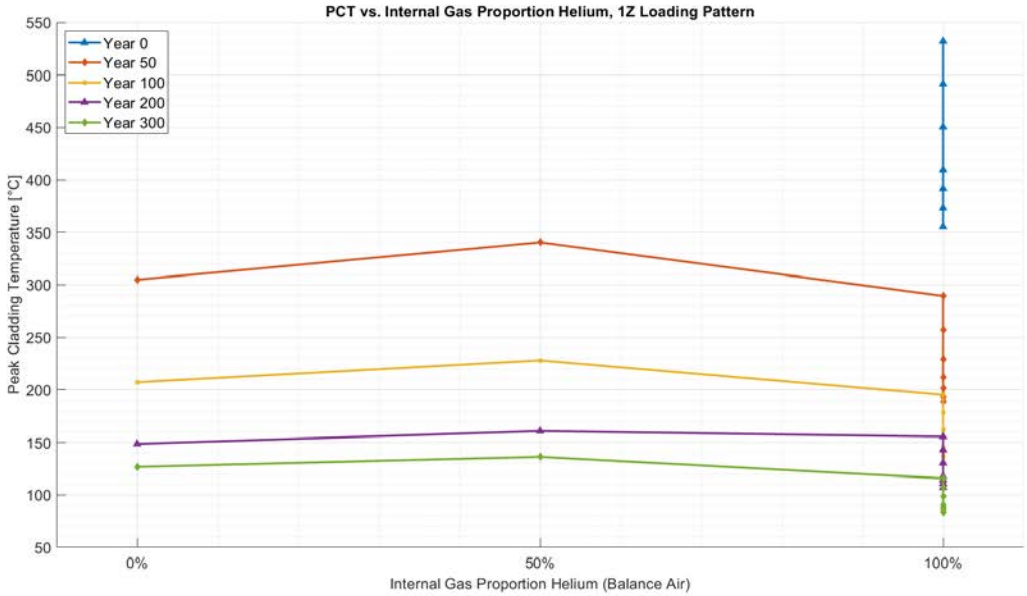


**Figure 5-9. PCT vs Internal Gas Proportion Helium, 1Z Loading Pattern**

## 5.3 Average Cladding Temperature Comparisons

This section shows the average cladding temperature results from the COBRA-SFS models. The temperature is plotted against the overall heat load (given as an estimated time in years after installation)

and separately against internal gas pressure and composition. The same temperature data are plotted for all three types of graphs; the data are only visualized differently.

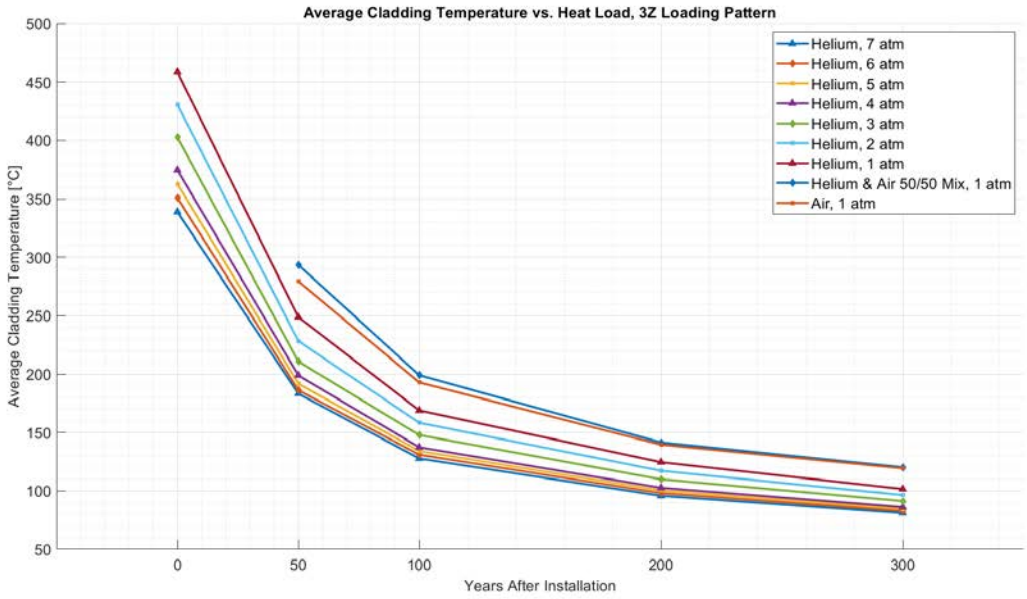


**Figure 5-10. Average Cladding Temperature vs. Heat Load, 3Z Loading Pattern**

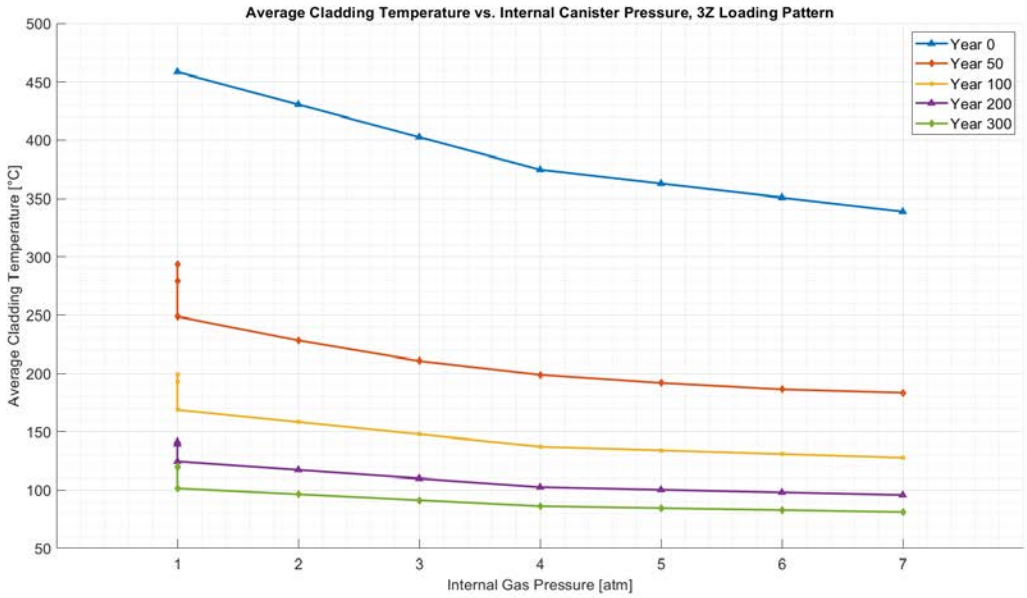


**Figure 5-11. Average Cladding Temperature vs. Heat Load, 3Z Loading Pattern**

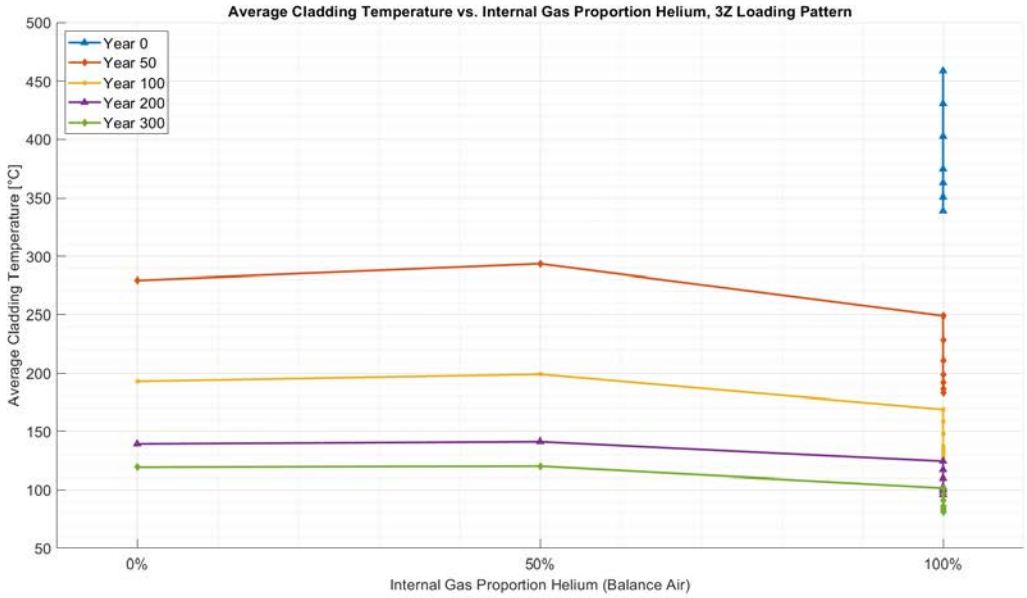


**Figure 5-12. Average Cladding Temperature vs. Internal Gas Proportion Helium, 3Z Loading Pattern**

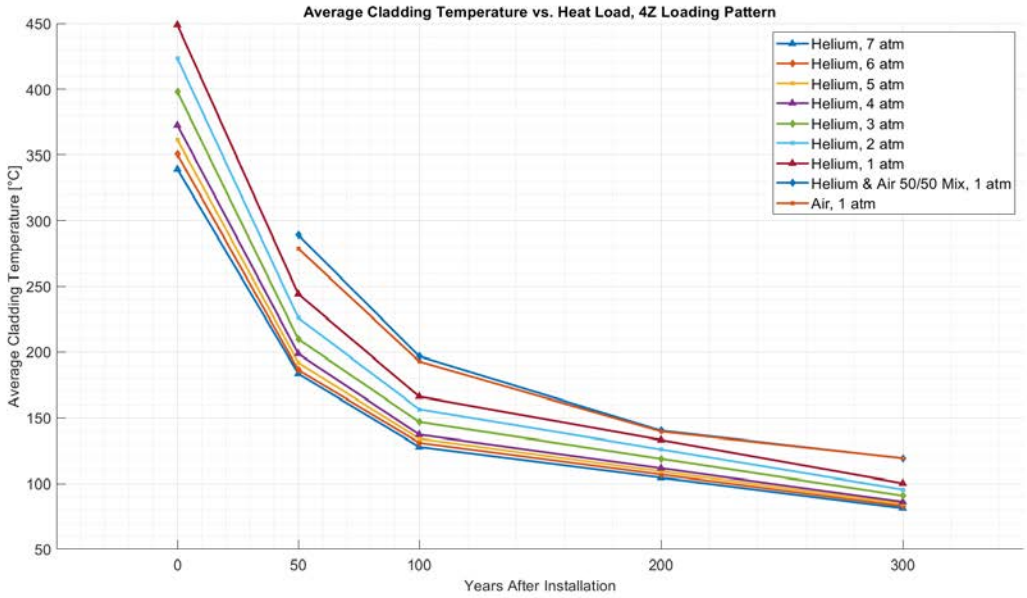


**Figure 5-13. Average Cladding Temperature vs. Heat Load, 4Z Loading Pattern**

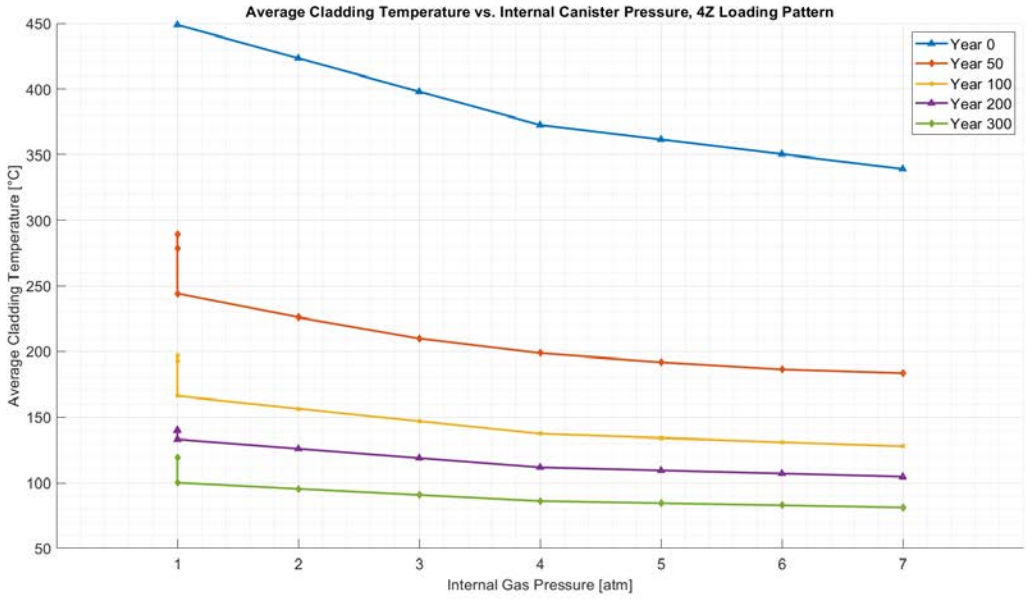


**Figure 5-14. Average Cladding Temperature vs. Internal Canister Pressure, 4Z Loading Pattern**

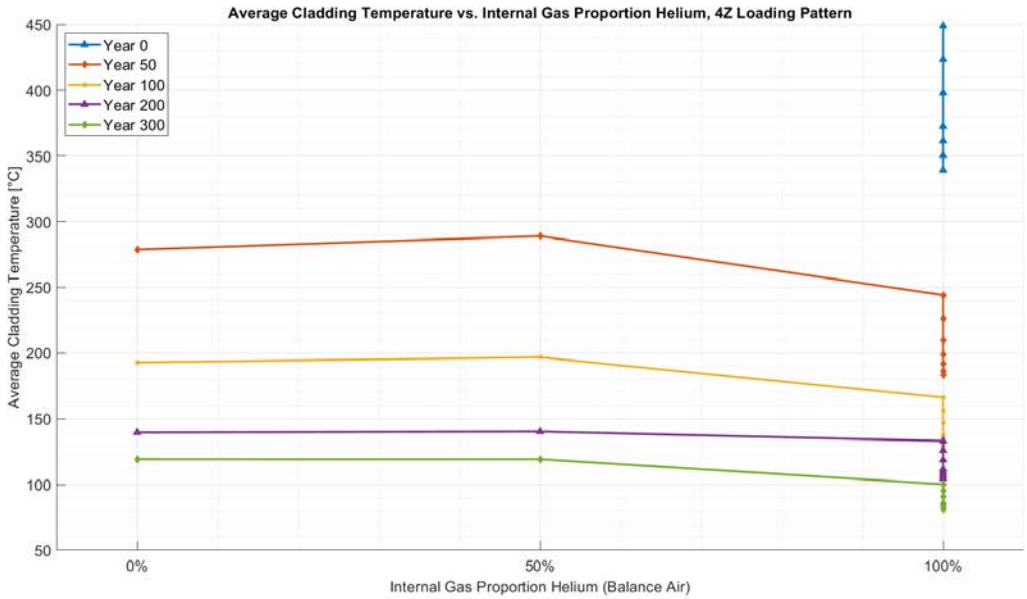


**Figure 5-15. Average Cladding Temperature vs. Internal Gas Proportion Helium, 4Z Loading Pattern**

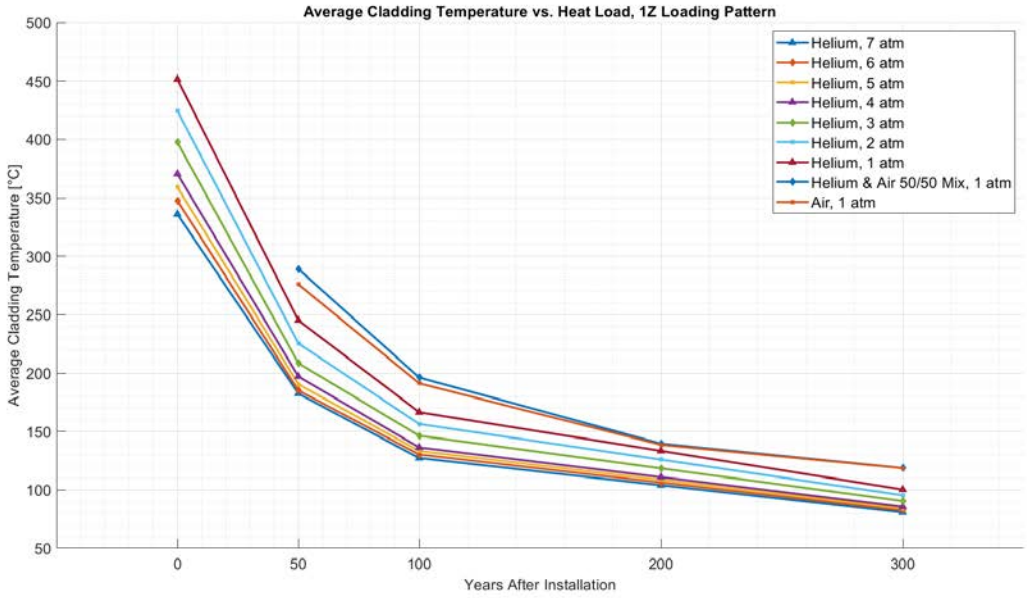


**Figure 5-16. Average Cladding Temperature vs. Heat Load, 1Z Loading Pattern**

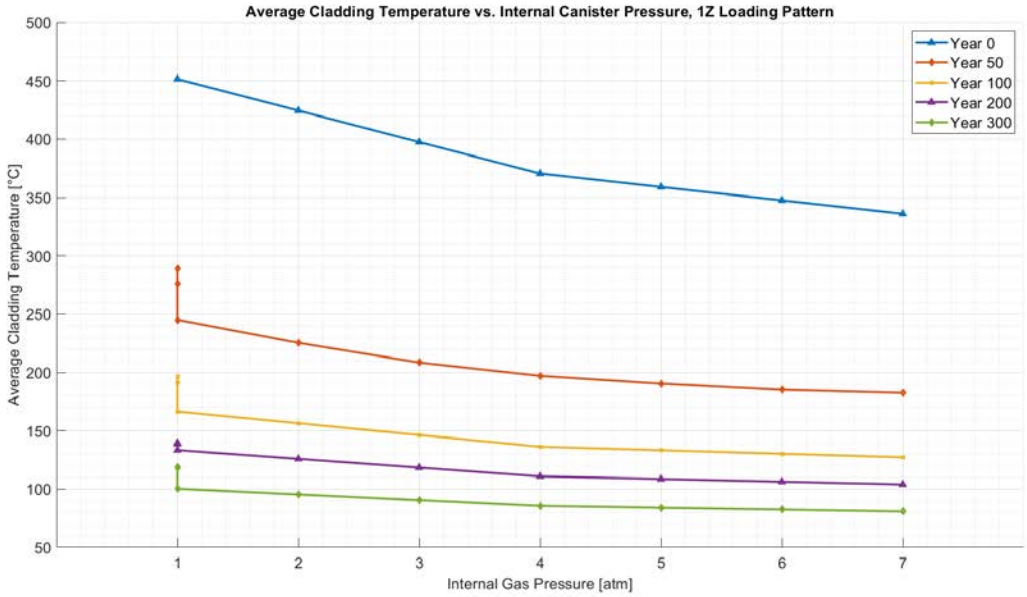


**Figure 5-17. Average Cladding Temperature vs. Internal Canister Pressure, 1Z Loading Pattern**

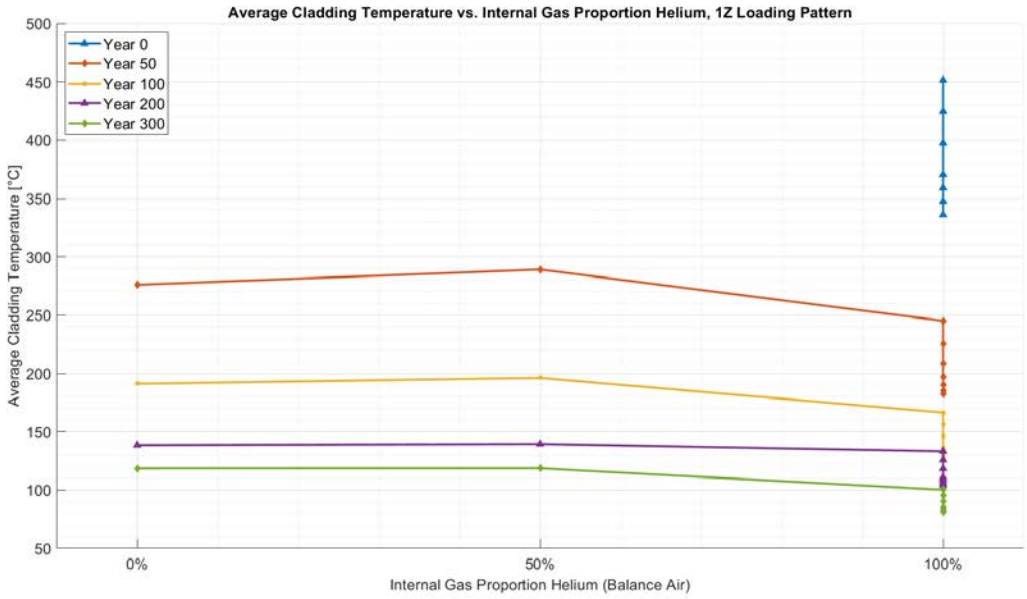


**Figure 5-18. Average Cladding Temperature vs. Internal Gas Proportion Helium, 1Z Loading Pattern**

## 5.4 Average Lid Temperature Comparisons

This section shows the average canister lid temperature results from the COBRA-SFS models. The lid temperature is plotted against the overall heat load (given as an estimated time in years after installation). Due to limitations of the COBRA-SFS code, only the average lid temperature is available to be analyzed.

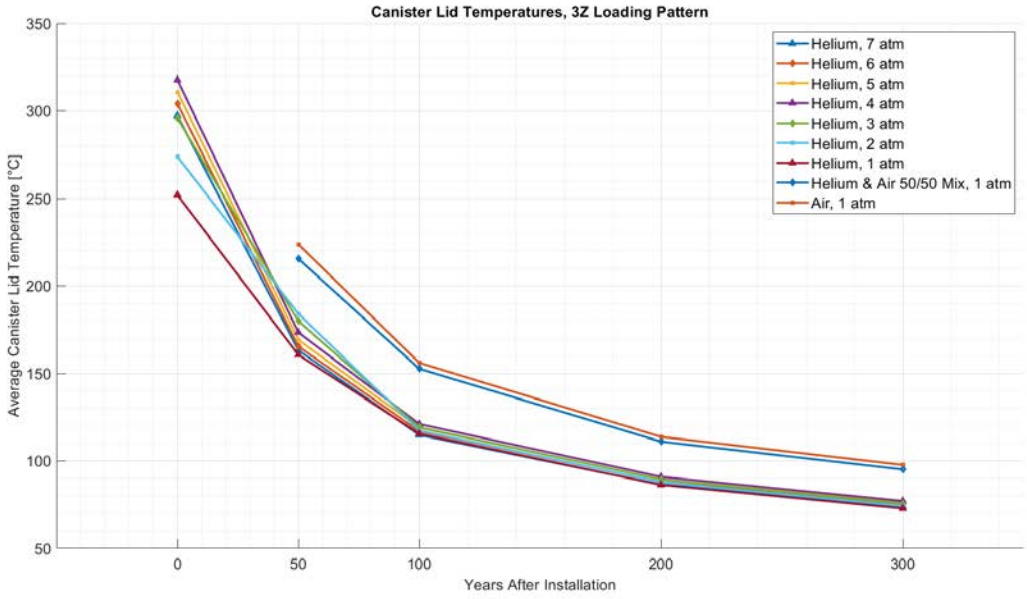


**Figure 5-19. Canister Lid Temperatures, 3Z Loading Pattern**

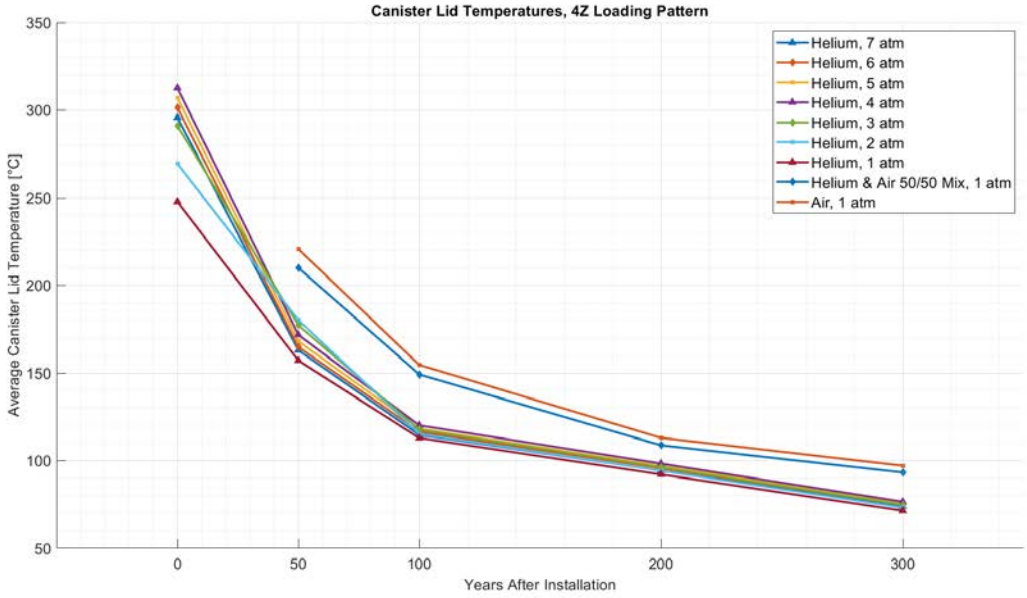


**Figure 5-20. Canister Lid Temperatures, 4Z Loading Pattern**

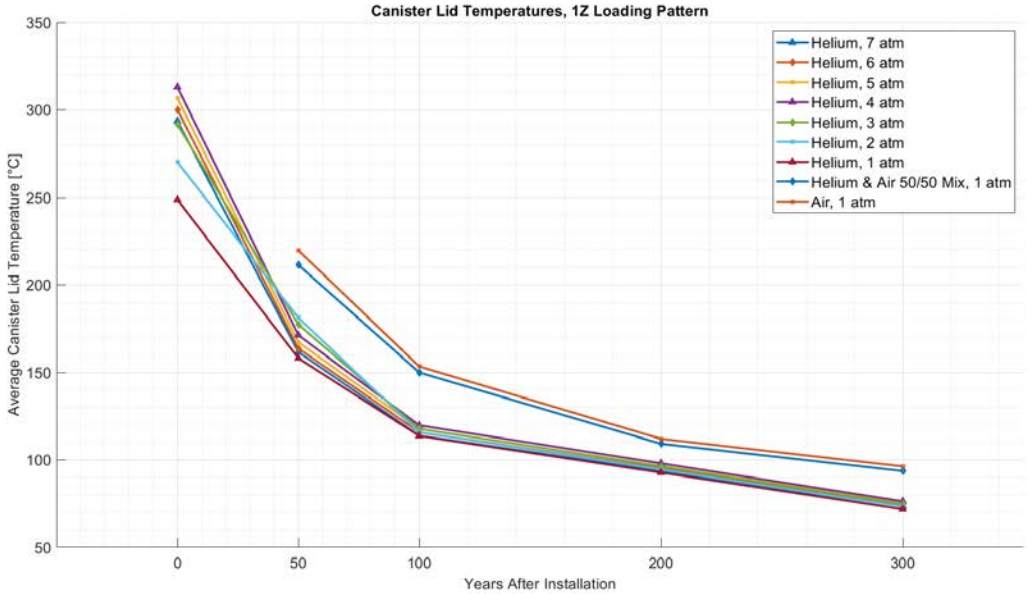


**Figure 5-21. Canister Lid Temperatures, 1Z Loading Pattern**

## 5.5 Average Base Temperature Comparisons

This section shows the average canister base temperature results from the COBRA-SFS models. The base temperature is plotted against the overall heat load (given as an estimated time in years after installation).

Due to limitations of the COBRA-SFS code, only the average base temperature is available to be analyzed.

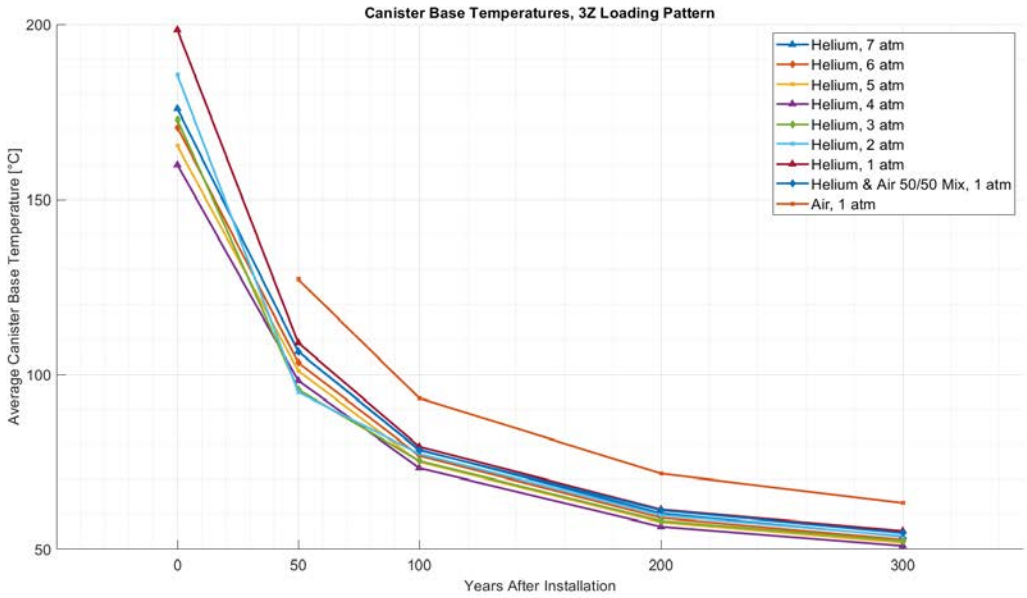


**Figure 5-22. Canister Base Temperatures, 3Z Loading Pattern**

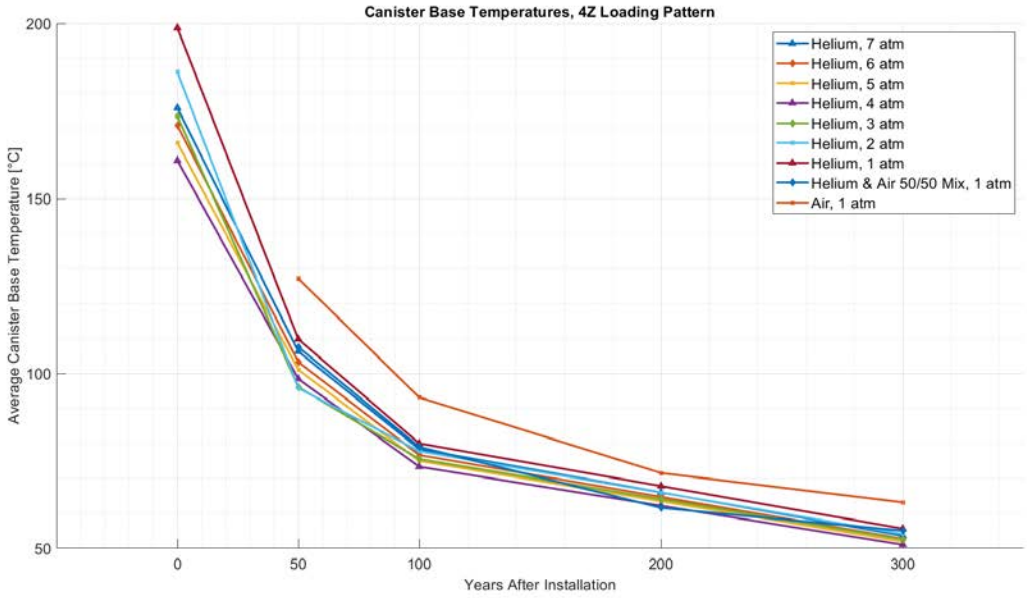


**Figure 5-23. Canister Base Temperatures, 4Z Loading Pattern**

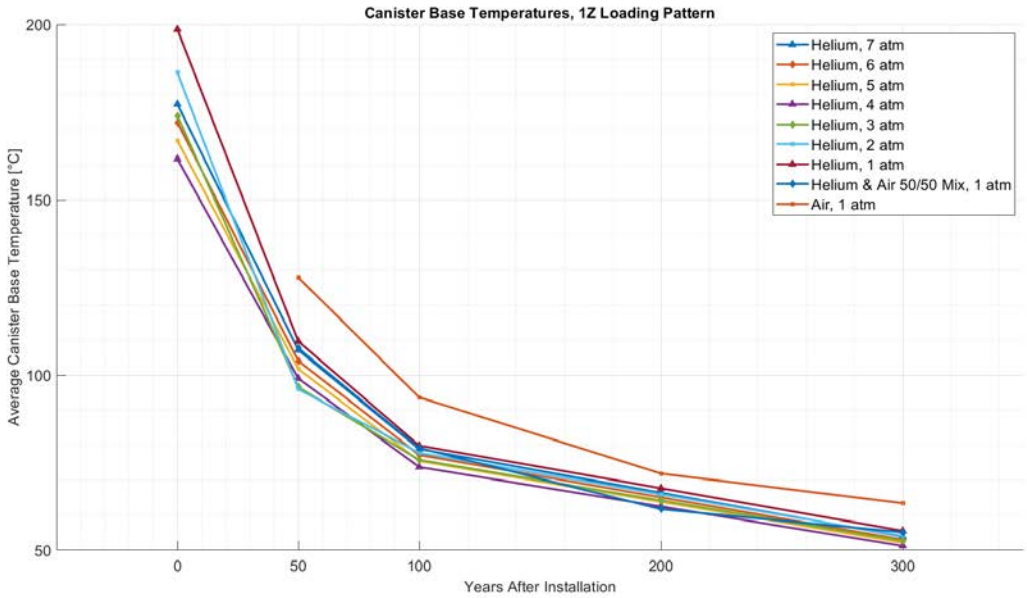


**Figure 5-24. Canister Base Temperatures, 1Z Loading Pattern**

## 5.6 Base and Lid Temperature Difference Comparisons

This section compares the results from the previous two sections, the average lid and average base temperatures from the COBRA-SFS models. The data plotted are the arithmetic differences between the canister lid average temperature and the canister base average temperature for each case.

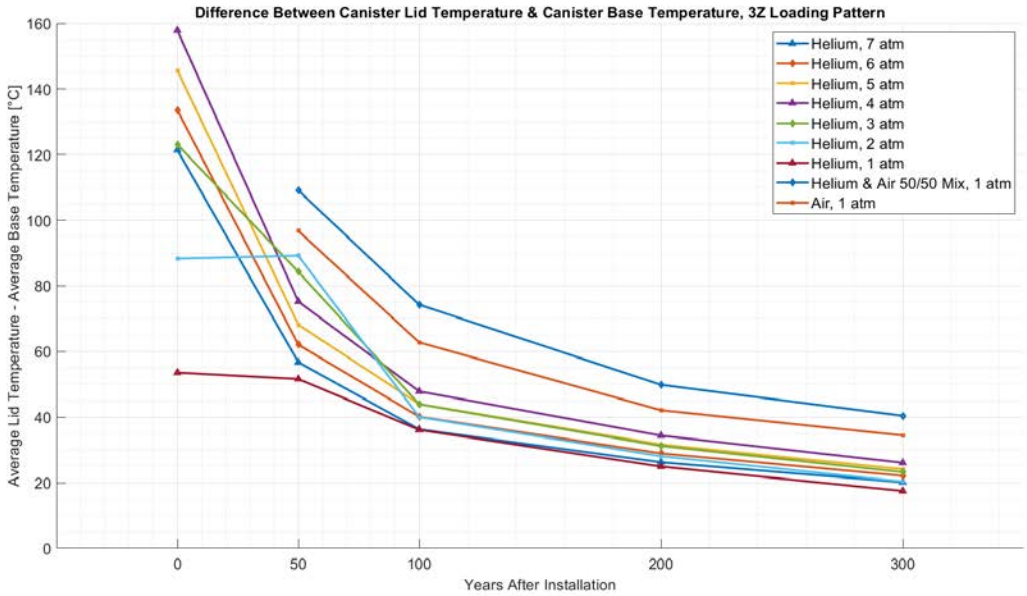


**Figure 5-25. Difference Between Canister Lid Temperature & Canister Base Temperature, 3Z Loading Pattern**

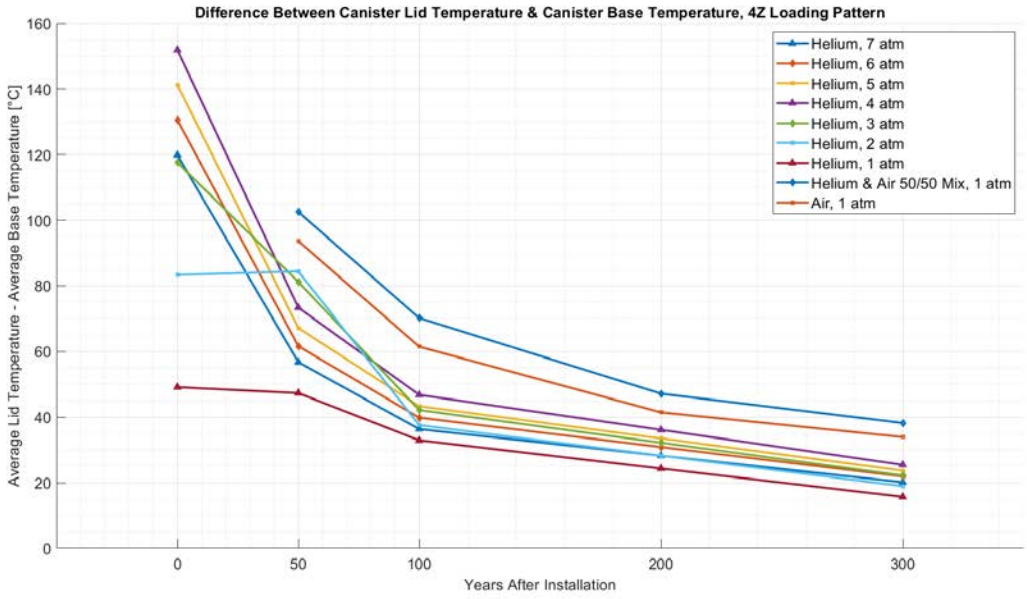


**Figure 5-26. Difference Between Canister Lid Temperature & Canister Base Temperature, 4Z Loading Pattern**

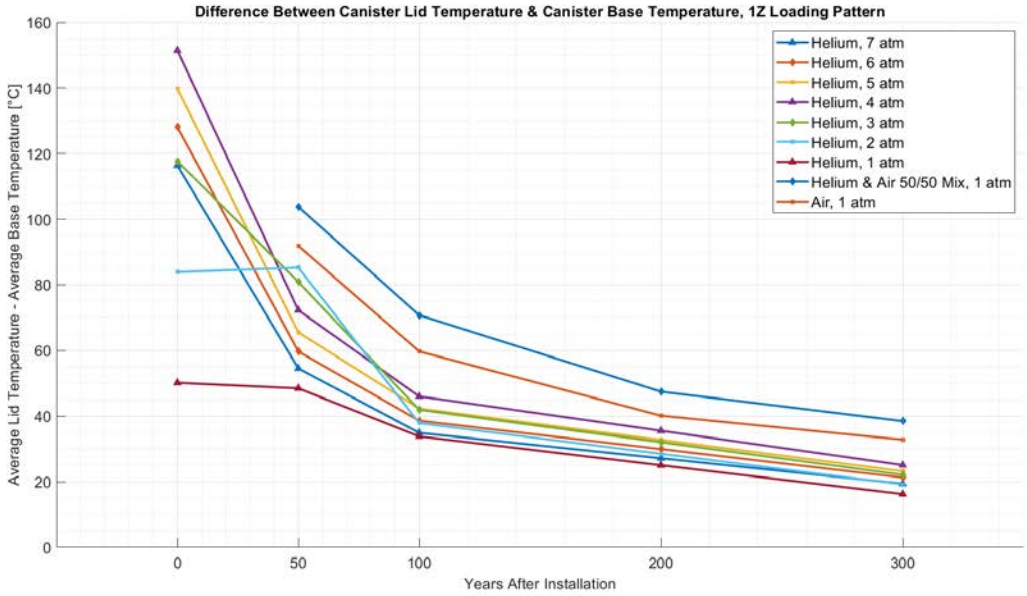


**Figure 5-27. Difference Between Canister Lid Temperature & Canister Base Temperature, 1Z Loading Pattern**

## 5.7 Average Canister Temperature Comparisons

This section shows the average canister wall temperature results from the COBRA-SFS models. The wall temperature is plotted against the overall heat load (given as an estimated time in years after installation).

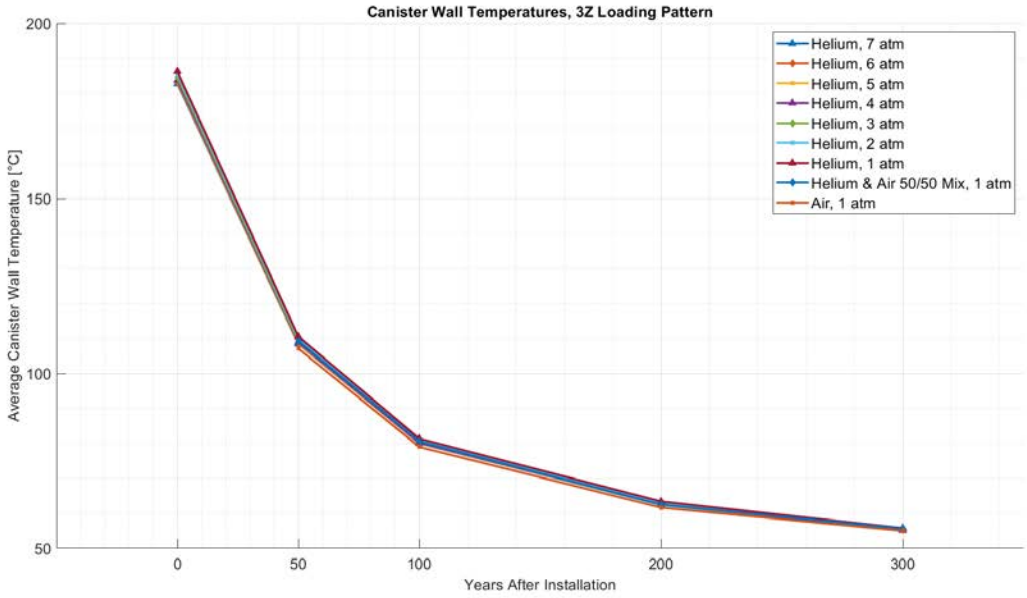


**Figure 5-28. Canister Wall Temperatures, 3Z Loading Pattern**

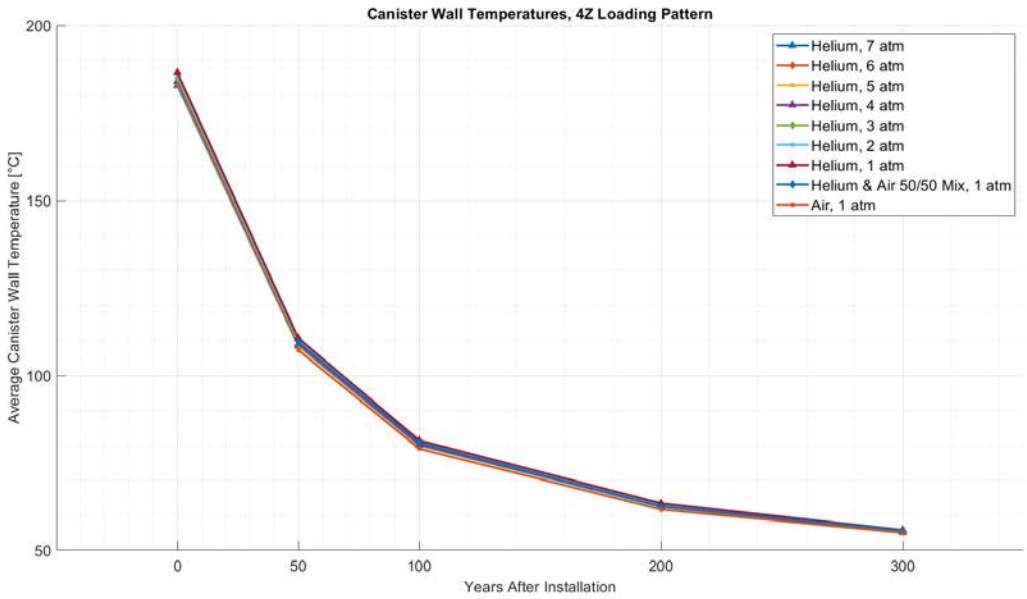


**Figure 5-29. Canister Wall Temperatures, 4Z Loading Pattern**

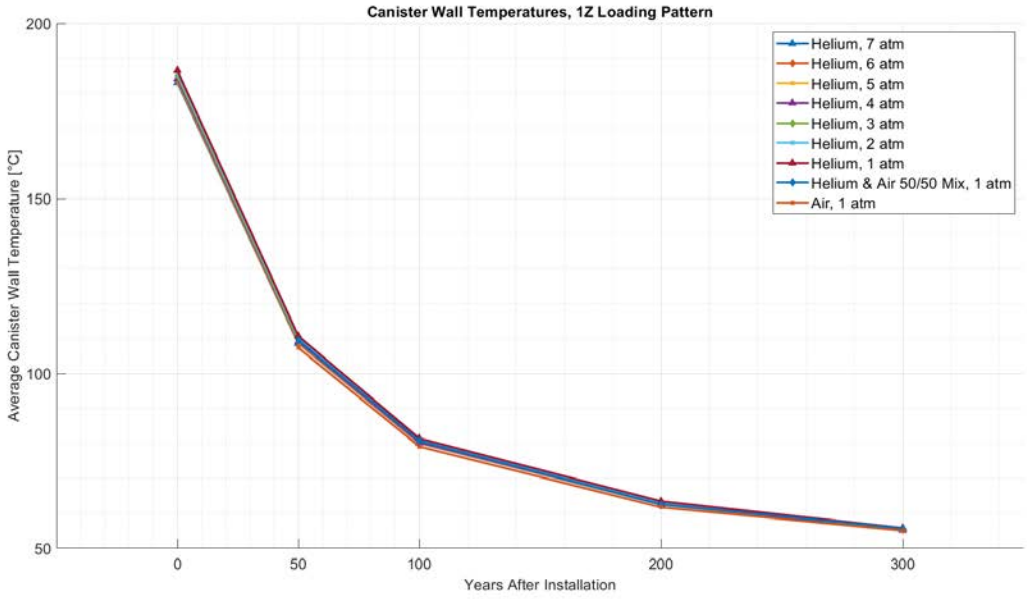


**Figure 5-30. Canister Wall Temperatures, 1Z Loading Pattern**

## 5.8 Average Gas Temperature Comparisons

This section shows the average canister gas temperature results from the COBRA-SFS models. The gas temperature is plotted against the overall heat load (given as an estimated time in years after installation). The gas temperature is averaged for a single assembly, assembly 19, located in the center of the MAGNASTOR PWR basket.

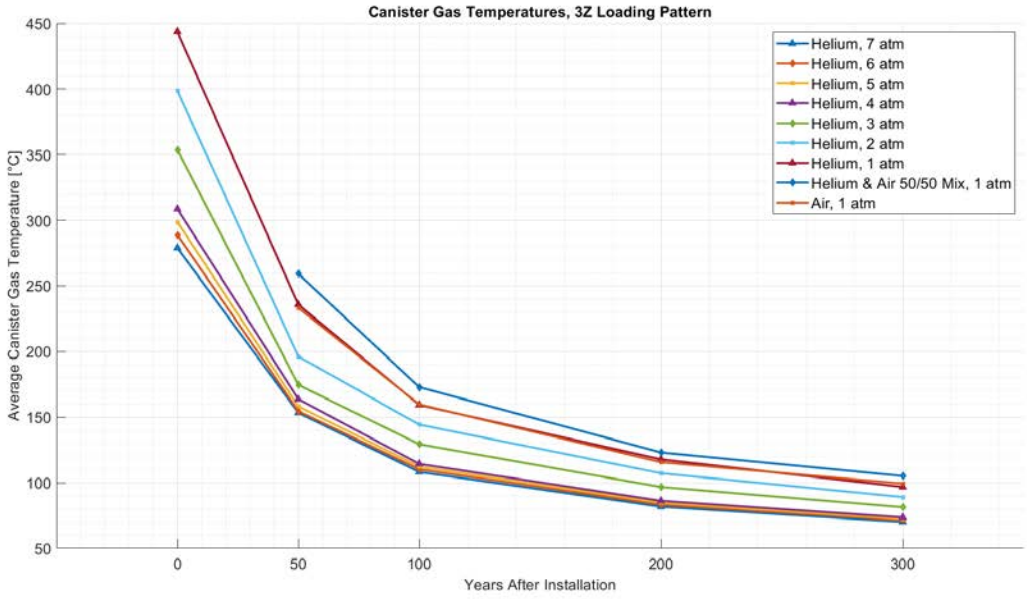


**Figure 5-31. Canister Gas Temperature, 3Z Loading Pattern**

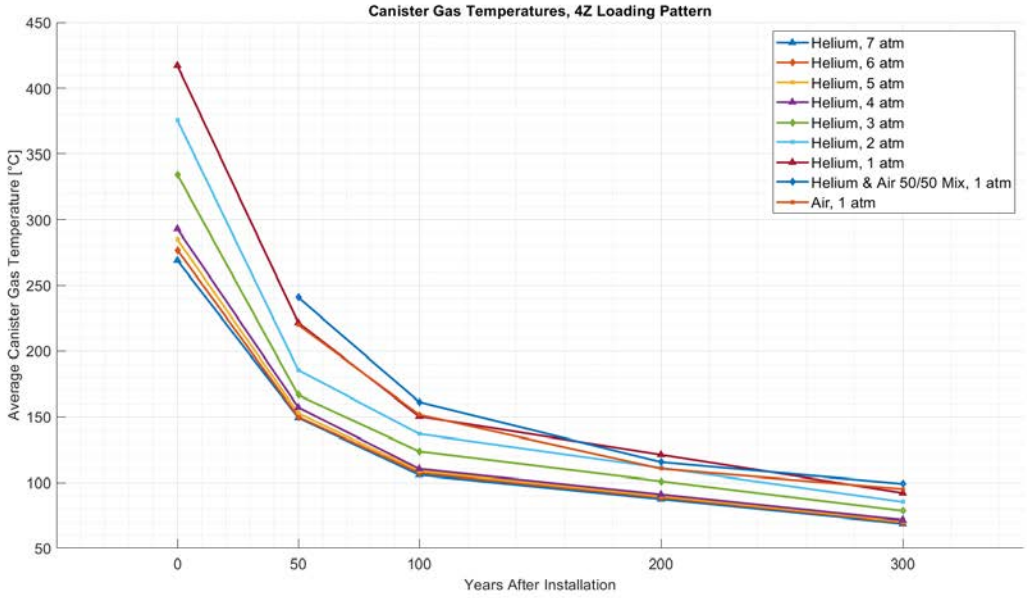


**Figure 5-32. Canister Gas Temperature, 4Z Loading Pattern**

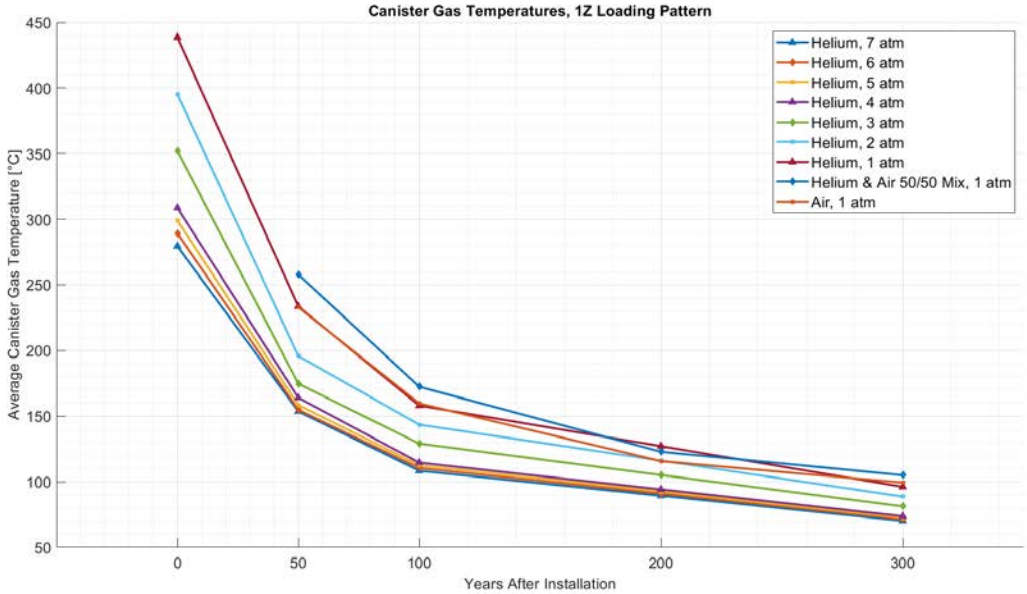


**Figure 5-33. Canister Gas Temperature, 1Z Loading Pattern**

## 5.9 Peak Rod Temperature Comparisons

This section shows the average temperature results for the peak temperature rod in each COBRA-SFS model. The rod temperature is plotted against the overall heat load (given as an estimated time in years after installation).

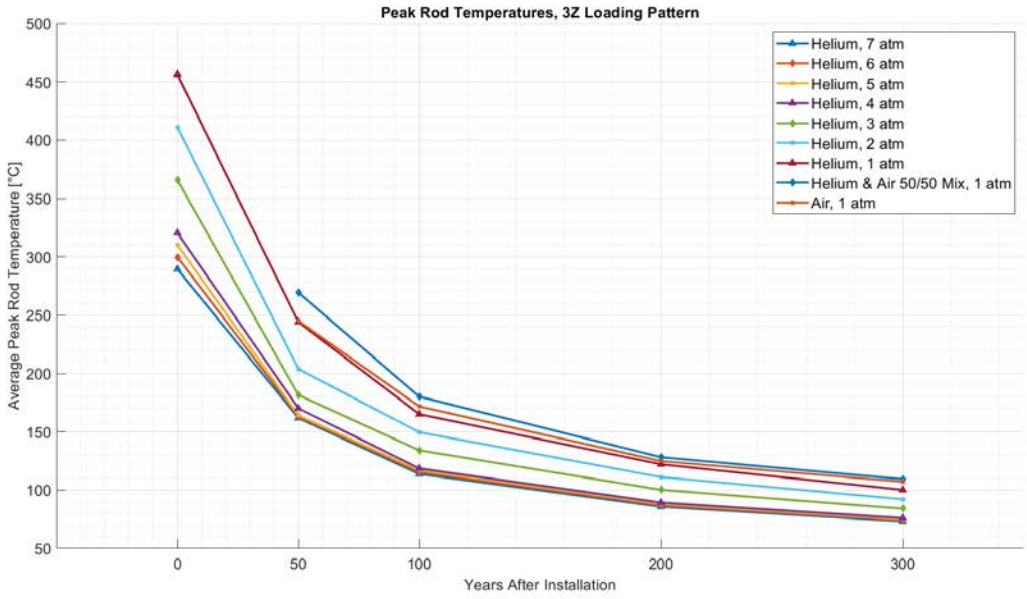


**Figure 5-34. Peak Rod Temperatures, 3Z Loading Pattern**

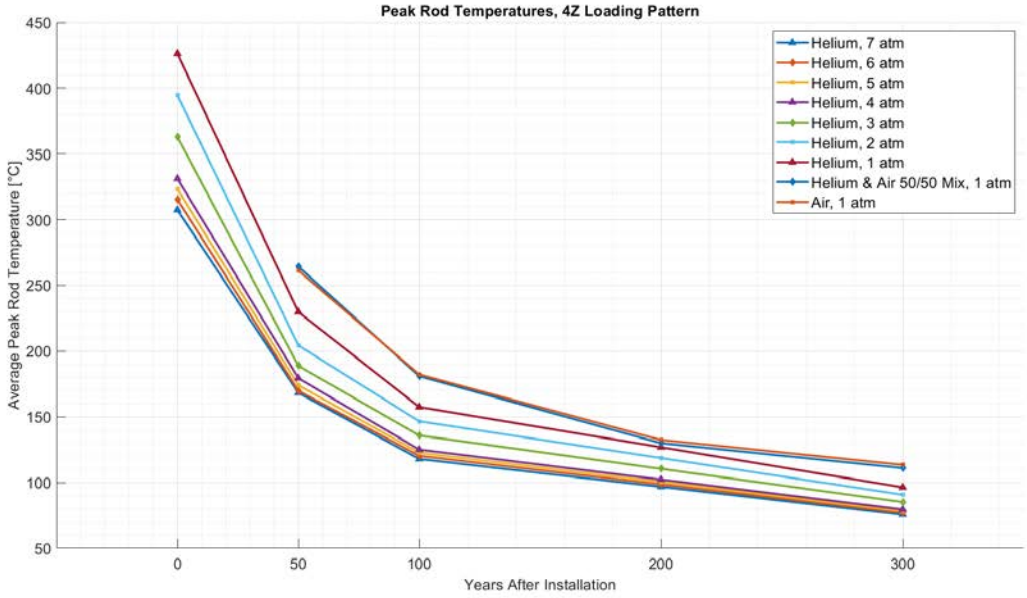


**Figure 5-35. Peak Rod Temperatures, 4Z Loading Pattern**

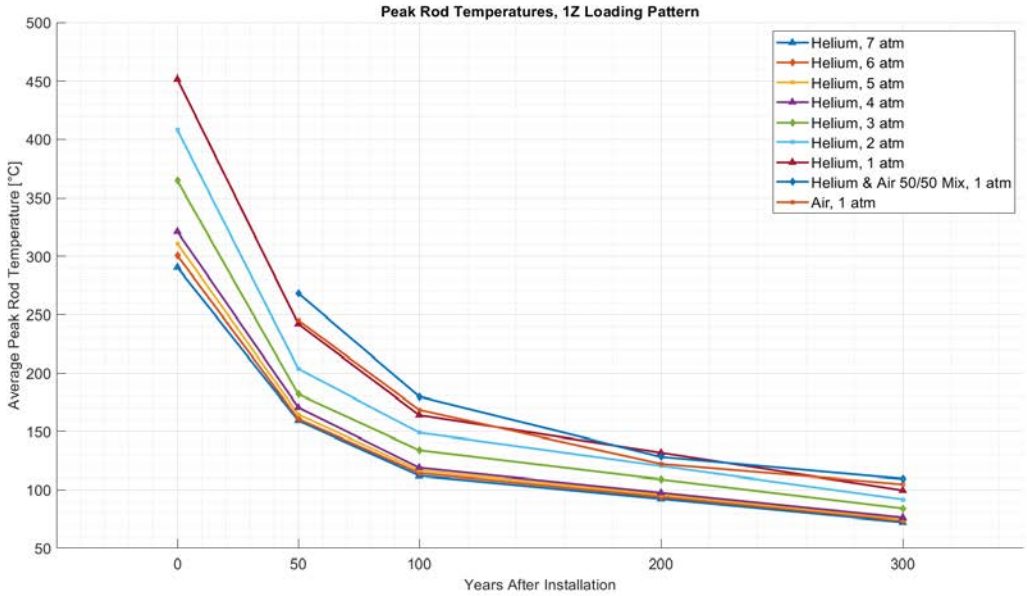


**Figure 5-36. Peak Rod Temperatures, 1Z Loading Pattern**

## 5.10 Cold Rod Temperature Comparisons

This section shows the average temperature results for the lowest temperature rod in each COBRA-SFS model. The rod temperature is plotted against the overall heat load (given as an estimated time in years after installation).

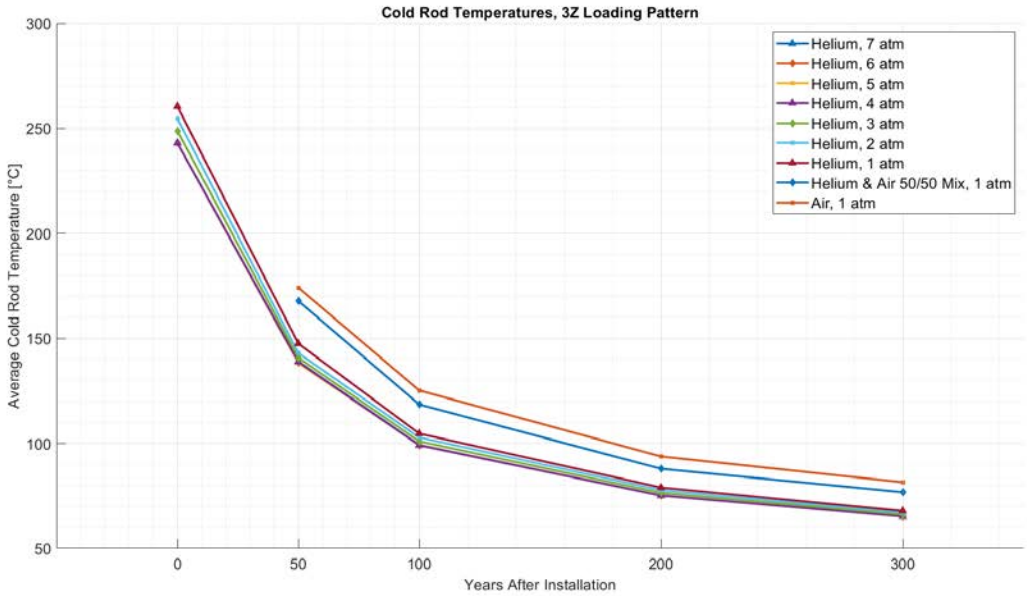


**Figure 5-37. Cold Rod Temperatures, 3Z Loading Pattern**

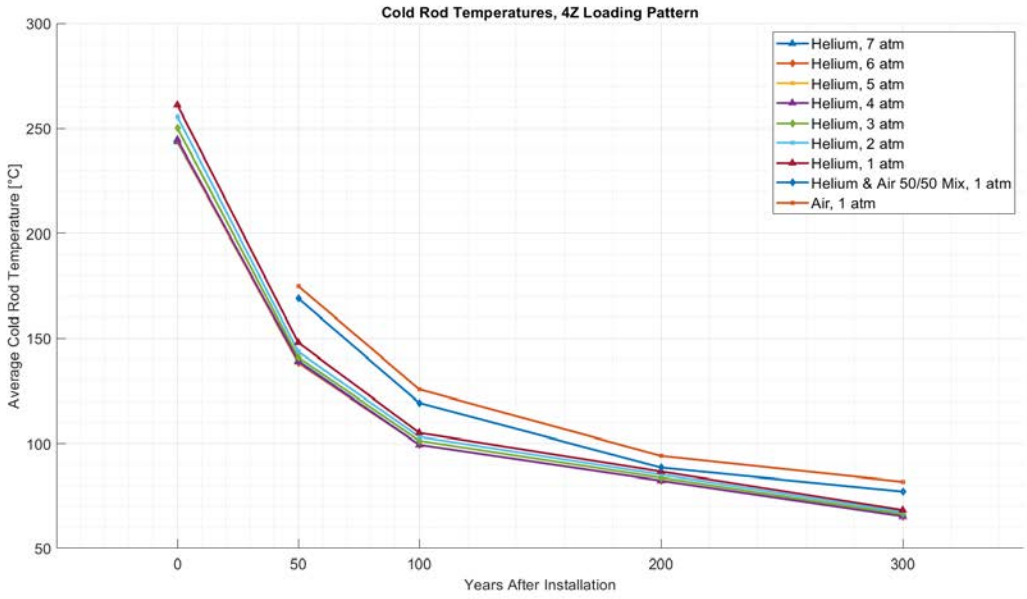


**Figure 5-38. Cold Rod Temperatures, 4Z Loading Pattern**

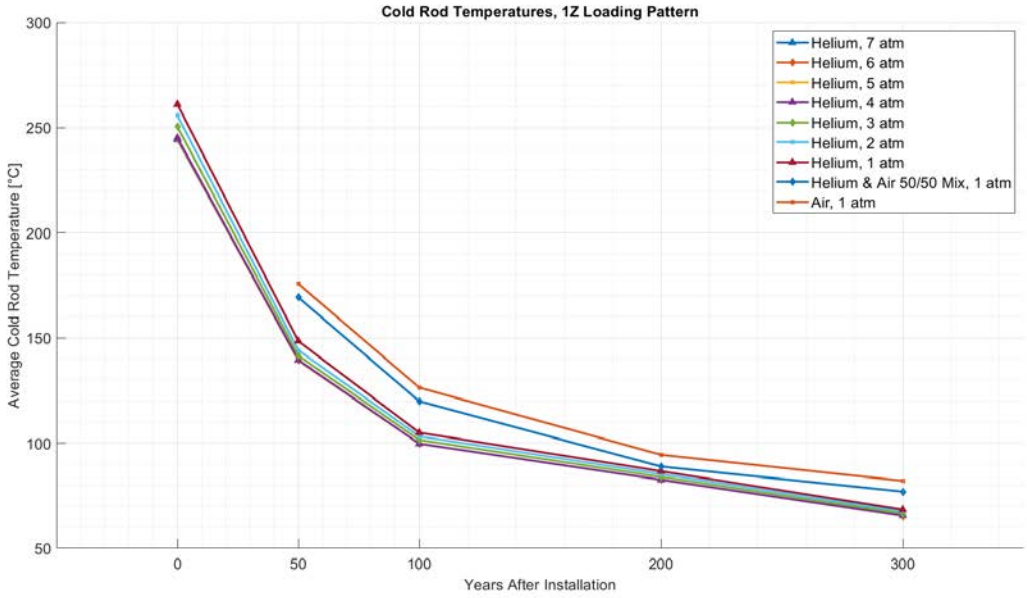


**Figure 5-39. Cold Rod Temperatures, 1Z Loading Pattern**

## 5.11 Fluid Velocity Comparisons

This section shows the average downcomer fluid velocities from the COBRA-SFS models. The fluid velocity is plotted against the overall heat load (given as an estimated time in years after installation).

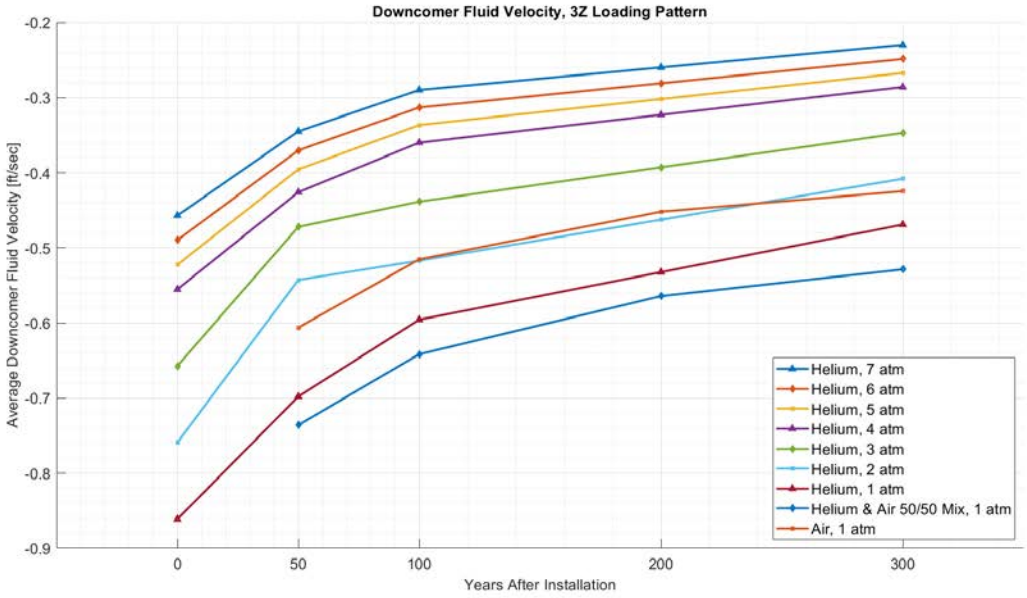


**Figure 5-40. Downcomer Fluid Velocity, 3Z Loading Pattern**

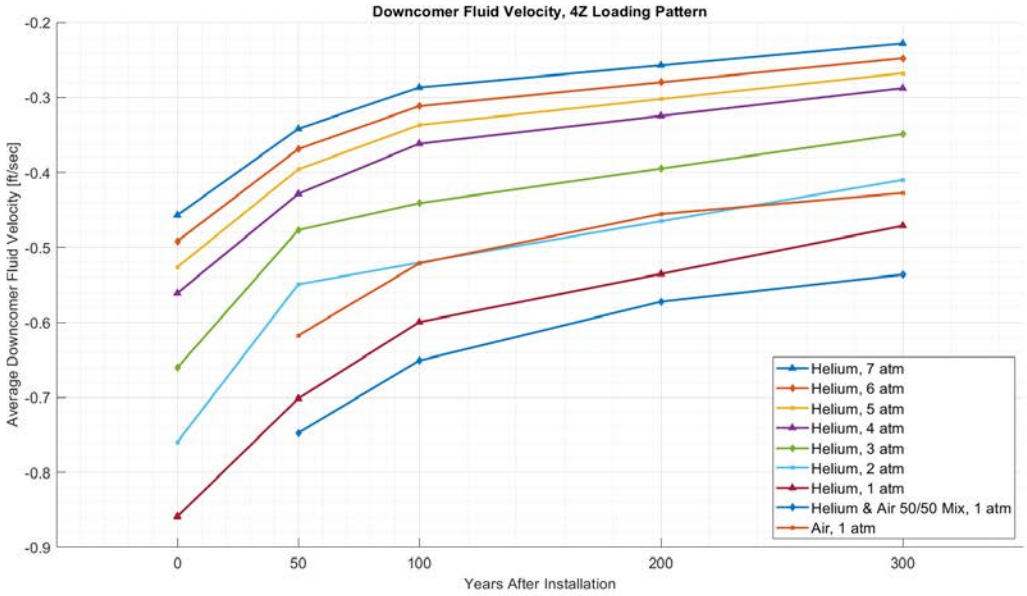


**Figure 5-41. Downcomer Fluid Velocity, 4Z Loading Pattern**

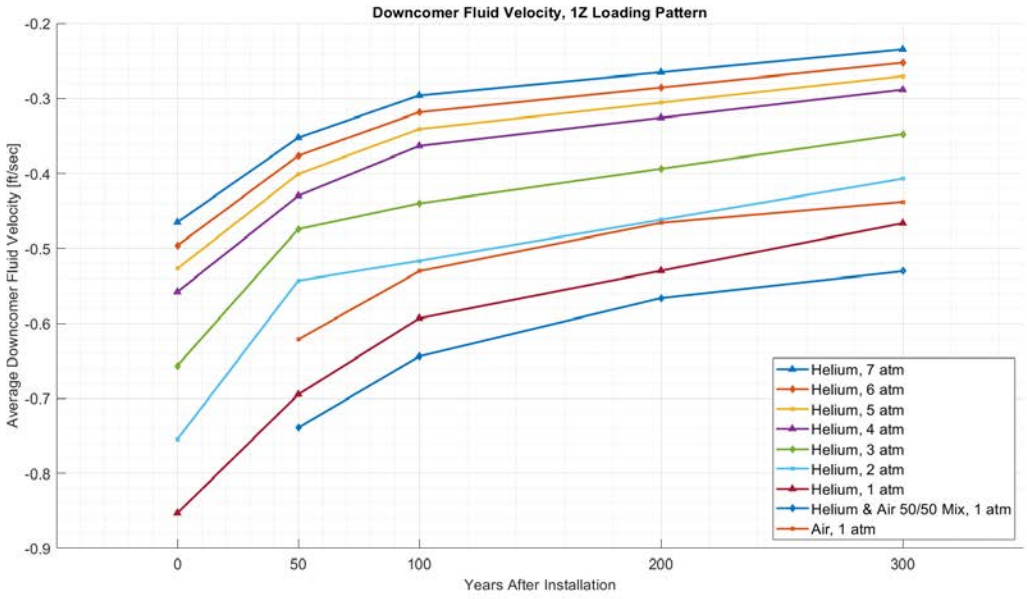


**Figure 5-42. Downcomer Fluid Velocity, 1Z Loading Pattern**

This section shows the annulus fluid velocities from a selection of the COBRA-SFS models. Only the 3Z loading pattern in shown, both for brevity and because no significant differences were observed between the three loading patterns. The fluid velocity appears to be strongly correlated to heat load, irrespective of pressure and gas composition.

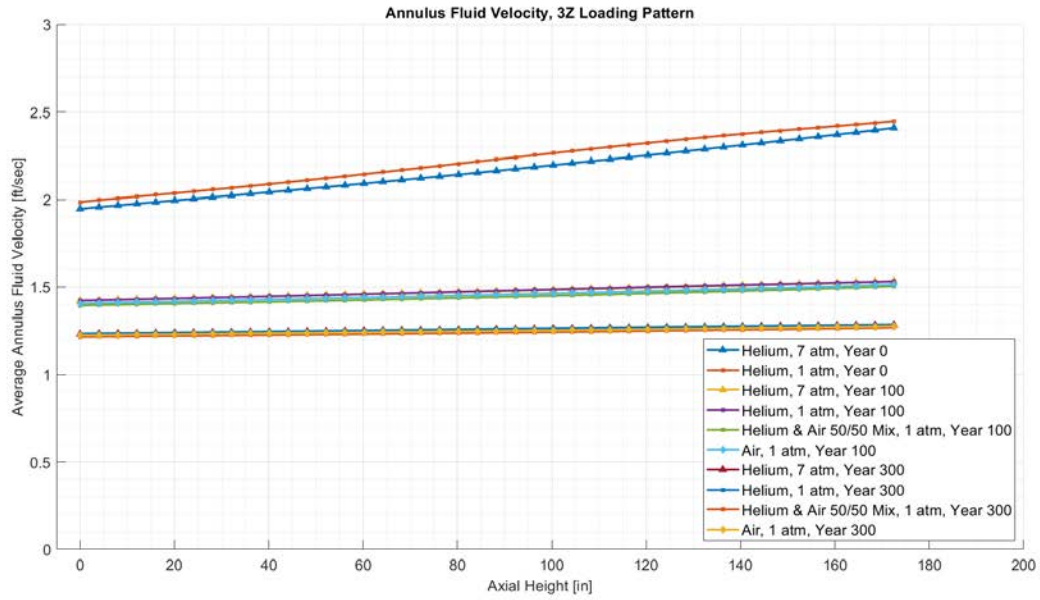


**Figure 5-43. Annulus Fluid Velocity, 3Z Loading Pattern**

## 5.12 Fluid Mass Flux Comparisons

This section shows the average downcomer mass flux from the COBRA-SFS models. The mass flux is plotted against the overall heat load (given as an estimated time in years after installation).

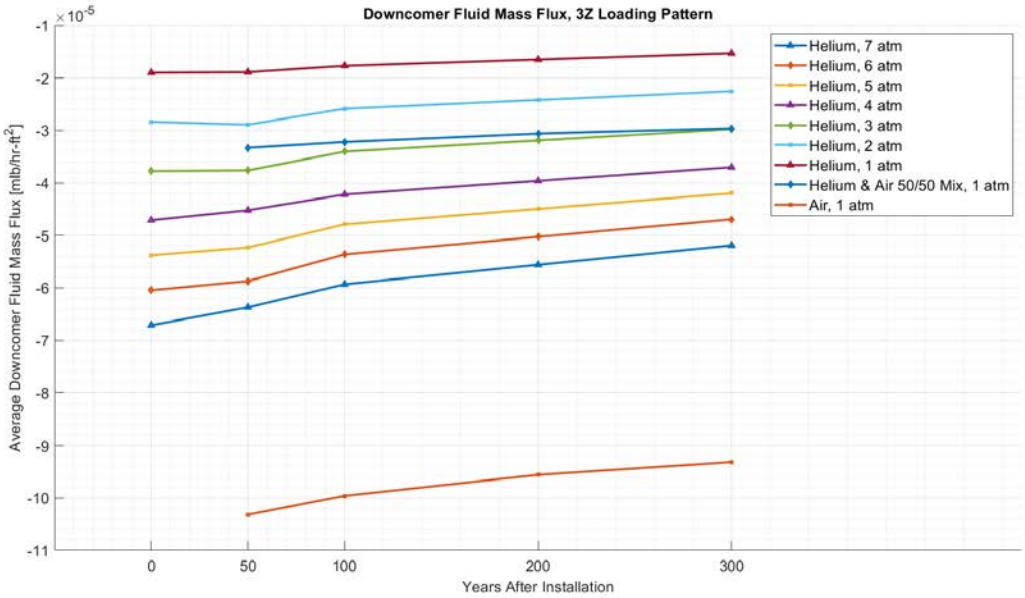


**Figure 5-44. Downcomer Fluid Mass Flux, 3Z Loading Pattern**

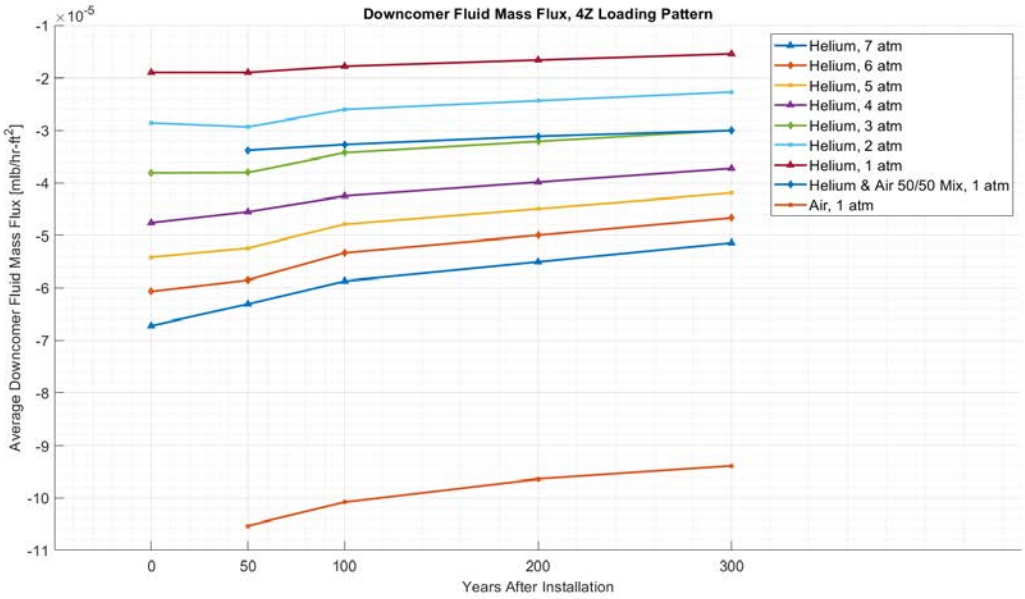


**Figure 5-45. Downcomer Fluid Mass Flux, 4Z Loading Pattern**

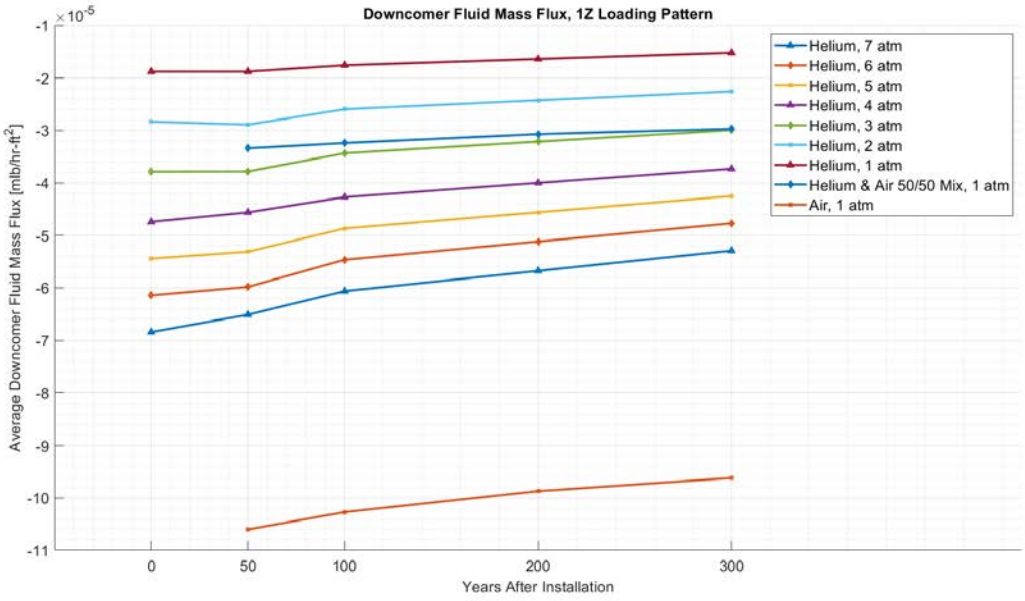


**Figure 5-46. Downcomer Fluid Mass Flux, 1Z Loading Pattern**

This page is intentionally left blank.

# 6. STAR-CCM+ MODEL DESCRIPTION

The present model was updated using STAR-CCM+ 2021.1.1, for all steps except definition of model geometry, which was performed with SolidWorks (Dassault Systemes 2011). The model descriptions in this section are repeated here from the original study (Fort et al. 2016), except for changes related to the fill gas.

## 6.1 Model Geometry

The following sections describe the model geometry, which includes the 3-dimensional model and the mesh.

### 6.1.1 Geometry

A 3-dimensional model of the MAGNASTOR geometry was created in the solid modeling Computer Aided Design (CAD) software SolidWorks (Dassault 2011). The CAD geometry was generated from 2-dimensional drawings of the MAGNASTOR assembly provided by NAC. The CAD geometry is shown in Figure 6-1.

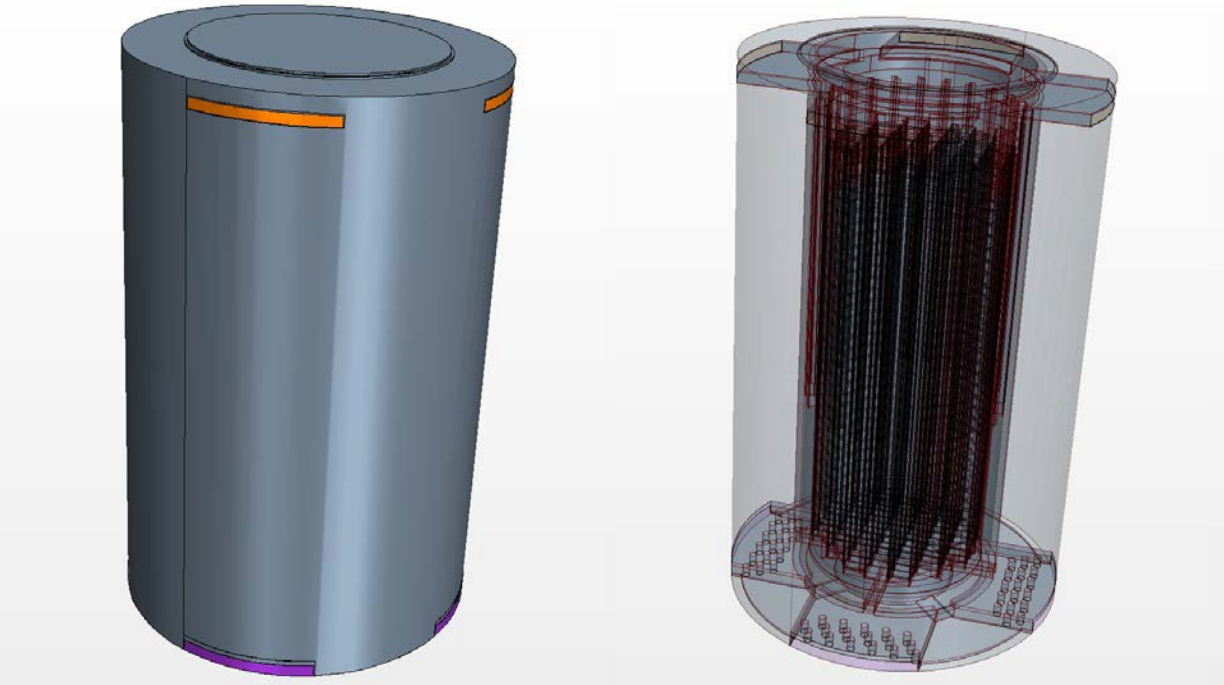

**Figure 6-1. CAD Model Geometry for MAGNASTOR Assembly**

### 6.1.2 Mesh

The SolidWorks geometry was imported into STAR-CCM+. The geometry was then meshed into 70 separate regions connected by 380 interface boundaries, resulting in a single conformal volume mesh across all regions. The polyhedral volume mesh contains 7,509,880 cells, 36,683,412 faces, and 29,673,739 vertices. Along each wall/fluid interface, the mesh contains a prism layer to improve the accuracy of the flow solution near the walls. The prism layer consists of orthogonal prismatic cells, four cells thick, adjacent to the wall boundaries. Figures 6-2 through 6-4 show the mesh assembly.

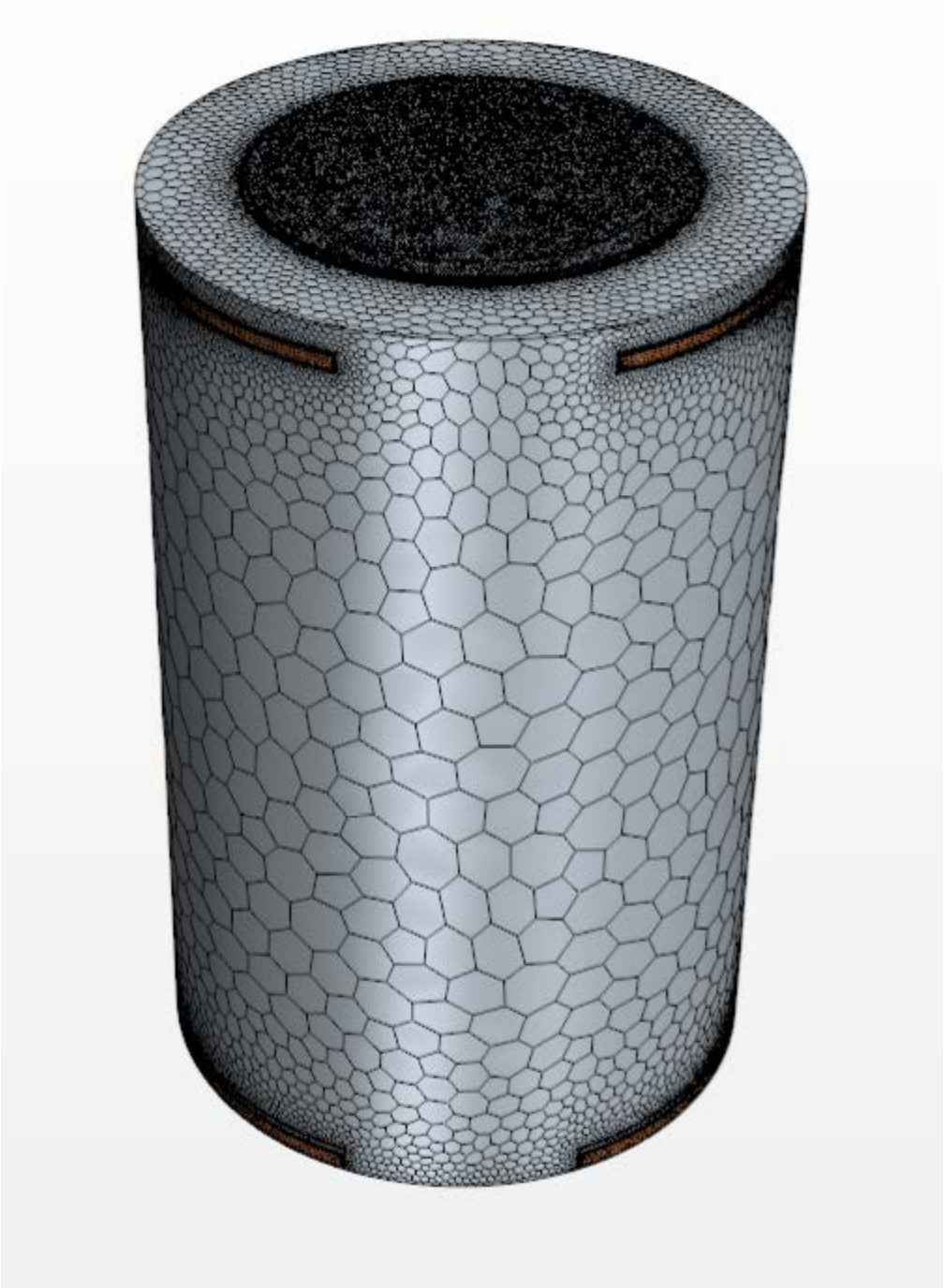

**Figure 6-2. MAGNASTOR Assembly Mesh**

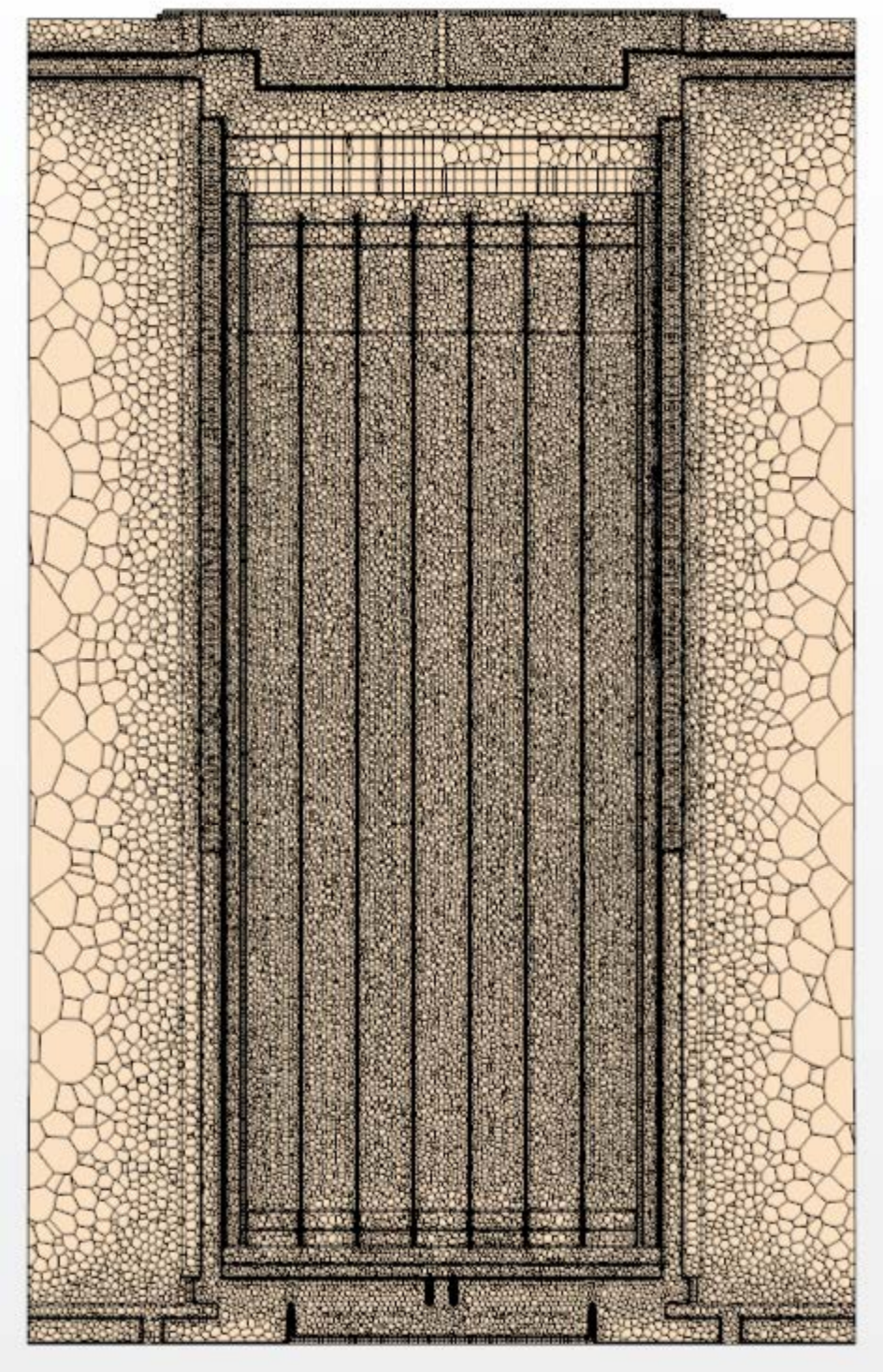

**Figure 6-3. MAGNASTOR Assembly Mesh – Axial Cross-sectional View**

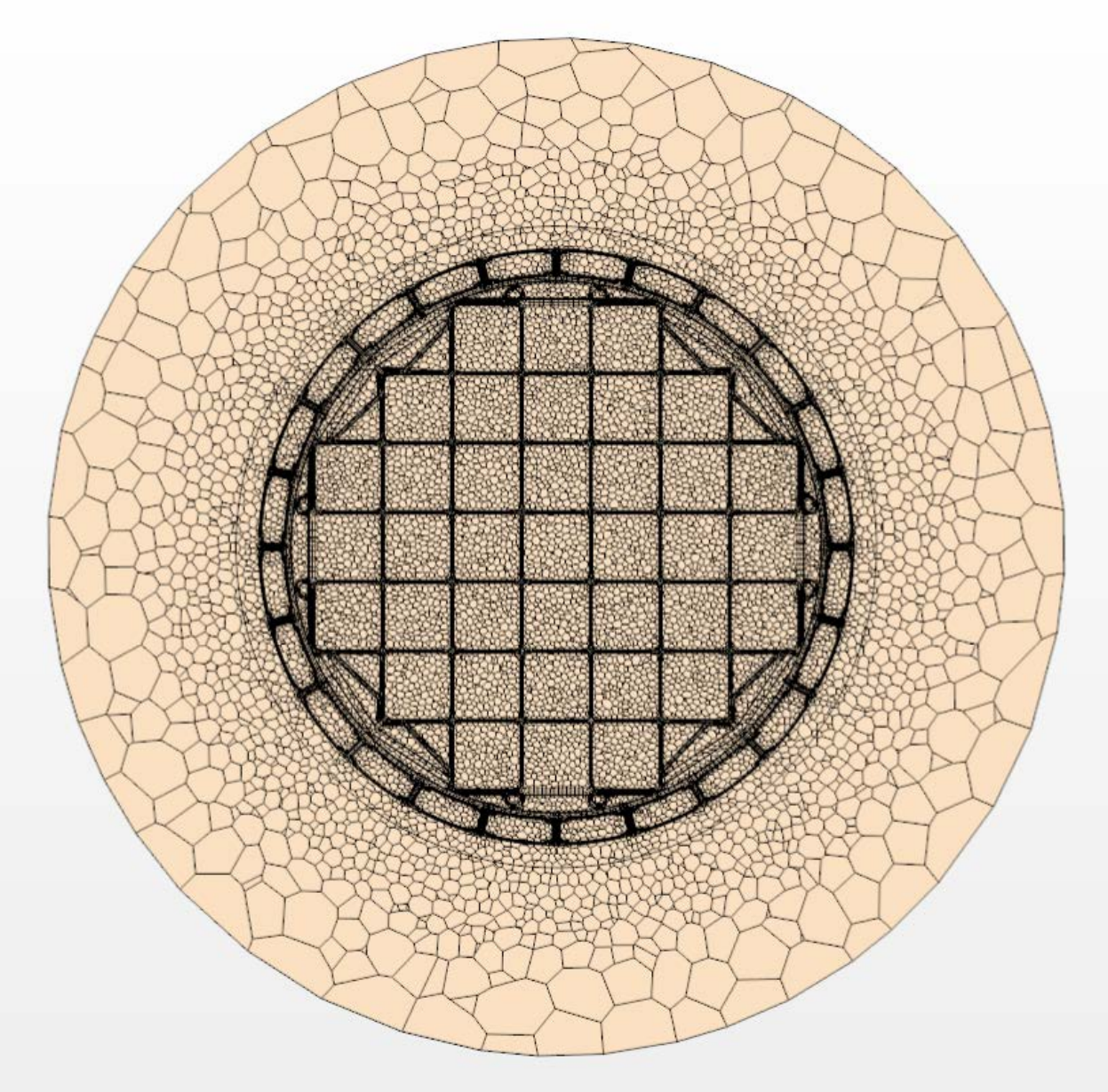

**Figure 6-4. MAGNASTOR Assembly Mesh – Radial Cross-sectional View**

## 6.2 Material Properties

Temperature-dependent properties were used in the STAR-CCM+ model for all solids and for the fill gases (air and helium). For thermal conductivity and dynamic viscosity of air, this was accomplished with appropriate inputs to Sutherland's law, an option available in the code. These same properties for helium and air-helium mixture were included in the STAR-CCM+ model as user-defined input tables (Incropera et al. 2007).

Since the fill gas in the TSC does not communicate with an external pressure boundary, the gases were assigned a constant density and buoyancy forces were computed using the Boussinesq approximation (see Cuta et al. 2013, Section 6.1.1). The fill gas density was set to the target bulk gas densities identified in Table 6-1. Since the airflow has pressures referenced to inlet and outlet boundaries, air density was computed using the ideal gas law.

**Table 6-1. Densities Assigned in the Filled Gas Region of the Model**

| Fill Gas | Density ($kg/m^3$) | Pressure (atm) |
|---|---|---|
| Helium | 0.763 | 7 |
| | 0.436 | 4 |
| | 0.109 | 1 |
| Air | 3.155 | 4 |
| | 0.789 | 1 |
| Mixture | 0.898 | 1 |

The helium within the TSC is modeled as a laminar flow. The cooling airflow was modeled as a turbulent flow using the built-in k-omega shear stress transport (SST) turbulence model (Siemens 2019).

## 6.3 Approximation of Fuel Region

Following general practice for CFD models of baskets and fuel assemblies, the rod bundles are modeled as a homogenized medium, with average properties designed to simulate heat transfer from the fuel and to give a representative and conservative representation of peak fuel temperatures. This strategy is well tested in horizontal storage systems where heat transfer by thermal conduction and radiation dominate and the contribution from convection in the fuel assemblies is small enough to be negligible. In such conditions, the radial heat transfer in the fuel is modeled as conduction-only with an effective thermal conductivity that includes effects of thermal radiation, following the methodology in Bahney and Lotz (1996).

The fuel assembly effective conductivity model had been developed previously and was based on geometry for WE 17x17 OFA in the Office of Civilian Radioactive Waste Management database (DOE 1987). The effective thermal conductivity model was calculated with an assembly power level of 1.02 kW. Note that the FSAR (NAC 2011) uses 14x14 fuel for design basis thermal analyses, since that fuel configuration has the minimum effective conductivity of all PWR fuel types that can be stored in this system.

The appropriate radial fuel effective conductivity for a given application depends on the fuel assembly geometry, the assembly decay heat, and the geometry of the basket cell in which the fuel assembly resides. The surface emissivity of the fuel rod cladding and the basket cell walls also need to be considered in developing an appropriate effective conductivity model for a particular application. For the assumption used in this case, the radial effective conductivity was determined to be,

$$k_{eff_{radial}} = 0.1147 \exp(0.0034\, T)$$

where

$k_{eff}$ = effective thermal conductivity (W/m-K), and

$T$ = local temperature (K).

For the axial effective conductivity of the assembly, the approach in safety-basis calculations is to neglect thermal radiation in the axial direction and convection. Effective conductivity in the axial direction for the homogeneous block representing the fuel assembly is defined simply as the area-weighted average of the conductivity of zircaloy cladding and helium backfill gas. Conductivity through the fuel pellets is conservatively neglected. A previously developed correlation for this fuel geometry was used in this model.

$$k_{eff_{axial}} = 0.9738 \exp(0.0008\, T)$$

## 6.4 Gap Resistances

The STAR-CCM+ model gap resistances were based on the thermal conductivity and assumed gap thickness between the solid surfaces in the model. An example is shown in the following equation (Incropera et al. 2007):

$$R = \frac{L}{k}$$

where

$R$ = contact resistance ($m^2$-K/W),

$L$ = gap width (m), and

$k$ = thermal conductivity of the fluid (W/m-K).

Gap resistances were imposed in same locations as described for the COBRA-SFS model in Section 4, except between the assumed layers in the neutron absorber and where a gap was modeled explicitly, as was the case with the gap between the corner basket supports and the inner wall of the TSC. Gap resistances imposed in the STAR-CCM+ model are listed in Table 6-2.

**Table 6-2. Gap Resistances Incorporated in the STAR-CCM+ Model**

| Location | Equivalent Gap Thickness (in.) | Gap Material |
|---|---|---|
| Between fuel tubes | 0.01 | He |
| Between layers of neutron absorber | 0.01 | He |
| Between side support and TSC inner wall | 0.1 | He |
| Between support standoffs and TSC outer wall | 0.1 | Air |

## 6.5 Thermal Radiation

Surface-to-surface thermal radiation within the fuel basket region and thermal radiation from the external surfaces of the cask to the environment are included in the heat transfer evaluations using the STAR-CCM+ model. The surface emissivities used for thermal radiation exchange were set to values shown in Table 6-3. The emissivity used in the STAR-CCM+ model for carbon steel is representative, but differs from the value used in the COBRA-SFS model (see Table 4-2).

**Table 6-3. Emissivity Values for Radiation Heat Transfer**

| Material | Emissivity |
|---|---|
| Carbon Steel | 0.65 |
| Concrete | 0.8 |
| Stainless Steel | 0.46 |

View factors are computed between patches composed of adjoining cell surfaces. The target ratio of patch count to cell face count was 10%. The thermal radiation model was deactivated in the porous model regions of the fuel assembly because the effective thermal conductivity model in use there already includes radiation.

## 6.6 Boundary Conditions

This section describes the various external boundary conditions, including convection on external surfaces, solar loading, and conduction to the ground.

### 6.6.1 Convection on External Surfaces

Correlations for natural convection between vertical and horizontal surfaces with air at one atmosphere were used to calculate the convection heat transfer between the environment and external surfaces. Table 6-4 shows the correlations used (from Heat Transfer by J.P. Holman 1996).

**Table 6-4. Natural Convection Correlations**

| Surface | Laminar | Turbulent |
|---|---|---|
| | 10^4<GrPr<10^9 | GrPr>10^9 |
| Vertical plane or cylinder | h=1.42(ΔT/L)^(1⁄4) | *h*=1.31(Δ*TT*)^(1⁄3) |
| Horizontal plate facing upward | h=1.32(ΔT/L)^(1⁄4) | *h*=1.52(Δ*TT*)^(1⁄3) |

### 6.6.2 Solar Loading

The values used for solar loading are the same regulatory values used in the COBRA-SFS model (as shown in Table 4-2). These are 24-hour average values and they were applied without any reduction for solar absorptivity.

### 6.6.3 Conduction to Ground

A conduction boundary was applied to the bottom of the storage system model to represent heat transfer to the concrete ISFSI pad. A thermal resistance equivalent to a 3-ft. thick concrete pad was assumed with a 70°F (21.1°C) temperature at its base.

This page is intentionally left blank.

# 7. STAR-CCM+ MODEL RESULTS

This section describes the STAR-CCM+ modeling results. Section 7.1 details the models included in the analysis. Sections 7.2 and 7.3 show the findings from the models. These consist of comparisons of peak temperatures as well as a qualitative examination of internal fluid conditions.

## 7.1 Simulation Matrix

STAR-CCM+ was used for a limited number of simulations, primarily as a verification of the COBRA-SFS model results and for a detailed view of the fluid flow field in the module. Table 7-1 shows the models created for this analysis. Each "X" signifies a model was run at those conditions.

**Table 7-1. STAR-CCM+ Simulation Matrix**

| Loading Configuration: | | | 3Z | | |
|---|---|---|---|---|---|
| Pressure | He | Air | 0 yrs | 50 yrs | 100 yrs |
| 7 atm | 100% | 0% | X | X | X |
| 1 atm | 100% | 0% | | | X |
| 1 atm | 50% | 50% | | X | X |
| 1 atm | 0% | 100% | | X | X |
| Loading Configuration: | | | 4Z | | |
| Pressure | He | Air | 0 yrs | 50 yrs | 100 yrs |
| 7 atm | 100% | 0% | X | X | X |
| 1 atm | 100% | 0% | | | X |
| 1 atm | 50% | 50% | | X | X |
| 1 atm | 0% | 100% | | X | X |
| Loading Configuration: | | | 1Z | | |
| Pressure | He | Air | 0 yrs | 50 yrs | 100 yrs |
| 7 atm | 100% | 0% | X | X | X |
| 1 atm | 100% | 0% | | | X |
| 1 atm | 50% | 50% | | X | X |
| 1 atm | 0% | 100% | | X | X |

## 7.2 Temperature Comparison

The PCTs for each assembly in each STAR-CCM+ simulation are given in this section in Figures 7-1 through 7-3. The PCT of each comparable COBRA-SFS model is also included. Figure 7-4 compares all of the PCT findings from both modeling methods. The dotted line represents zero difference between the models. The further the data point lies from the dotted line, the more the PCT findings diverge.

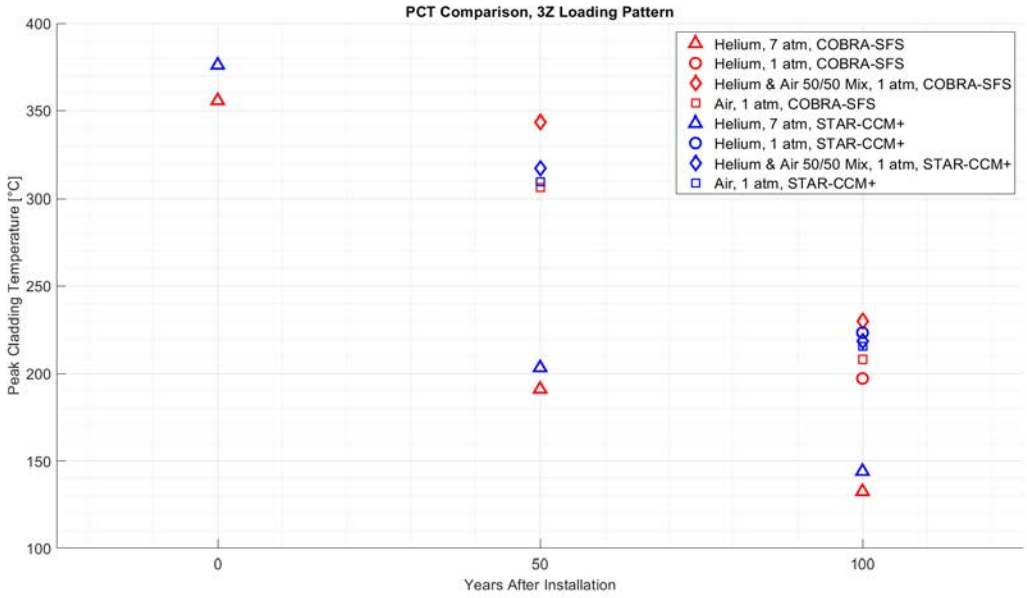


**Figure 7-1. Peak Cladding Temperatures, STAR-CCM+ & COBRA-SFS Models, 3Z Loading Pattern**

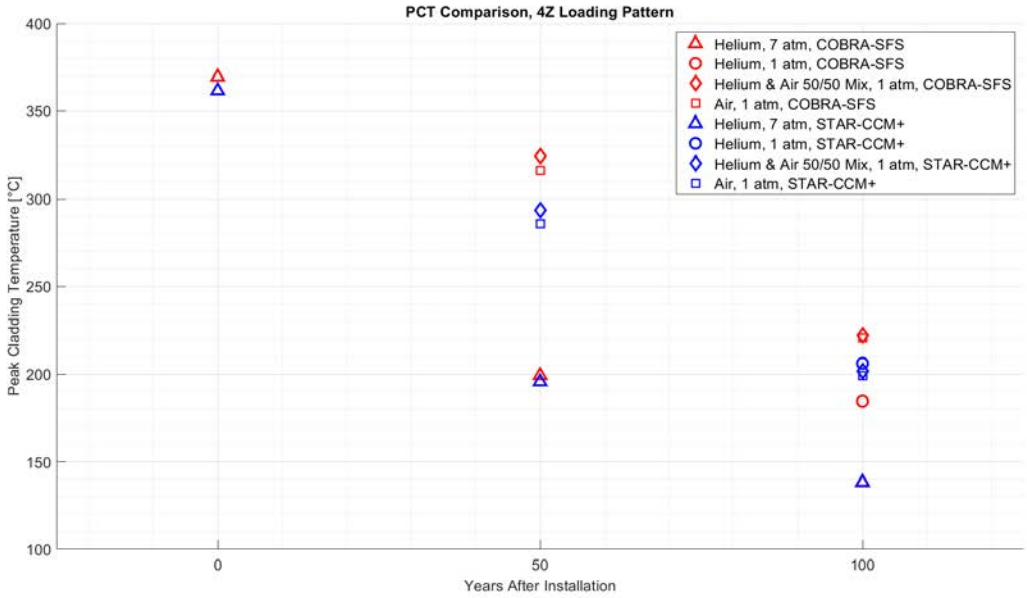


**Figure 7-2. Peak Cladding Temperatures, STAR-CCM+ & COBRA-SFS Models, 4Z Loading Pattern**

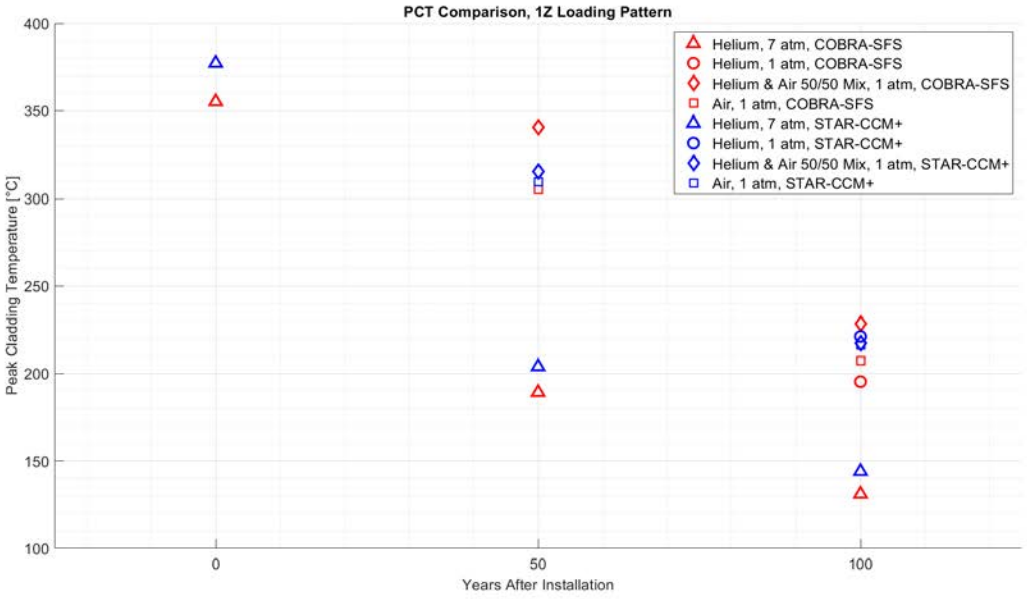


**Figure 7-3. Peak Cladding Temperatures, STAR-CCM+ & COBRA-SFS Models, 1Z Loading Pattern**

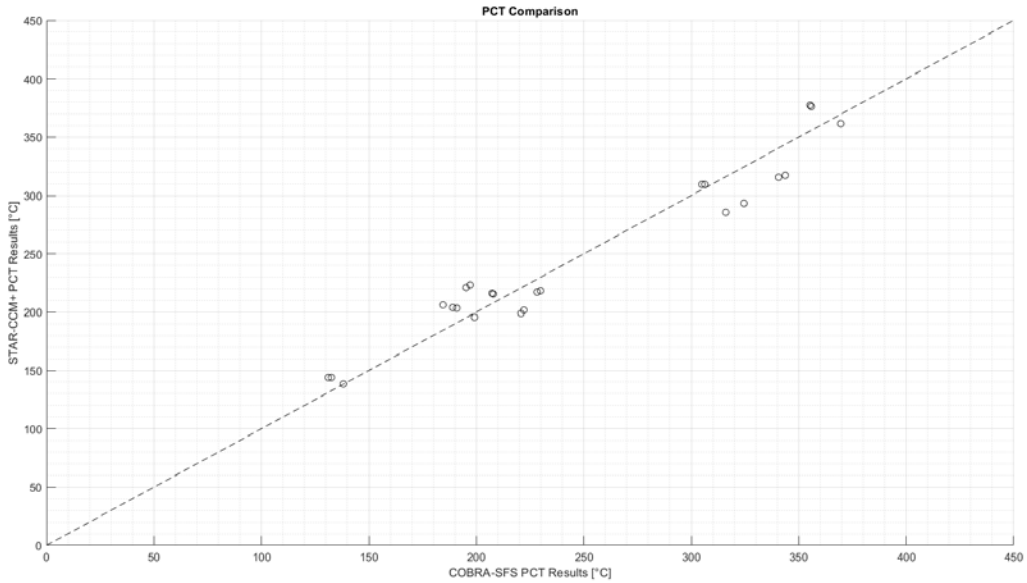


**Figure 7-4. Peak Cladding Temperature Comparison, STAR-CCM+ & COBRA-SFS Models, All Loading Patterns**

Figures 7-5 through 7-12 are temperature distribution maps for the canister surface for the 3Z loading pattern cases.

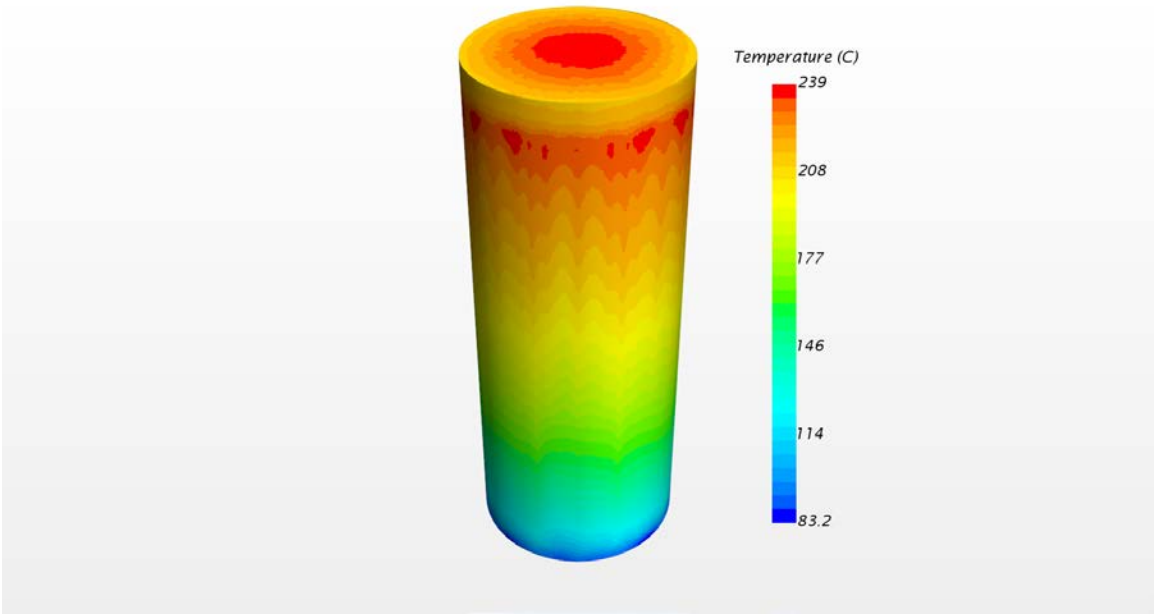


**Figure 7-5. Canister Temperature Distribution, 0 Years, 7 Atm He Fill Gas, 3Z Loading Pattern**

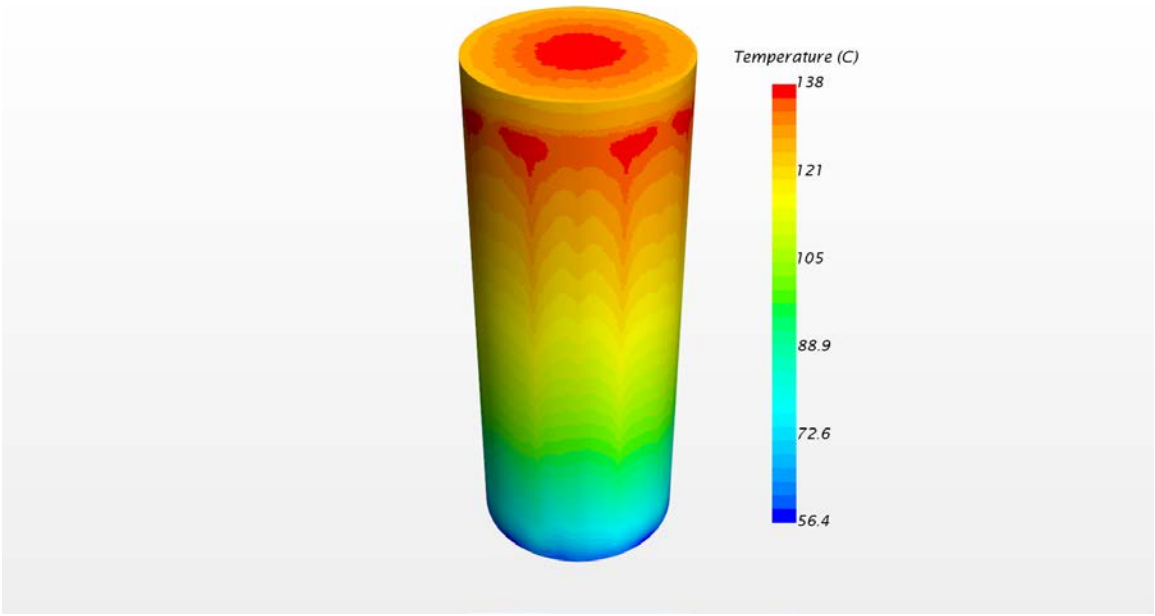


**Figure 7-6. Canister Temperature Distribution, 50 Years, 7 Atm He Fill Gas, 3Z Loading Pattern**

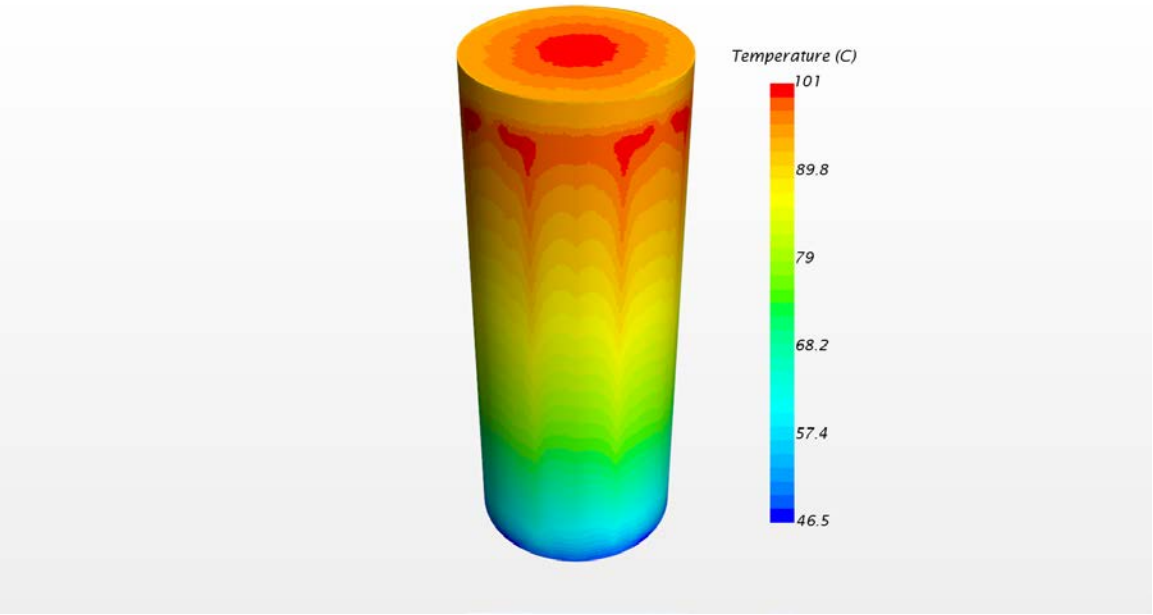


**Figure 7-7. Canister Temperature Distribution, 100 Years, 7 Atm He Fill Gas, 3Z Loading Pattern**

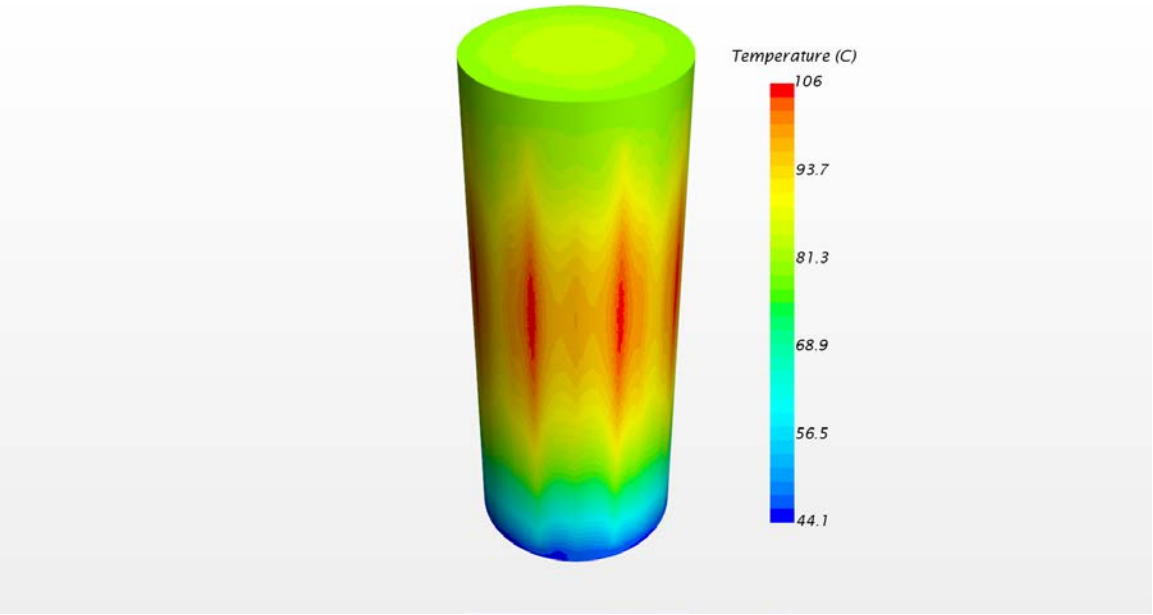


**Figure 7-8. Canister Temperature Distribution, 100 Years, 1 Atm He Fill Gas, 3Z Loading Pattern**

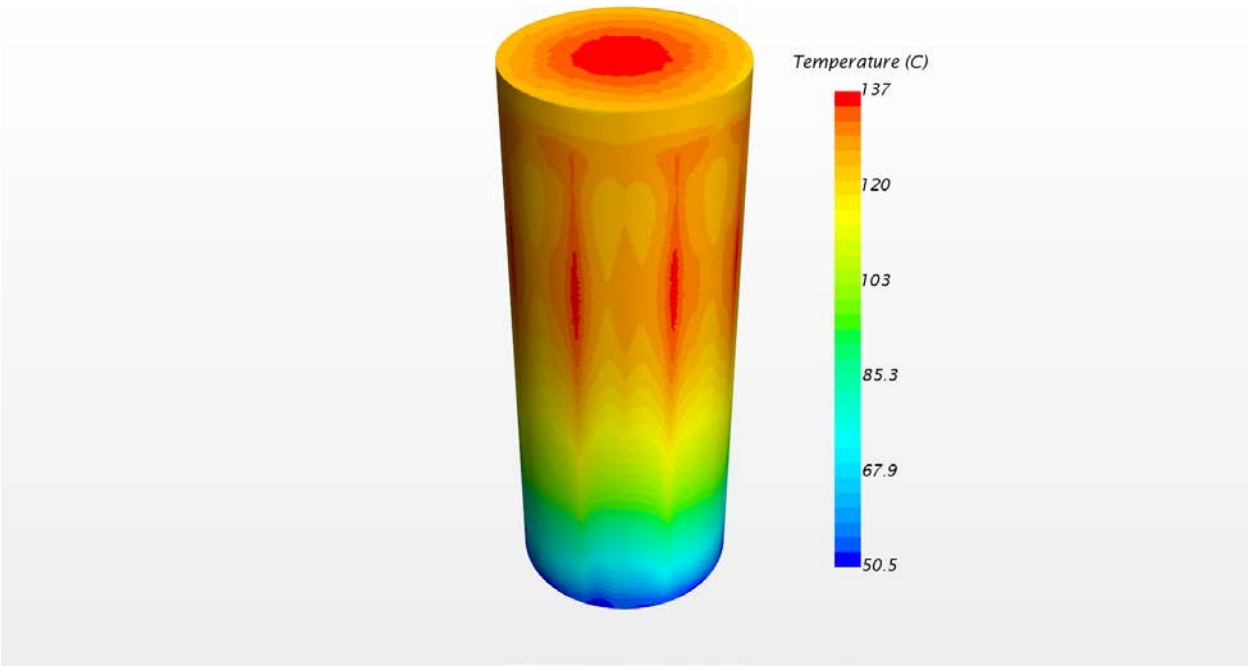


**Figure 7-9. Canister Temperature Distribution, 50 Years, 1 Atm He-Air Mix Fill Gas, 3Z Loading Pattern**

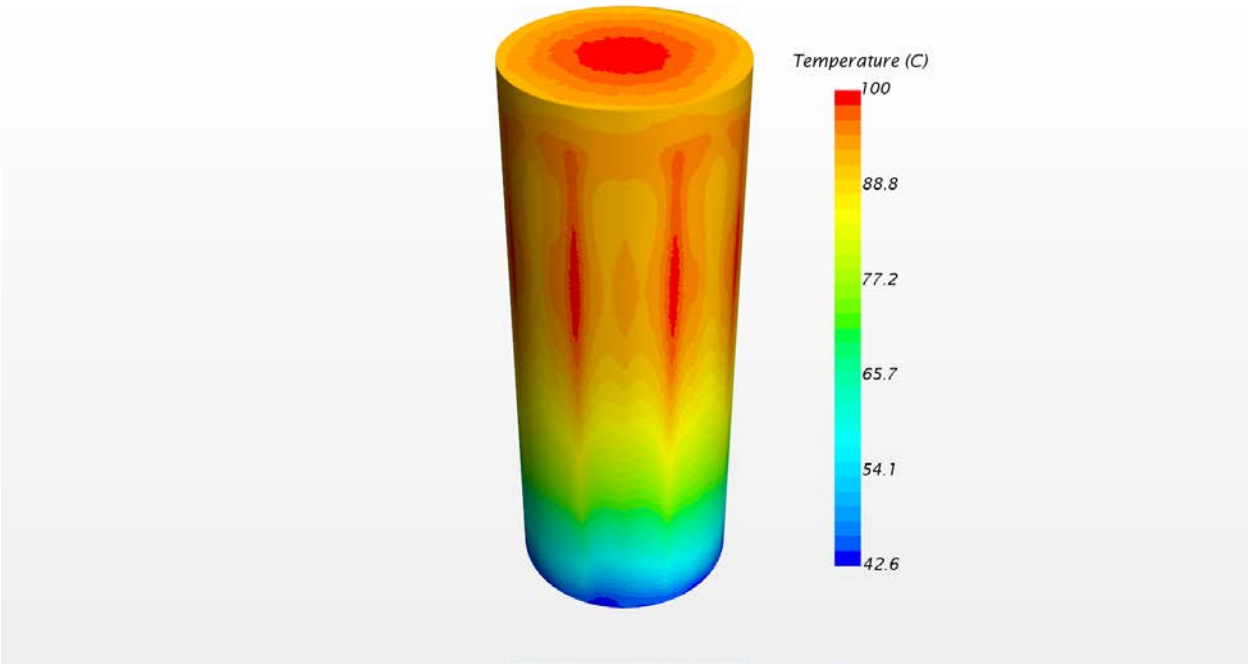


**Figure 7-10. Canister Temperature Distribution, 100 Years, 1 Atm He-Air Mix Fill Gas, 3Z Loading Pattern**

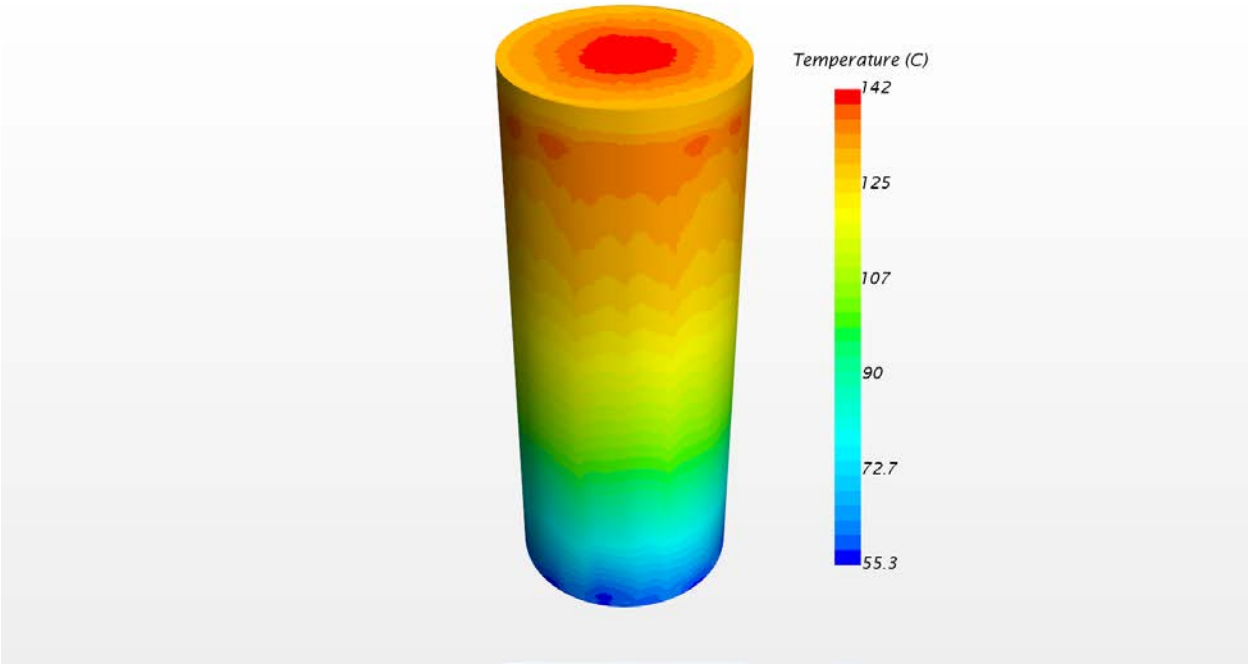


**Figure 7-11. Canister Temperature Distribution, 50 Years, 1 Atm Air Fill Gas, 3Z Loading Pattern**

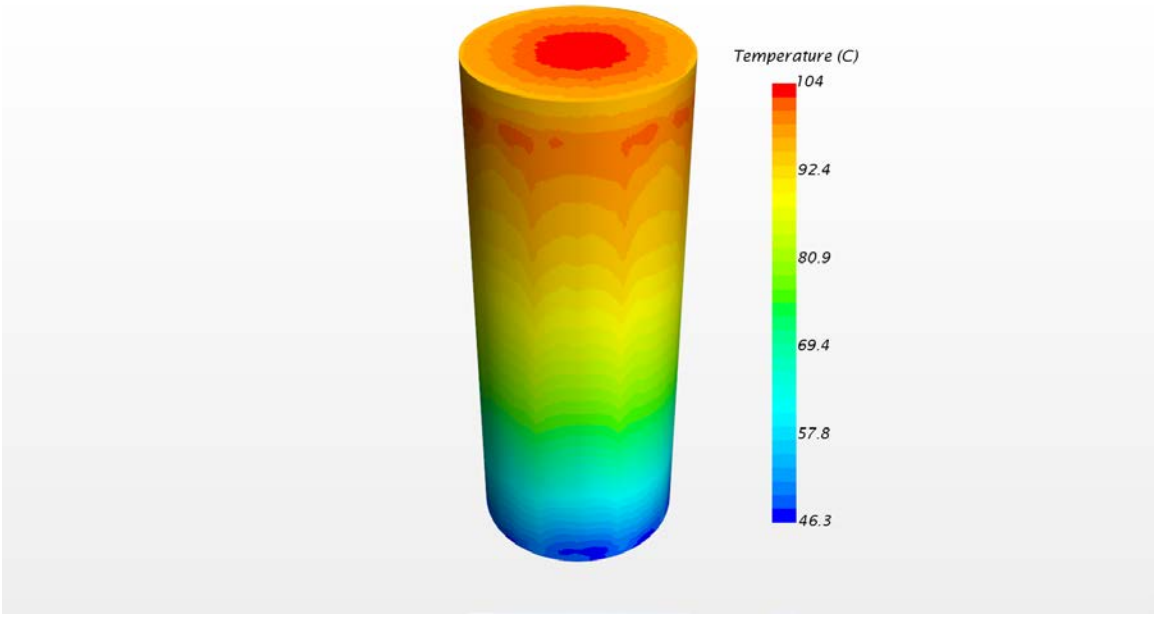


**Figure 7-12. Canister Temperature Distribution, 100 Years, 1 Atm Air Fill Gas, 3Z Loading Pattern**

## 7.3 Fluid Velocity Comparison

The following are velocity maps of 3Z loading cases. Figures 7-13 through 7-16 show the velocities in a horizontal slice in the MAGNASTOR system. The slice is positioned at the axial midpoint of the canister. The point velocities in the assemblies are not considered to be representative because the fuel rod structures were not explicitly modeled. For a given assembly, the average velocities will be comparable. The scaling of the figures is different for each case.

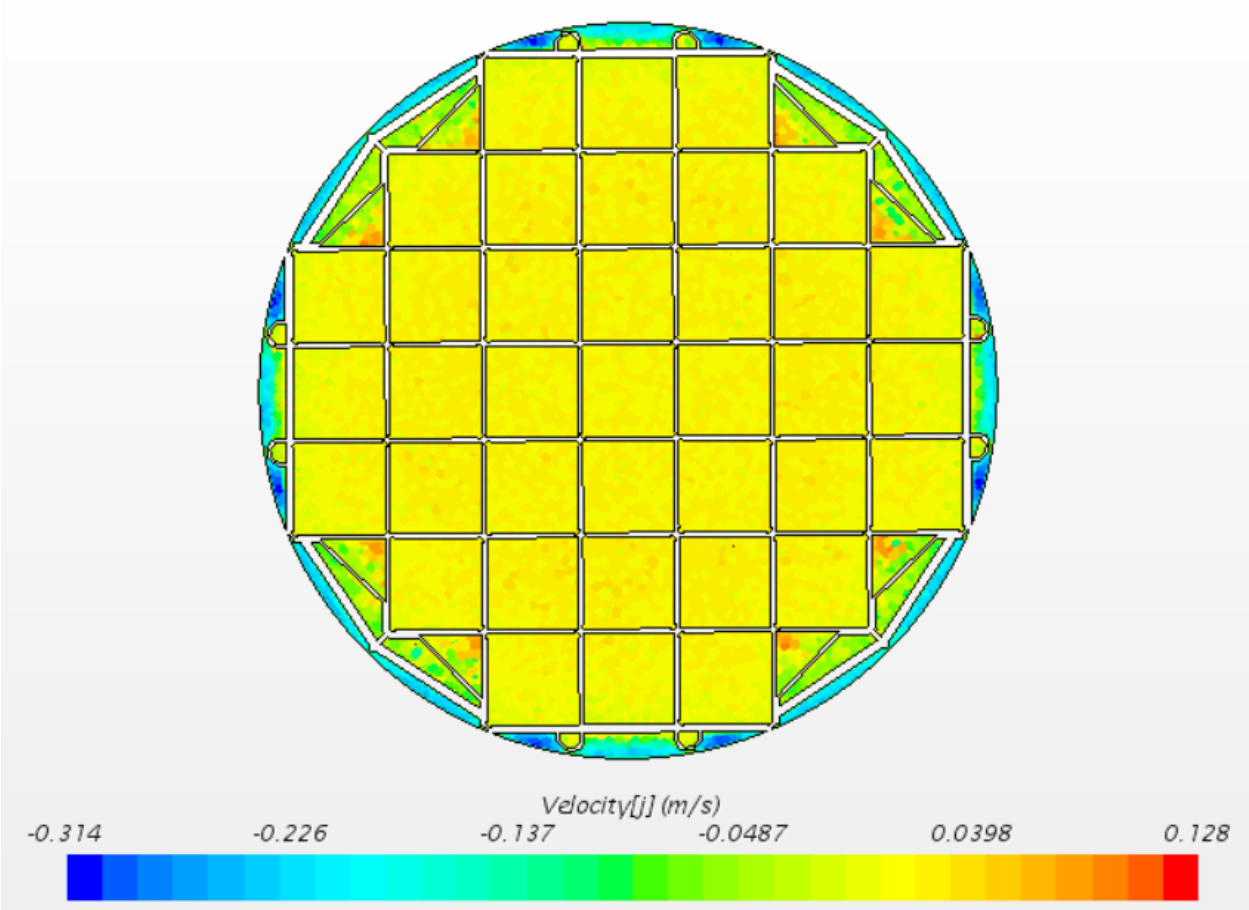


**Figure 7-13. Radial Velocity, 0 Years, 7 Atm He Fill Gas, 3Z Loading Pattern**

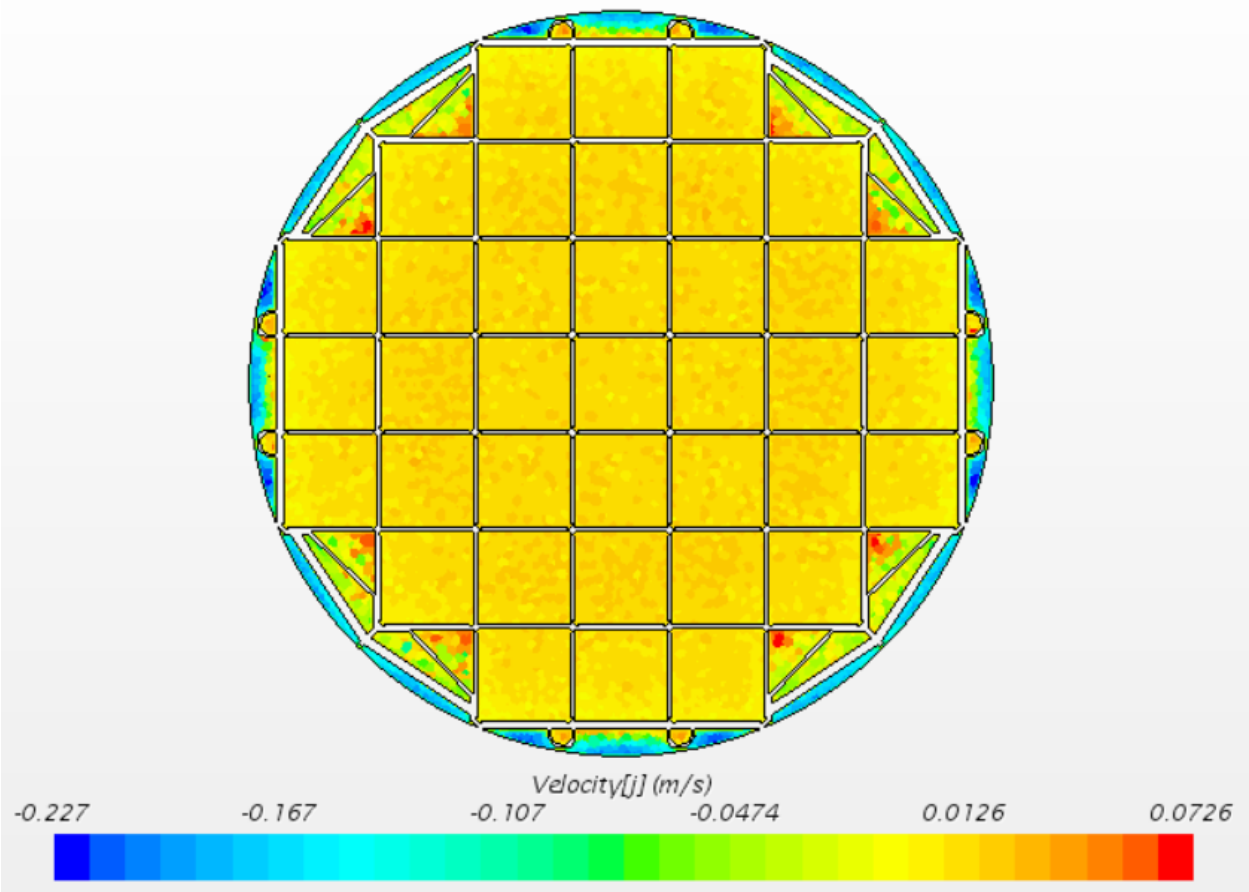


**Figure 7-14. Radial Velocity, 100 Years, 7 Atm He Fill Gas, 3Z Loading Pattern**

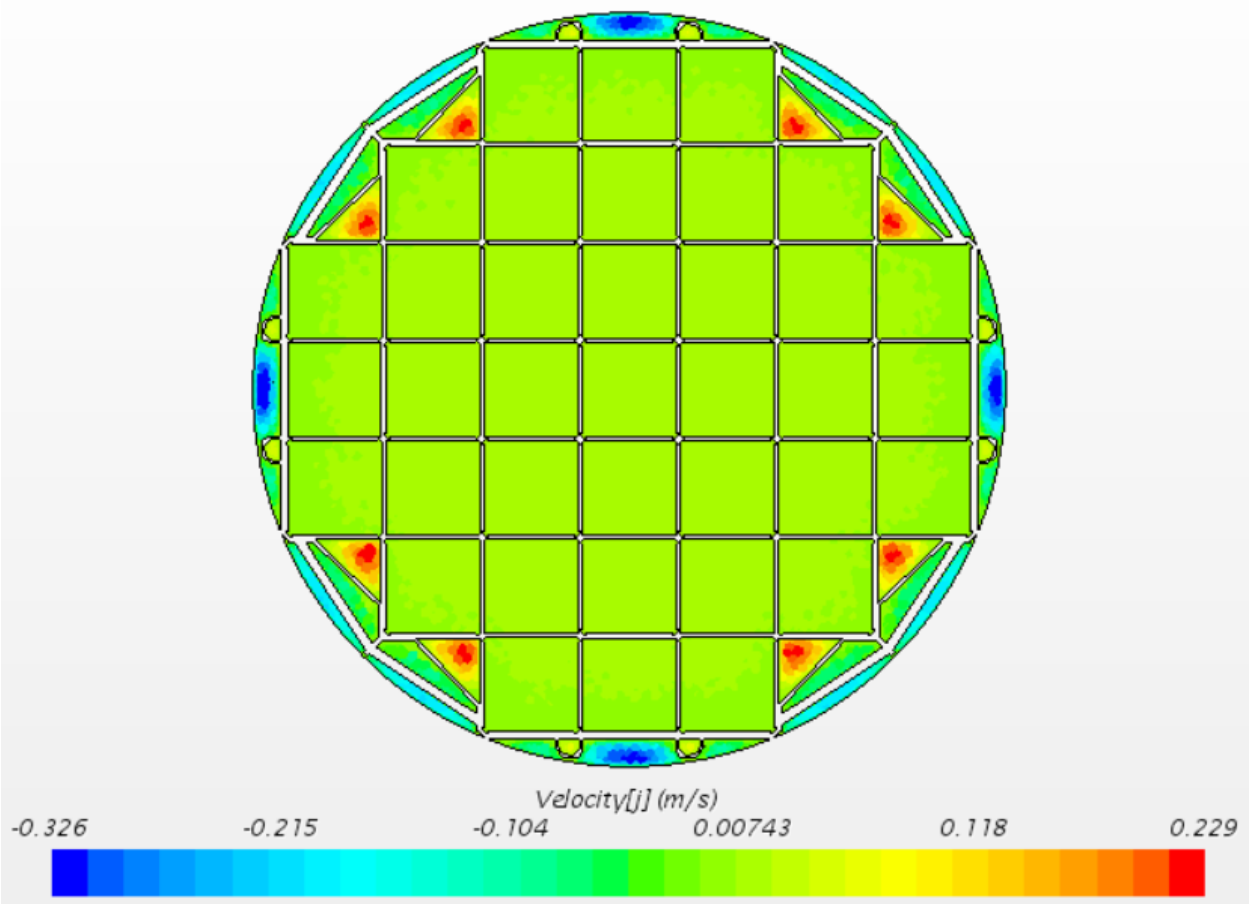


**Figure 7-15. Radial Velocity, 100 Years, 1 Atm He Fill Gas, 3Z Loading Pattern**

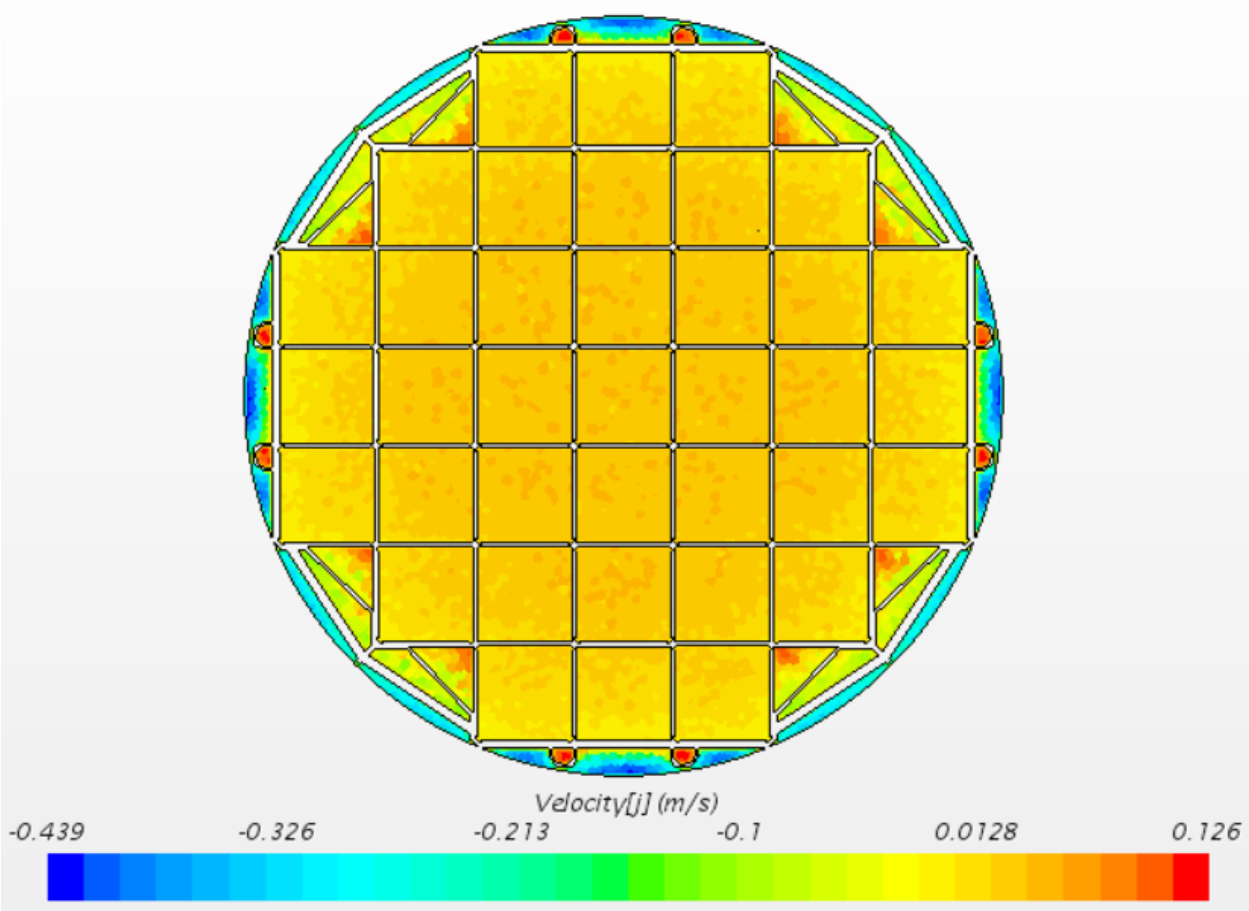


**Figure 7-16. Radial Velocity, 100 Years, 1 Atm Air Fill Gas, 3Z Loading Pattern**

Figures 7-17 to 7-20 show the velocity maps of the MAGNASTOR system in 3Z loading configuration using a vertical slice. Only the upper section of the gas environment is shown. The velocities in the assemblies are not considered to be representative because the fuel rod structures were not explicitly modeled. The scaling of the figures is different for each case.

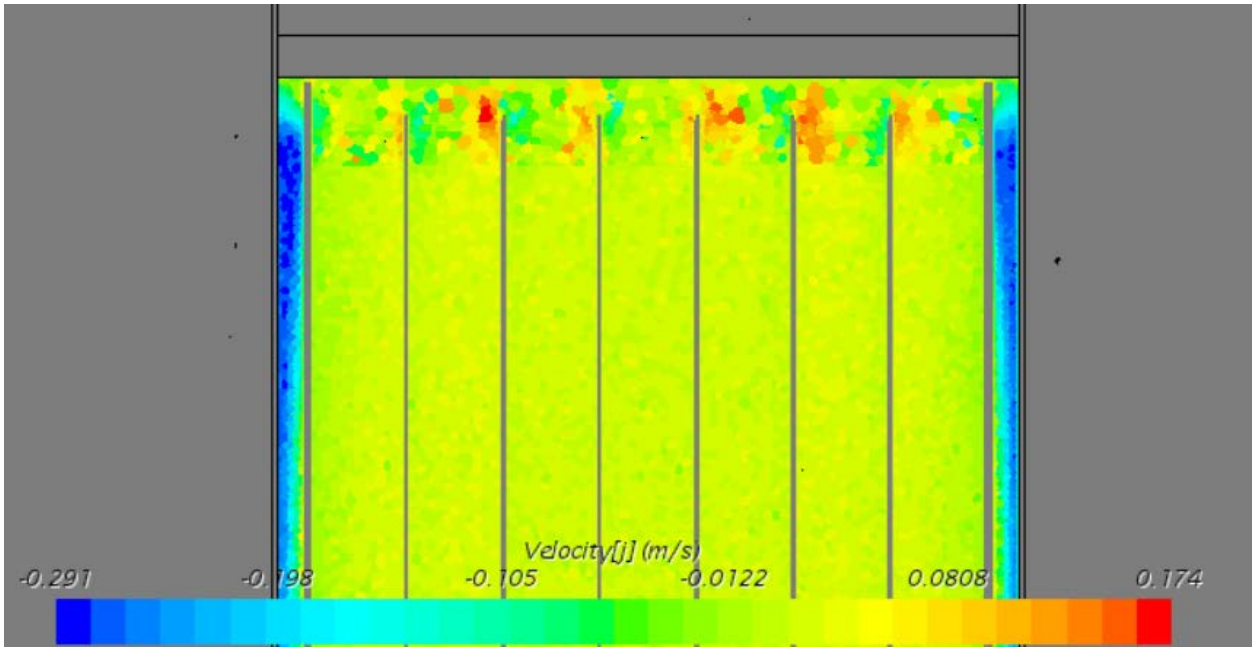


**Figure 7-17. Axial Velocity, 0 Years, 7 Atm He Fill Gas, 3Z Loading Pattern**

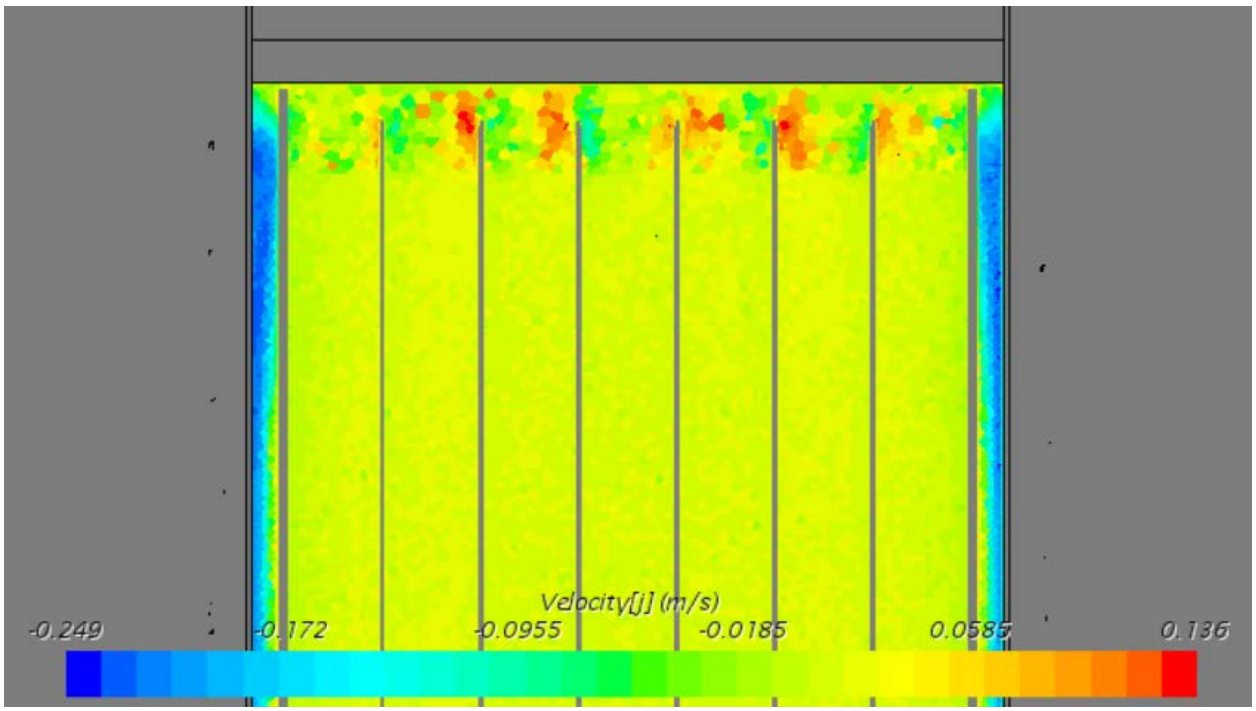


**Figure 7-18. Axial Velocity, 100 Years, 7 Atm He Fill Gas, 3Z Loading Pattern**

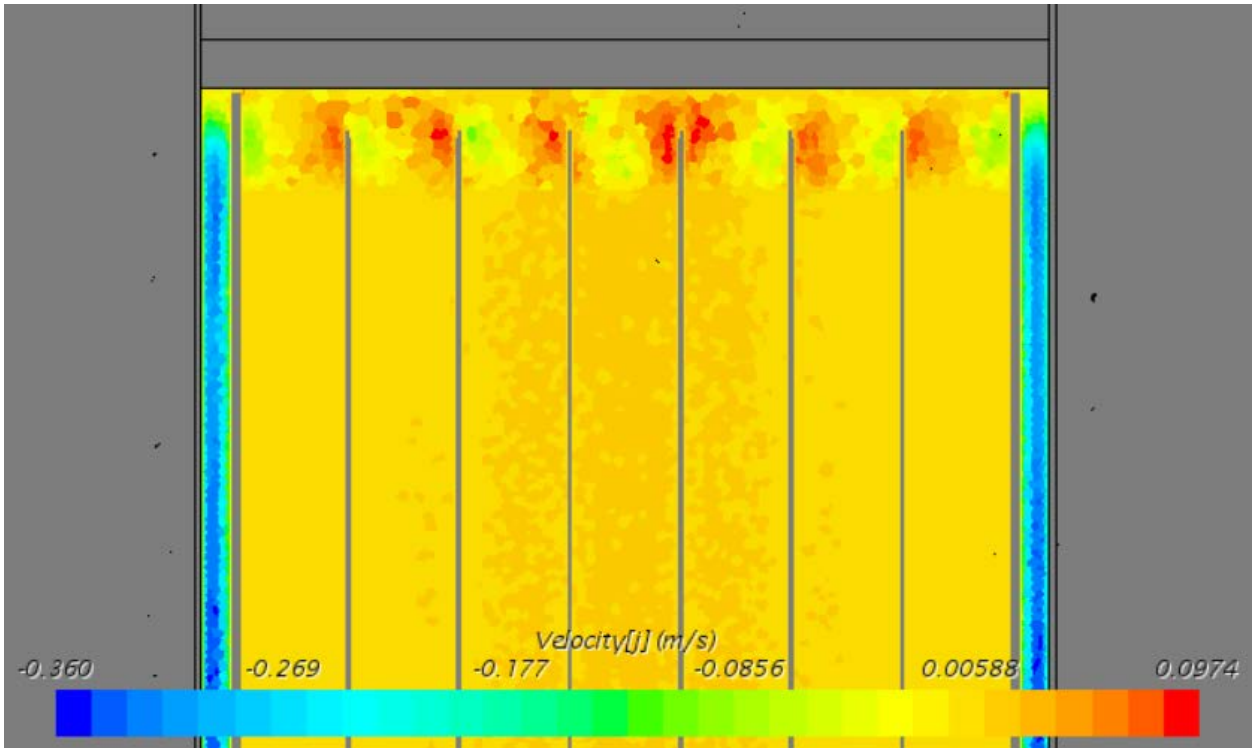


**Figure 7-19. Axial Velocity, 100 Years, 1 Atm He Fill Gas, 3Z Loading Pattern**

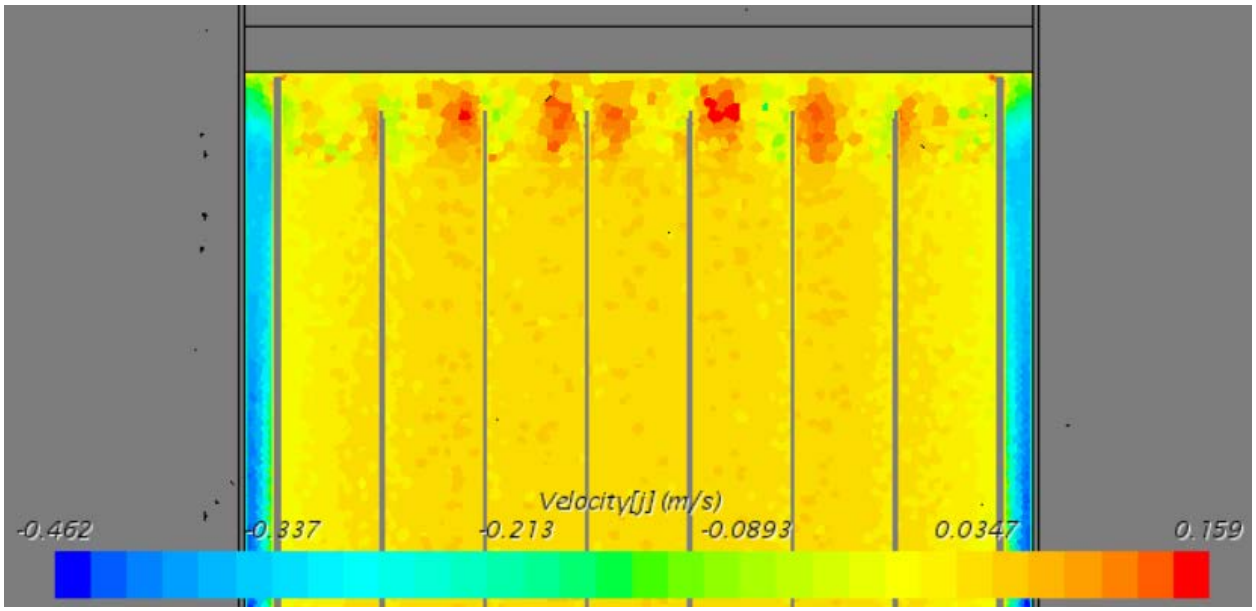


**Figure 7-20. Axial Velocity, 100 Years, 1 Atm Air Fill Gas, 3Z Loading Pattern**

This page is intentionally left blank.

# 8. DISCUSSION

This section discusses a selection of the important results and specifically their relevance to the initial questions of this report:

1. What are the thermal impacts in areas of interest?
2. Can we determine fill pressure loss through external (relative to canister) temperature behavior?
3. What are the impacts on flow velocities (inside and outside the canister)?

## 8.1 Peak Cladding Temperature

Both the STAR-CCM+ and COBRA-SFS results showed good agreement with each other in the helium environment cases. COBRA-SFS generally modeled temperatures that were colder than the STAR-CCM+ results. This is likely due to differences in approximation of the fuel region, gap resistances and gas composition. Previous work modeling the MAGNASTOR with a K-effective model and STAR-CCM+ has shown the STAR model to be 5°C – 11°C higher in PCT than the COBRA-SFS model. All the results presented in this paper are consistent with that finding. STAR-CCM+ models relied on a calculated gas density to estimate the fill gas. This method has been tested and validated for helium environments but has not been used to simulate mixed and air environments before.

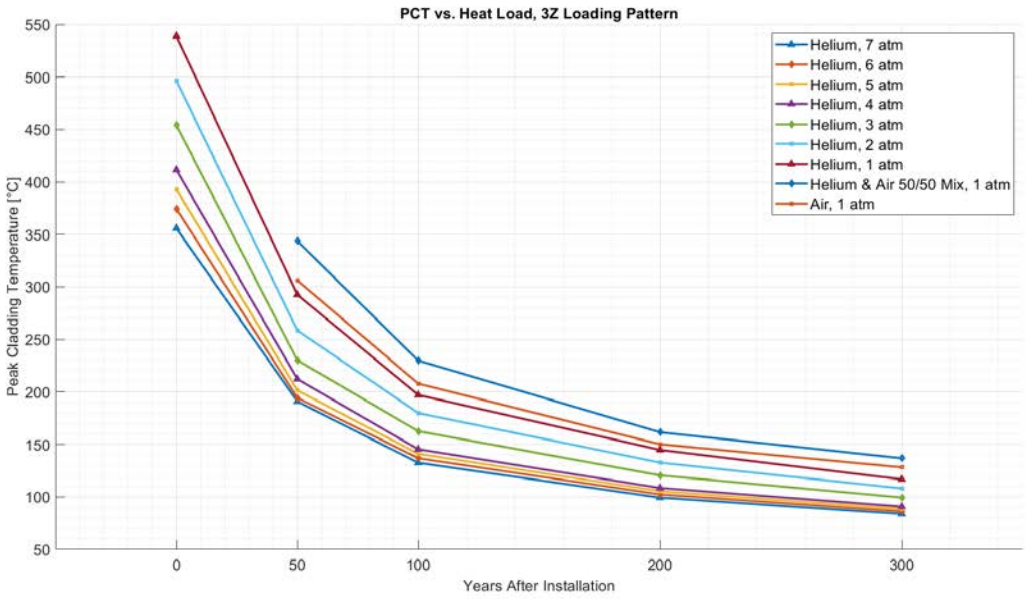


**Figure 8-1. Peak Cladding Temperatures, 3Z Loading Pattern**

The PCT results (Figure 8-1) overall are largely as expected for a system like the MAGNASTOR that relies on thermosiphoning for cooling. Put simply: when helium pressure decreases, PCT increases. The more interesting results are seen when the 1 atm helium results are compared to the 1 atm 50/50 mixed He-air results. Using the 3-zone loading pattern as an example, the air PCT is approximately 20°C lower than the 50/50 PCT after 100 years. Section 8.2 shows in more detail the canister internal cooling flows, which when considering mass flux are increased when the atmosphere is 1 atm air compared to 1 atm helium or 50/50 helium. This directly impacts the convection cooling and at the relatively low heat loads

result in lower cladding temperatures. At higher heat loads this effect may not hold due to the changing balance between radiation, conduction, and convection heat transfer.

## 8.2 Fluid Flow

The annulus gas velocities were completely dependent on heat load, which is as expected. The air flow is induced through the change in density within the annulus. That change can only be affected by heat load, not internal conditions.

From the COBRA-SFS results, the average velocity of the gas in the downcomers changes gradually with changing internal environment gas, with more significant changes occurring with the introduction of air. For all loading patterns, the highest velocities were found in the mixed gas cases, with the low-pressure pure helium and pure air cases being similar. The STAR-CCM+ results show similar average velocities in the downcomers but afford much higher resolution flow dynamics. The regions of highest flow change significantly based on the internal gas environment. As shown in the horizontal slices, the area of highest velocity in the downcomers is more centrally located for low-pressure environments. The vertical slices show that the velocities vary axially as well. The high heat load case shows a much stronger velocity gradient, with higher velocities towards the lid than the base. The lower heat load cases and low-pressure cases show a much more even distribution in axial velocity in the downcomers.

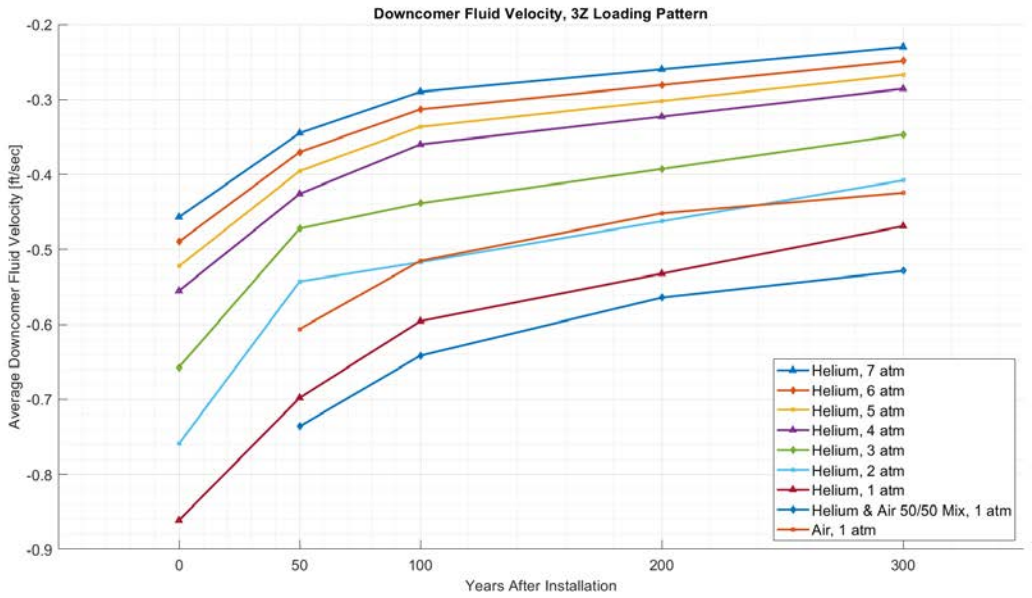


**Figure 8-2. Downcomer Fluid Velocity, 3Z Loading Pattern**

Figures 8-2 and 8-3 show the fluid velocities and mass flow rates respectively. From these plots it becomes clear why counterintuitive temperature results appear, as discussed in Section 8.1. Mass flow rate of the air cases are very high compared to the 1 atm helium. Clearly at these temperature differentials and mass flow rates this is enough to overcome the reduced thermal conductivity of the air. Overall mass flow is a better indication of convective cooling than velocity and the increased mass flow indicates that air can carry more energy out of the canister. The increased mass flow can be attributed to the difference in density between helium and air. As shown in Figure 8-4, the density of nitrogen at 1 atm is much higher and exhibits greater changes per degree of temperature difference than helium at 1 atm.

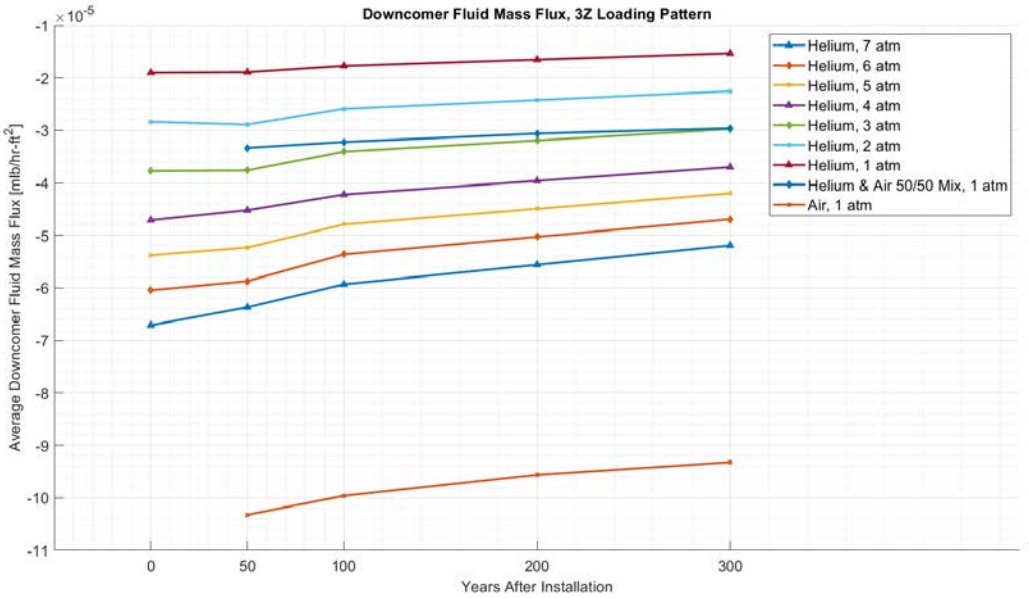


**Figure 8-3. Downcomer Fluid Mass Flux, 3Z Loading Pattern**

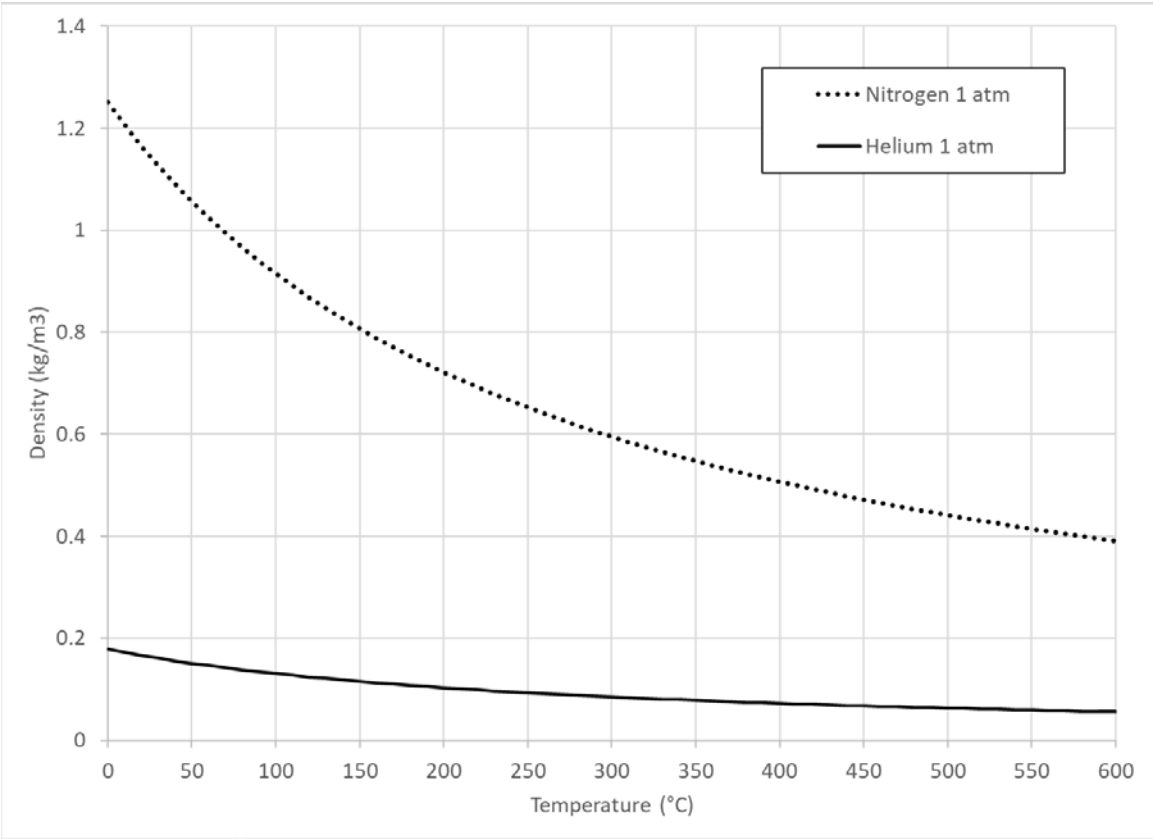


**Figure 8-4. Comparison of Densities between Helium and Nitrogen at 1 atm**

## 8.3 Canister Surface Temperatures

The results from the STAR-CCM+ simulations show significant variation of the canister, lid, and base temperatures at a resolution that were not possible to obtain from the COBRA-SFS simulations. While the overall averages are consistent, the temperature distributions seen in the STAR-CCM+ results could be important factors depending on application. For instance, if one were interested in using lid or base temperatures to diagnose the presence of a depressurizing leak, the placement of a sensor could have a significant effect on the sensor's usability. Even accounting purely for average temperature as plotted in Figures 8-5 and 8-6 there is a noticeable increase in lid and base plate temperatures for air cases compared to helium cases. This change is generally 10°C–25°C and is detectable by most sensor implementations. One aspect that is not addressed in this report is the transient response of the canister. There may be some "noise" related to ambient temperature changes and more study would be needed to determine the magnitude of this and whether or not a detection system could be set up to appropriately warn of loss of helium. Between 1 atm and 7 atm, lid and base temperatures are relatively constant after 100 years.

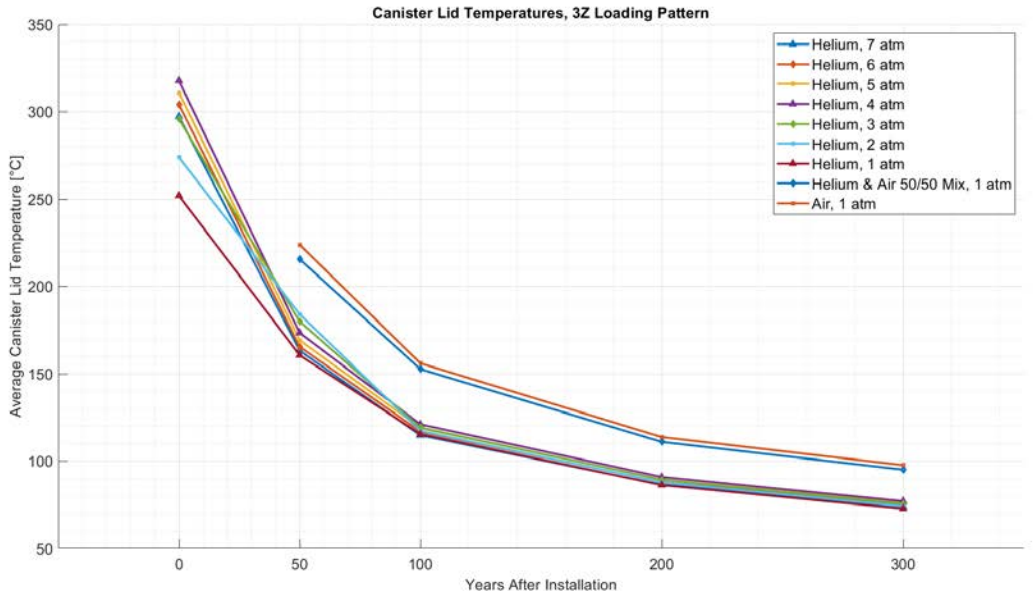


**Figure 8-5. Canister Lid Temperatures, 3Z Loading Pattern**

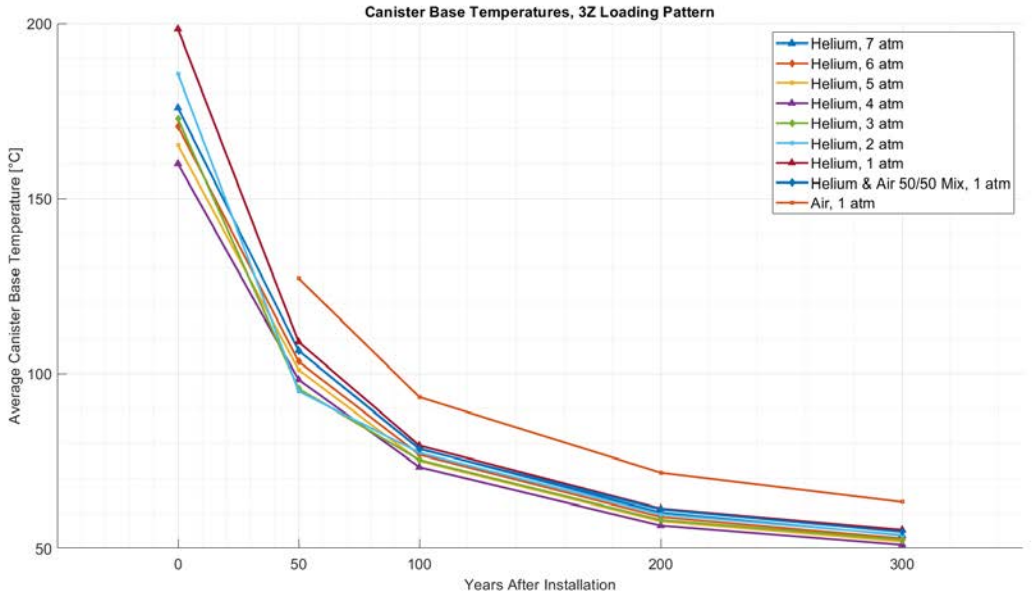


**Figure 8-6. Canister Base Temperatures, 3Z Loading Pattern**

The potential also exists for employing temperature sensors that measure the lid and base temperatures at the same time. Figure 8-7 shows the differences between the average lid and base temperatures for all cases modeled using the 3Z loading pattern. At high heat loads, it may be easy to differentiate between a fully pressurized system and a system that is losing pressure. The temperature difference is almost 40°C greater at 4 atm than at 7 atm for the design basis (year 0) case. The disparity in temperature difference between 4 atm and 1 atm helium at the design basis case is approximately 105°C. As the heat load falls over time, the helium fill cases tend to differ less. At year 300, all helium fill cases fit into a 10°C envelope. An important finding, however, is that even at year 300, there is a significant change between any full helium fill case and the mixed gas fill case and the air fill case. The difference between the greatest helium fill case and the mixed gas fill case at year 300 exceeds 10°C.

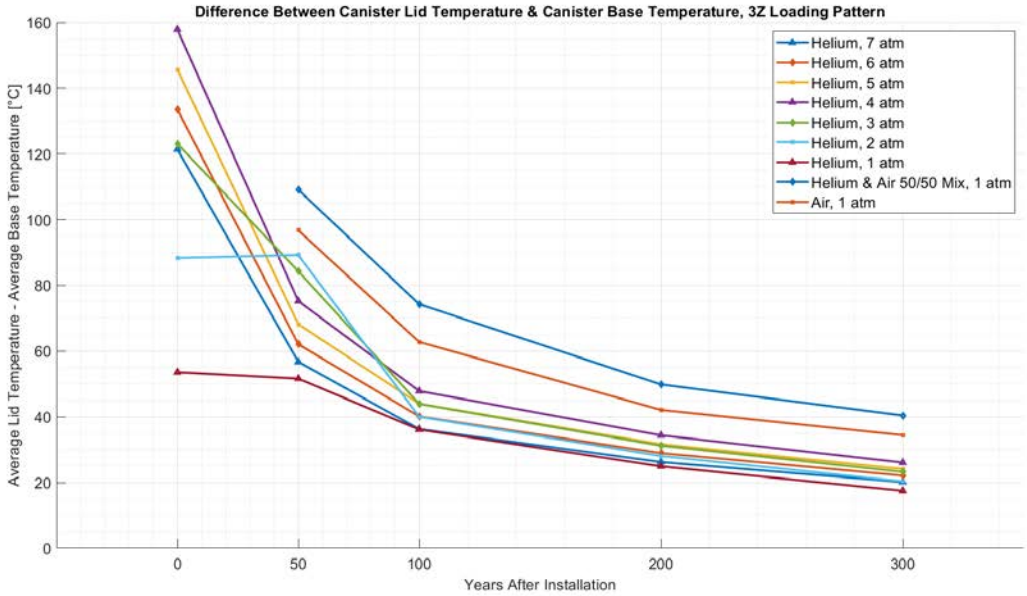


**Figure 8-7. Lid – Base Temperature Differences, 3Z Loading Pattern**

Another important result shown in the COBRA-SFS results is in Figure 8-8. This shows the consistent average canister temperature regardless of gas environment. The other plots in this section denote the variation in temperature profile. In contrast, the average temperature is a surrogate for heat flux out the side boundary. The consistent temperature is indicative that the same amount of heat is exiting the canister radially in all cases with the same heat load.

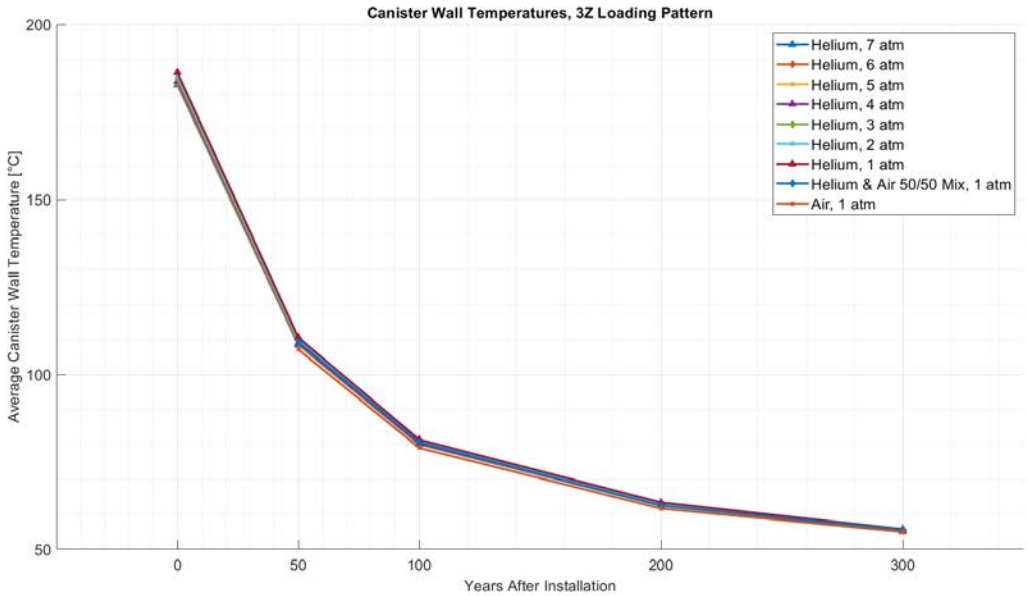


**Figure 8-8. Average Canister Wall Temperatures, 3Z Loading Pattern**

Figures 8-9 and 8-10 show STAR-CCM+ plots for the canister surface at 100 years and 1 atm helium and air respectively. Figure 8-11 shows the temperature distribution on the canister surface at 0 years and 7 atm helium, for comparison. As discussed in Section 8.2, the helium and air velocities and mass flow

rates are very different. In this case the temperature distribution (not magnitude) of the air case closely matches the temperature distribution of the 7 atm helium cases early in life. This could impact both canister integrity and leak detection. If a breach were to occur later in life, the heated areas of the canister would be very different than with a fully pressurized helium canister. Additionally, this shows the type of temperature profile variation that is experienced between helium and air environments, even at the same pressure. There is a substantial difference with the helium profile at 1 atm showing peaks much higher of centerline than the 1 atm air case.

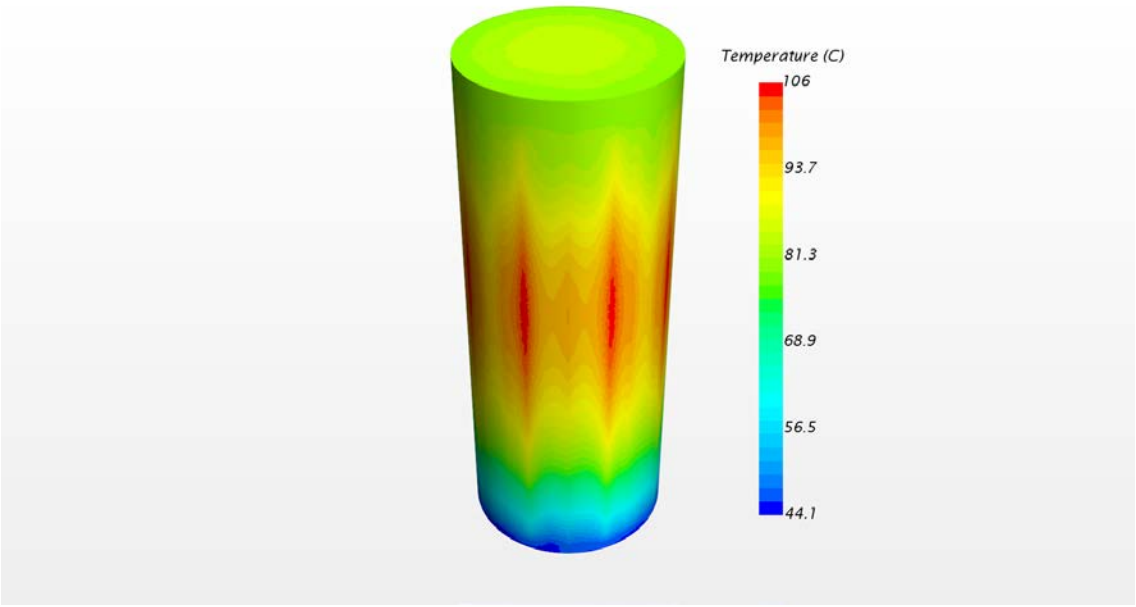


**Figure 8-9. STAR-CCM+ Temperature Plot for the Canister Surface at 100 Years and 1 Atm Helium**

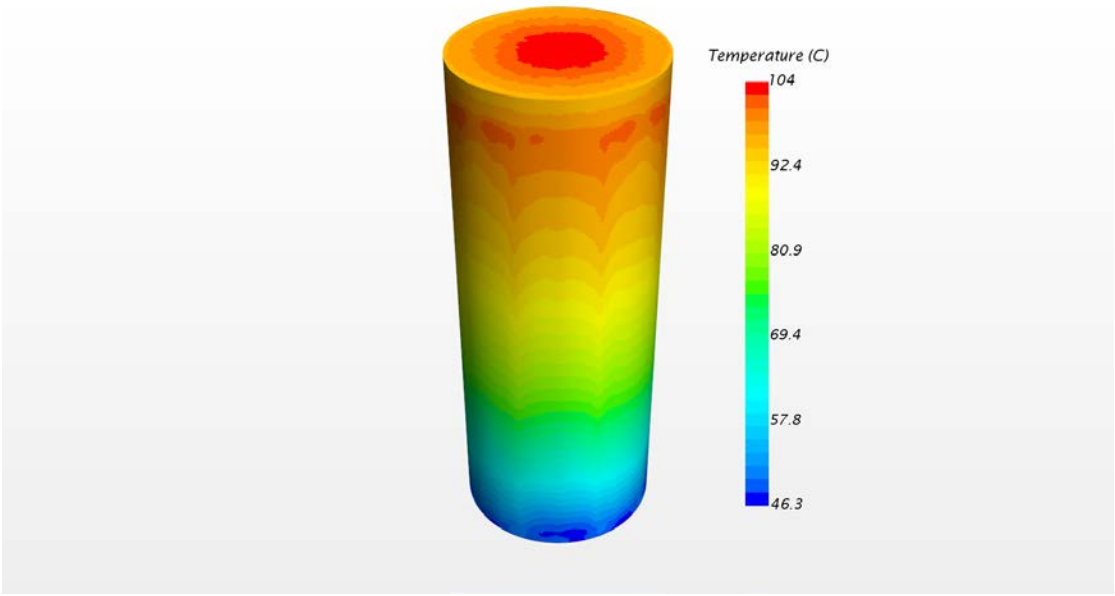


**Figure 8-10. STAR-CCM+ Temperature Plot for the Canister Surface at 100 Years and 1 Atm Air**

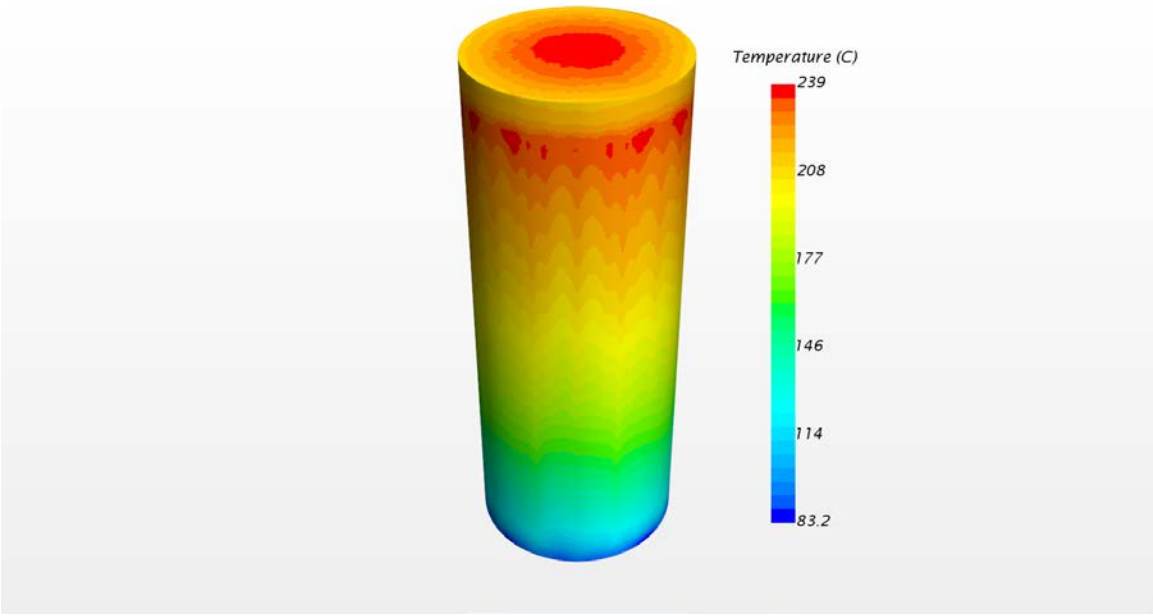


**Figure 8-11. STAR-CCM+ Temperature Plot for the Canister Surface at 0 Years and 7 Atm Helium**

# 9. CONCLUSIONS

The results in this work show the ability of both STAR-CCM+ and COBRA-SFS to model different atmospheric conditions in a spent fuel storage system. By modeling the MAGNASTOR cask with two separate codes and showing agreement in results, there is high confidence in their validity. Using COBRA-SFS provided an ability to collect a very large dataset with practical time constraints and computing hardware for this application. Conclusions are drawn below in the three major areas of study for this report.

## 9.1 Thermal Impacts

For each of the loading patterns studied there was no significant change in overall behavior later in life. This is useful for future modeling work since it can narrow down the relevant cases to study. There was also no challenge to the thermal performance limits of the cask and fuel with loss of helium pressure and introduction of air into the canister. This is needed to bound the consequence of a loss of fill gas. There will be no direct impact on safety significant thermal performance metrics. The primary impacts will be to secondary features such as the canister temperature distribution and gas velocities. At the heat loads studied the model results showed a decreasing difference between cladding temperatures as helium temperatures increased, suggesting there is a diminishing return to higher pressurization in this class of storage system.

## 9.2 Loss of Fill Gas Detection Ability

The results of this report show that detection of loss of fill gas is absolutely possible through studying canister temperatures. The temperature differences between helium and air environments are significant and would likely be detectable by correctly set up equipment. Using lid and base temperature differences as a detection method seems very feasible. However, it would not be without its challenges. Detecting decreased helium pressure later in life may be difficult due to the potential for “noise” in a real system. This would likely require using more sensitive sensors, with close attention paid to the contact between the sensor and the canister as well as any wind activity during measurement. As shown in the temperature distribution plots from the STAR-CCM+ models, the location of the sensor may also have a significant effect on determining a leak. At this point, it is difficult to develop best practices regarding placement, but this could be ameliorated with further study. Additional considerations would likely include the leak rate and any transient temperature effects, all of which were not able to be examined in this effort.

## 9.3 Flow Impact

The annulus flow showed no change with internal environment. However, significant changes in the internal canister gas flows were observed when the helium environment was replaced with air. Mass flux in the downcomers was affected by both pressure and proportion of air. As pressure decreased, the mass flux decreased proportionally. With the introduction of air, the increased velocity and gas density resulted in increasing the mass flux by a large margin. The magnitude of gas velocity in the downcomers was highest for low-pressure environments and increased as pressure was reduced. The gas velocity was not as sensitive to the introduction of air as the mass flow, with all 1 atm gas velocities almost equivalent. Overall, the results indicate that there will be no change in the external deposition rate of particles no matter the internal gas environment. However, if there is a breach later in life, internal gas velocities will increase from their helium low point. This is outside the scope of this analysis, but it raises the question of whether any hypothetical fuel particles will be resuspended.

This page is intentionally left blank.

# 10. FUTURE WORK

There are multiple possibilities for follow on modeling and experimental work from the results in this report. Although there was no direct thermal consequence of the loss of fill gas, there are areas of research and technology development that can be informed by further efforts in this area. Some possibilities are:

- Experimental validation of results with an apparatus such as the Dry Cask simulator would be useful to confirm the behavior shown in this report. However, some effects may not be as prominent without a larger multi-assembly experimental setup.
- This work led to the development of additional analysis tools that can be used in conjunction with COBRA-SFS to process data more quickly. The modeling effort could be repeated with another storage system for less expense.
- Much of the dataset generated could not be thoroughly processed due to time constraints. Detailed statistical analysis could yield greater understanding of which factors are most influential on thermal behavior. A predictive regression model could be developed without additional fluid thermal modeling.
- This report was limited to steady state modeling. Transient modeling of this system under environmental conditions would be an important step in the development of sensor technology. This is needed to define the “noise’ and understand the detection setpoints and signal processing needed to definitively determine if there is a loss of helium in the canister.
- Further study needs to be conducted into both the internal and external transport of particles in this type of system. Under an air environment there was significant difference in the internal flow velocities. Work outside the scope of this report is needed to determine if those velocity changes impact the transport of particles to a canister breach. External transport will not be affected by a hypothetical canister breach; however the transport conditions have not been evaluated in this work.

This page is intentionally left blank.

# 11. REFERENCES

Bahney III, RH and TL Lotz. 1996. *Spent Nuclear Fuel Effective Thermal Conductivity Report*. BBA000000-01717-5705-00010 Rev. 00, TRW Environmental Safety Systems, Inc., Fairfax, Virginia.

Chase, M.W., Jr. 1998. "NIST-JANAF Thermochemical Tables, Fourth Edition." *J. Phys. Chem. Ref. Data*, Monograph 9, 1-1951.

Cox, J.D.; Wagman, D.D.; Medvedev, V.A. 1984. *CODATA Key Values for Thermodynamics*. Hemisphere Publishing Corp., New York.

Cuta JM, SR Suffield, JA Fort, and HE Adkins. 2013. *Thermal Performance Sensitivity Studies in Support of Material Modeling for Extended Storage of Used Nuclear Fuel*. Fuel Cycle Research and Development, U.S. Department of Energy, Used Fuel Disposition Campaign. FCRD-UFD-2013-000257. PNNL-22646.

Dassault Systèmes. 2011. SolidWorks 2011. SolidWorks® Software. Dassault Systèmes - SolidWorks Corporation 300 Baker Avenue Concord, Massachusetts 01742 USA.

Fort, JA, TE Michener, SR Suffield, DJ Richmond. 2016. *Thermal Modeling of a Loaded MAGNASTOR Storage System at Catawba Nuclear Station*. PNNL-25871, Pacific Northwest National Laboratory, Richland, Washington.

Fort, JA, DJ Richmond, JM Cuta and SR Suffield. 2019. *Thermal Modeling of the TN-32B Cask for the High Burnup Spent Fuel Data Project*. PNNL-28915, Pacific Northwest National Laboratory, Richland, Washington.

Gauld IC, SM Bowman, and JE Horwedel. 2009. *ORIGEN-ARP: Automatic Rapid Processing for Spent Fuel Depletion, Decay, and Source Term Analysis*. ORNL/TM-2005/39, Oak Ridge National Laboratory, Oak Ridge, Tennessee.

Holman JP. 1996. *Heat Transfer*. McGraw-Hill Companies. Edition 8.

Incropera FP, DP Dewitt, TL Bergman, and AS Lavine. 2007. *Fundamentals of Heat and Mass Transfer*. 6th ed. John Wiley & Sons, Hoboken, New Jersey.

Lombardo NJ, JM Cuta, TE Michener, DR Rector, and CL Wheeler. 1986. *COBRASFS: A Thermal-Hydraulic Analysis Computer Code; Volume Ill: Validation Assessments*. PNL-6049, Vol. 3, Pacific Northwest Laboratory, Richland, Washington.

Michener TE, DR Rector, JM Cuta, RE Dodge, and CW Enderlin. 1995. *COBRA-SFS: A Thermal-Hydraulic Code for Spent Fuel Storage and Transportation Casks*. PNL-10782, Pacific Northwest National Laboratory, Richland, Washington.

Michener TE, DR Rector, JM Cuta, and HE Adkins, Jr. 2017. *COBRA-SFS: A Thermal-Hydraulic Code for Spent Fuel Storage and Transportation asks, Cycle 4a*. PNNL-24841, Pacific Northwest National Laboratory, Richland, Washington.

NAC 2011. FSAR – Non-Proprietary – MAGNASTOR "Final Safety Analysis Report." Rev. 1, NAC International, Norcrosse, Georgia.

NRC 2003. *Cladding Considerations for the Transportation and Storage of Spent Fuel*. SFST-ISG-11, Rev 3, U.S. Nuclear Regulatory Commission, Washington, D.C.

Rearden, B.T. and M.A. Jessee, Eds., *SCALE Code System*, ORNL/TM-2005/39, Version 6.2, Oak Ridge National Laboratory, Oak Ridge, Tennessee (2016). Available from Radiation Safety Information Computational Center as CCC-834.

Rector DR and TE Michener. 1989. *COBRA-SFS Modifications and Cask Model Optimization*. PNL-6706, Pacific Northwest Laboratory, Richland, Washington.

Siemens, PLM. 2019. STAR-CCM+ 14.02 (computer software). Siemens Product Lifecycle Management Software, Inc., Plano, Texas.

Wieselquist, W.A., A.B. Thompson, J.L. Peterson, and S.M. Bowman. 2016. *ORIGAMI Automator Primer: Automated ORIGEN Source Terms and Spent Fuel Storage Pool Analysis*. ORNL/TM-2015/409. Oak Ridge National Laboratory, Oak Ridge, Tennessee.